X-RAY TOPOGRAPHY TECHNIQUES FOR THE ANALYSIS OF LASER

IRRADIATED SILICON

A Thesis presented to the Faculty of the Graduate School

University of Missouri-Columbia

In Partial Fulfillment

of the Requirements for the Degree

Master of Science

---

by

PRAJVAL STEPHEN RODRIGUES

Dr. Robert A. Winholtz   Thesis Supervisor

DECEMBER 2005

The undersigned, appointed by the Dean of the Graduate School,

have examined the thesis entitled

X-RAY TOPOGRAPHY TECHNIQUES FOR THE ANALYSIS OF
LASER IRRADIATED SILICON

Presented by

Prajval Stephen Rodrigues

A candidate for the degree of

Master of Science

And hereby certify that in their opinion it is worthy of acceptance.

Dr. Robert A. Winholtz

Dr. Robert Tzou

Dr. Paul F. Miceli

ACKNOWLEDGEMENTS

LIST OF TABLES

LIST OF FIGURES

TABLE OF CONTENTS

CHAPTER 1

INTRODUCTION

1.1   X-rays

X-rays have a very short wavelength compared to other electromagnetic waves. The interaction of electromagnetic radiation with matter depends on the wavelength. The term X-rays refers to electromagnetic radiation wavelengths between about 0.01 and 100 Å. X-rays occupy the region between gamma and ultraviolet rays in the complete electromagnetic spectrum [Cullity, 1978]. X-rays below about 1 Å are termed "hard" and this includes gamma rays; above 10 Å, we speak of "soft" X-rays. The SI unit in the X-ray wavelength regime is the nanometer (1 nm = 10^{-9} m), but the Ångstrom (1 nm = 10 Å) is convenient and is frequently used. Since x-rays have a very short wavelength, they contain a lot more energy than radiation with longer wavelengths. An interesting characteristic of x-rays is their ability to pass through many materials. A common way to detect x-rays is with photographic film. Since x-rays are electromagnetic waves just like visible light rays, they also will cause photographic film to be exposed. Photographic films however, always need an intensifier screen and the film in such cases is poorly exposed by x-rays. X-rays can also be detected with detectors similar to those used in digital cameras to record visible light.

X-rays have a wavelength, which is about the same size as an atom. Since the wavelength of X-rays is comparable to the lattice-spacing of many materials, they undergo diffraction. This is useful in studying the nature of a crystal and the arrangements of atoms within a crystal.

1.2   X-ray Diffraction and Topography

When X-rays or neutrons are scattered by a crystal, the periodic array of scattering sites - electrons for X-rays and nuclei for neutrons - leads to directions around the scattering material in which the scattered waves scatter constructively or in-phase [Krawitz, 2001]. The addition of the amplitudes of all these waves in given directions results in almost zero intensity in most directions but strong beams in some directions [Bowen et al., 1998]. In these directions, peaks in intensity, which are the summations of amplitudes of the incident plane waves scattered by the electrons or nuclei, are observed. This is the phenomenon of diffraction. The positions, intensities and shapes of these peaks are related to the crystal structure (peak position and intensity) and physical state (peak shape) of the material, as well as to the experimental measurement parameters [Krawitz, 2001].

Comparing material evaluation techniques, radiography is a very important tool in itself and though it has a wide field of applicability, it is ordinarily limited in the internal detail it can resolve, or disclose, to sizes of the order 10^{-1} cm. Diffraction on the other hand, can indirectly reveal details of internal structure of the order 10^{-8} cm in size, and it is with this phenomenon, its has its applications in evaluating materials [Cullity, 1978].

1.2.1   Bragg's Law

The simplest and most useful description of diffraction is still that obtained by Bragg. As seen in Figure 1.1, it relates peak position (the diffraction angle θ), interplanar spacing d, and the wavelength of the radiation λ [Krawitz, 2001]. Strong diffraction occurs when all the waves add up in phase. It can be seen from Figure 1.1 that strong diffraction results when

$$n\lambda = 2d \sin \theta \qquad\qquad (1.1)$$

where n is a integer representing the order of diffraction.

A small number of planes give a very broad peak and large numbers of planes a narrow peak, converging to a value characteristic of a thick crystal. Thus, diffraction for a given plane and wavelength does not take place over the zero angular range defined by Bragg law, but over a small finite range. This range, called the rocking curve width, varies and it governs the strain sensitivity of the technique [Bowen et al., 1998].
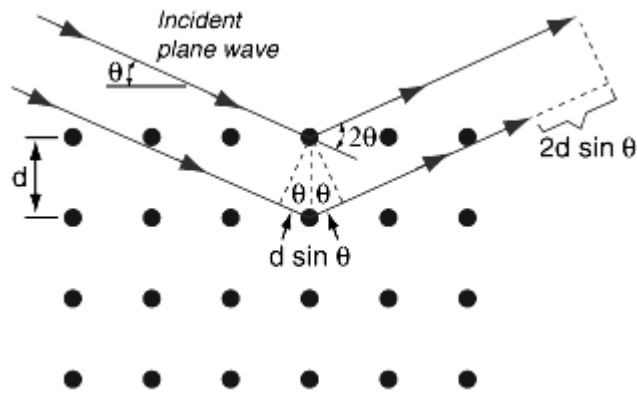
Figure 1.1. Illustration of Bragg's Law [Georgia State University].

X-ray topography creates an image of a crystal with a diffracted x-ray beam as illustrated in Figure 1.2. While most x-ray diffraction techniques mathematically reconstruct structural information about the specimen by making measurements in reciprocal space, x-ray topography creates a direct image of crystal defects such as strained regions. Imperfect regions of a nearly perfect crystal will diffract differently than the surrounding perfect regions, giving rise to contrast in the diffracted beam and producing an image of the imperfections [Winholtz, 2003].

3

X-ray topographic techniques produce an image of a surface of crystal, or of the projection of a selected volume of crystal, by recording the diffracted X-ray intensity issuing from such surface or volume. Two factors, often largely independent and separable, determine the level of intensity reaching each point on the image recording medium. The first is simply whether or not the specimen is locally oriented so that some radiation among the range of wavelengths impinging upon it can be reflected by Bragg's law, and secondly, whether the intensity of such reflected rays will range from zero upwards [Amelinckx et al., 1978].

For nearly perfect crystals, the angle θ where diffraction occurs is very sharply defined and the full-width at half-maximum over which diffraction occurs is measures in seconds of arc. Changes in this rocking curve width can be measured and used as a measure of crystal imperfection [Winholtz, 2003].
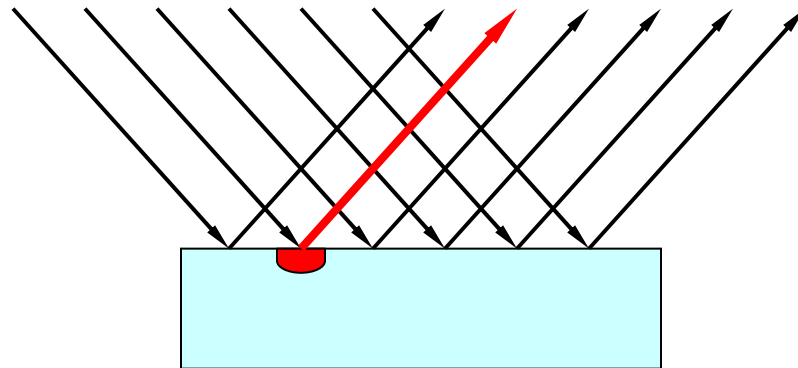
Figure 1.2. Illustration of image formation in x-ray topography. Rays of the incident x-ray beam produce a diffracted x-ray beam. Where the crystal is perfect, the diffracted rays are all of the same intensity. Where the crystal is damaged (dark region) the crystal diffracts with a different intensity or direction giving rise to contrast within the diffracted beam [Winholtz, 2003].

1.3   Literature Review

A complete theoretical understanding of laser interactions and damage of materials, particularly in the ultra-fast regime, has not yet been achieved. Laser ablation plays an important role in laser processing and structuring of materials. The applications range from high-precision drilling and cutting to fabrication of complex surface patterns or highly controlled changes of the physical or chemical microstructure. By choosing the proper laser parameters such as wavelength, intensity, and pulse duration, a great flexibility is available to tailor laser ablation to suit specific tasks.

During the last decade, investigations have focused on the study of the differences between the processes induced by ultra-fast (fs) laser pulses and those generated by longer laser pulses [Herrmann et al., 1998]. Also, during the last few years, results have been reported, which indicate that the use of very short laser pulses provide distinct advantages in certain applications over laser pulses of much longer duration[Liu et al., 1997] . These findings have stimulated the interest in the physical understanding and damage mechanisms caused by short pulse laser ablation [Linde et al., 2000]. Experimental and theoretical investigation of ultrashort pulse damage threshold of Si has been carried out by Allenspacher et al. in 2003, Chen et al. in 2004 and Azzouz in 2004. The results of theoretical and experimental findings have been consistent.

Careful experimental evaluations and studies are vital in gaining a detailed understanding of the interaction and damage mechanisms. There is currently much interest in femtosecond scale laser interactions with materials. Comparison of the damage produced by the ultra-fast femtosecond laser pulses to the longer nanosecond pulses is also of interest.

Optical microscopy and scanning electron microscopy give us a brief idea of the physical nature of the damage. They provide information about the location, surface profile and extent of visible damage. However these methods do not give us an idea of the damage to the crystal lattice caused by laser ablation.

This study examined the use of X-ray topography to investigate the effects and differences in laser irradiation damage to single crystal silicon. The theory and application of conventional and synchrotron radiation topography has been covered in text by Bowen and Tanner. The use of x-ray diffraction to detect strain fields in single crystal substrates began over four decades ago with transmission-based x-ray topography techniques by Lang, 1959. X-ray topography as a completely nondestructive technique is used to study crystal defects, deformation fields and compositional changes in semiconductors because of high sensitivity to strains induced by defects in crystals [Korytar & Ferrari, 2001; Bowen et al., 1998]. X-ray diffraction, for example has been used to detect deformation fields due to overlying strained thin film features and residual stress due to evaporated Ni dots on Si substrate [Murray et al., 2004]. The transient structural changes in materials under laser irradiation have been measured by time-resolved X-ray diffraction. Lattice deformation in laser irradiated silicon crystal has been studied by picosecond X-ray diffraction [Kishimura et al., 2003]. X-ray topography can hence be used as a useful tool to analyze lattice damage, stress and strain in crystals. The propagation and elimination of dislocations generated at the early stage of Czochralski silicon crystal growth has been studies using synchrotron white x-ray topography [Kawado et al., 2005]. X-ray rocking curve measurements are sensitive to strain [Bowen et al., 1998] and with topography have also been used to study the influence of nitrogen

impurities on the defect structure of synthetic diamonds [Hoszowska1 et al., 2001]. Time resolved x-ray diffraction experiments have also been performed to study macromolecular systems of biological importance [Stojanoff et al., 1997; Boggen et al., 200; Hu et al., 2001].

X-ray topography provides a unique method of examining the damage produced. Silicon wafer specimens were prepared with laser irradiated spots at different fluence levels with both nanosecond pulses and femtosecond pulses. The specimens were designed to be examined with X-ray topography. High resolution topographs of the laser-irradiated spots on both groups of crystals were produced. The resolutions of the topographs were smaller than the irradiated spots and hence reveal the differences in damage from the nano- and femtosecond lasers.

1.4   Synchrotron Radiation

Synchrotron radiation is the electromagnetic radiation emitted by charged particles that are moving (in circular orbits) at extremely high speeds (close to the speed of light) in a magnetic field. The following section will discuss in detail the generation and applicability of synchrotron radiation in high resolution x-ray diffraction and topography.

1.4.1   Synchrotron Radiation Sources

In a conventional tube, X-rays are generated when energetic electrons are stopped by a metal target. The process is inefficient and the thermal properties of solids place an upper limit on the brightness of X-ray beams that can be achieved [Bowen et al., 1998]. Conventional X-ray sources emit unpolarized divergent, quasi-monochromatic radiation. The conversion of electron power to characteristic X-radiation is less than 0.1% efficient. In contrast, electrons accelerated in a storage ring or in a synchrotron emit linearly polarized white radiation as a near plane wave with almost 100% efficiency [Hart, 1975]. As there are no target materials to melt, the brightness achievable from synchrotron radiation sources may be 10^3 to 10^8 times higher than those obtained from standard X-ray generators [Bowen et al., 1998].

When electrons are confined to a circular orbit in a storage ring by a magnetic field, electromagnetic radiation called synchrotron radiation is emitted, owing to their high acceleration towards the center of the circle [Bowen et al., 1998]. Such radiation was originally a by-product of high-energy research facilities used to study atomic particle collision. These *first generation* sources have been supplanted by *second-* and *third-generation* sources that are dedicated to research in materials, life sciences and

other activities. Our main interest derives from the high intensities produced, the ability to choose from a continuous range of wavelengths and the natural collimation of synchrotron beams. The Advanced Photon Source (APS), a third-generation synchrotron source at Argonne National Laboratory near Chicago, serves as a model facility. A schematic of the APS facility is shown in Fig 1.3 [Krawitz, 2001].

Synchrotron radiation is produced by the acceleration of electrons or positrons. Electrons (at the APS) are accelerated to near the speed of light (energies of up to 7 GeV at the APS). At the APS this is accomplished initially in a linear accelerator (linac), then a 368 m racetrack-shaped booster ring in which radio frequency cavities impart 32 keV per turn to the initial 450 MeV electrons. In 0.25 s they make 200,000 orbits and reach their target energy of 7 GeV. They are then injected into a storage ring (1104 m in circumference) where they are steered by 1097 magnets and make 271,000 orbits per second in a 1×10^{-9} torr vacuum (atmospheric pressure is 760 torr). The electrons are guided by magnets that bend them and also *wiggle* or *undulate* them, that is, create oscillations in the magnetic field to impart greater beam flux.

At relativistic velocities, the emission is strongly peaked in the forward direction, tangential to the electron orbit. Perpendicular to the orbit plane, the emission angle θ is given by $\theta = m_o c^2 / E$, where m_o is the electron rest mass, c is the velocity of light and E is the electron energy [Bowen et al., 1998]. Thus a 7 GeV beam has an opening angle of 0.0004^o (15 s) of arc. The flux of a beam is given by (photons/s-mrad-unit bandwidth), whereas brightness is (photons/s-unit solid angle-unit source area-unit bandwidth) [Krawitz, 2001].
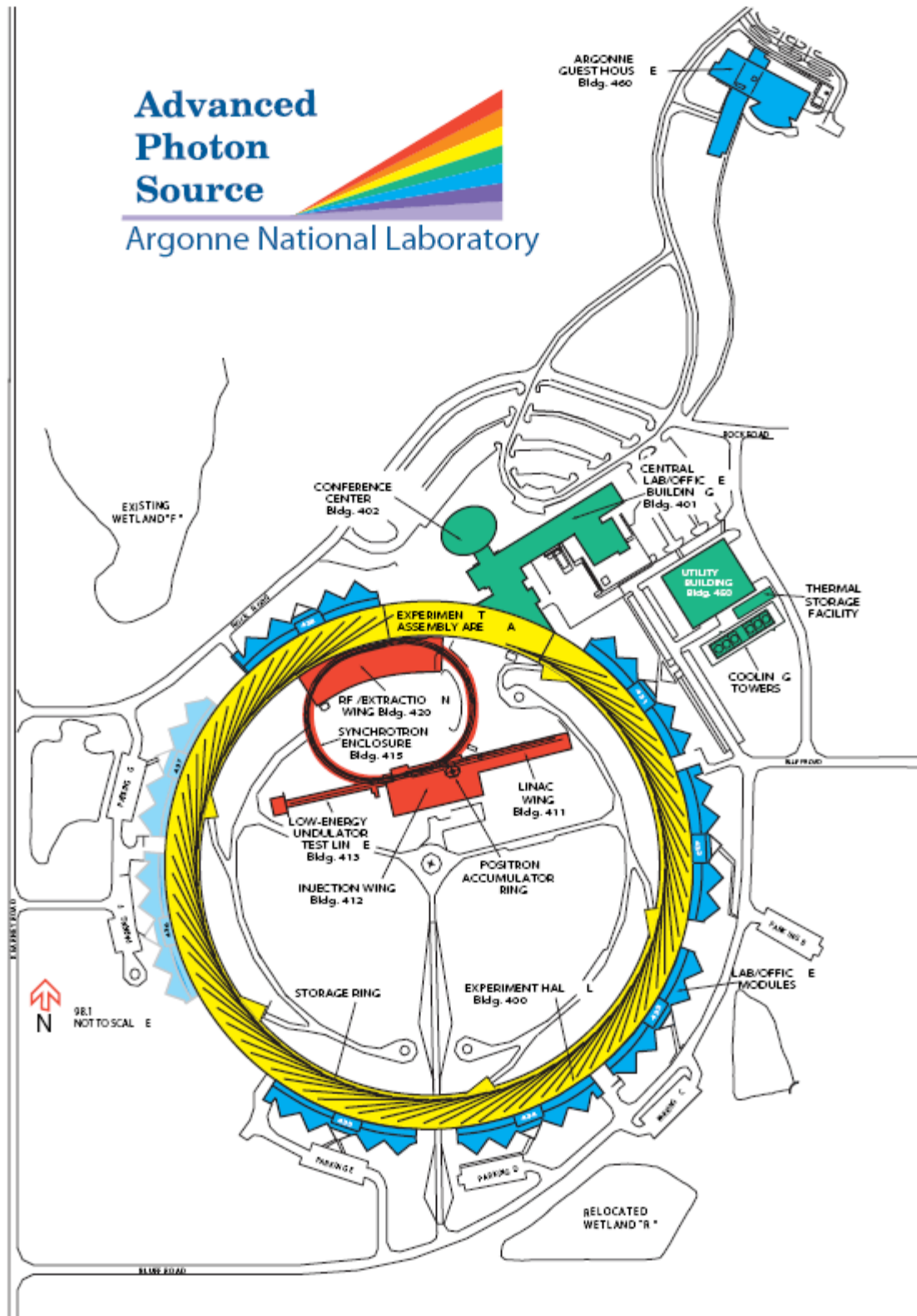
Figure 1.3. Schematic of the Advanced Photon Source at Argonne National Laboratory [APS].

1.4.2 Applicability of Synchrotron Radiation to X-ray Topography

There are five features of synchrotron radiation which make it both unique and worth the effort of traveling to a distant place to conduct experiments [Bowen et al., 1998]. They are Intensity, Continuous spectrum, Collimation, Polarization and Time structure.

1.4.2.1 Intensity

In order to take high resolution X-Ray topographs, slow, very small grain size photographic emulsions were conventionally used. Ilford L4 nuclear emulsions used to give the best results, and exposure times on conventional generators range from hours to days. Use of synchrotron radiation reduces exposure times on these emulsions to a matter of seconds or less. Direct imaging electronic area detectors, which are severely limited in resolution from quantum noise with conventional generators, have enough photons with synchrotron radiation to give good quality images in real time. Dynamic experiments, in which changes in the material are studied as a function of variables, such as time, temperature, stress or electric or magnetic field, may thus be performed either in real-time at moderate resolution or in a rapid step-by-step mode at high resolution.

1.4.2.2 Continuous Spectrum

A storage ring designed for synchrotron radiation emits radiation over a very broad spectrum which extends down to 0.1 Å at the third-generation sources. The long wavelength cutoff is usually set at about 2.5 Å from the absorption of the beryllium window. This wide wavelength range allows one to optimize independently geometry, absorptions conditions and strain sensitivity by selecting a wavelength to use. The

continuous spectrum permits high resolution Laue topographs to be taken which are extremely easy to set up and are applicable to a wide range of materials.

1.4.2.3 Collimation

Because of low divergence, topography experiments may be conducted at a great distance (50-1000 m) from the source. This provides a wide beam at the specimen and relatively large areas may be illuminated without the need for scanning.

1.4.2.4 Polarization

The high degree of X-ray polarization in the electron orbit plane provides means of controlling both the signal/noise ratio and the penetration of the X-rays into the specimen. Depending on whether the incidence plane is chosen vertically or horizontally, σ (sigma) or π (pi) polarization may be selected.

1.4.2.5 Time structure

The pulsed time structure, typically at megahertz rates, permits stroboscopic topography of very rapid cycle phenomena such as the propagation of acoustic waves. The pulse rate at the APS is 2 Hz.

1.5 Lasers

The term LASER is an acronym for Light Amplification by Stimulated Emission of Radiation. A laser is a device that's amplifies light and produces a highly directional, high-intensity coherent beam that most often has a very pure frequency or wavelength. It comes in sizes ranging from approximately one tenth the diameter of a human hair to the size of a very large building, in powers ranging from 10^{-9} to 10^{20} W, and in wavelengths ranging from the microwave to the soft X-ray spectral regions with corresponding frequencies from 10^{11} to 10^{17} Hz. Lasers have pulse energies as high as 10^4 J and pulse durations as short as 5×10^{-15} s. They can drill holes in the most durable of materials and can weld detached retinas within the human eye. They are used to perform heat treatment of high-strength materials and provide a special surgical knife for many types of medical procedures. They act as target designators for military weapons and are a key component of some of our most modern communication systems [Silfvast, 2004]. Some of the most important laser properties are discussed below [Hect, 1994].

1.5.1 Wavelength

Light is made of waves, and the wavelength, is a fundamental characteristic of light. Each type of laser emits a characteristic wavelength or a small range of wavelengths. The wavelengths depend on the type of material that emits the laser light, the laser's optical system, and the way the laser is energized. Laser action can produce infrared, visible and ultraviolet light. Most lasers are called monochromatic and nominally emit one wavelength. Actually, they emit a range of wavelengths, but the range is narrow enough to be considered a single wavelength for most purposes. Some lasers emit light at different wavelengths under different conditions.

1.5.2 Output Power

Output power measures the strength of a laser beam, which differs widely among lasers. Strictly speaking power measures how much energy the laser releases per unit time; it is measured in watts and defined by the formula

$$\text{Power} = \Delta \text{ (Energy)}/ \Delta \text{ (Time)} \tag{1.2}$$

One watt is defined as a rate of one joule (of energy) per second. Laser output powers cover a wide range. Some lasers produce beams containing less than a thousandth of a watt (a milli-watt) and some produce thousands of watts (kilo-watts).

1.5.3 Duration of emission (Pulsed and Continuous Output)

Lasers often emit steady beams of light or pulses of light. Laser pulses can come in various durations and repetition rates. The length or duration of a pulse can range from milliseconds to femtoseconds or, in scientific notation 10^{-3} to 10^{-15} second. The pulses may be repeated once a minute, or may appear thousandth or even millionth of times in a second. If you want to get the total energy in a pulse, you need to know how the power changes with time. A laser may have extremely high peak power during a short pulse, but because a pulse is short, it doesn't contain much energy. To make a simple approximation

$$\text{Pulse Energy} = \text{Peak Power x Pulse Length} \tag{1.3}$$

The average power in a pulsed laser beam differs from the peak power; it is a measure of the average energy flow per second. Thus,

$$\text{Average Power} = \text{(Number of Pulses x Pulse Energy)}/ \text{Time} \tag{1.4}$$

Peak and average power can both be important quantities depending on laser application. Both are measured in watts and as would be expected, peak power is higher. Pulse energy is measured in joules.

1.5.4 Beam Divergence and Size

Laser beams, on careful observation spread out as you get farther from the laser. This spreading is called divergence; it is measured as half the full angle at which the beam spreads. Laser beam divergence is typically measured in milliradians, or thousandths of a radian. Laser beams have small divergence and some can be detected at long distances. This high directionality of laser beams is one of their most important properties.

1.5.5 Coherence

Light waves are coherent if they are all in phase with one another. The more monochromatic a laser is, the more coherent it is. Monochromatic light need not be coherent, but light that is not monochromatic cannot stay coherent over a long distance. Many laser applications do not require coherent light; the coherence is incidental.

1.5.6 Efficiency and Power Requirements

Lasers differ widely in how efficiently they convert input energy into light. Like other light sources, they are not very efficient in generating light, with the best converting up to about 30% of input energy into light. Many types convert as little as 0.01% or even 0.001% of the input energy into light.

Efficiency becomes a more important consideration at higher output powers. It's not a big problem if a 1-mW laser produces a watt of waste heat, because it's easy to dissipate that little heat. However, it would be very hard to dissipate the millions of watts of waste heat from a 1-kW laser with the same efficiency.

CHAPTER 2

EXPERIMENTAL

2.1   Specimen Preparation

Silicon wafers were used to produce the laser-irradiated specimens.   The Si wafers were donated by MEMC Electronic Materials, Inc. of St. Charles, Missouri.   All specimens were 100 mm diameter wafers with a nominal thickness of 0.6 mm.   Wafers were 100 wafers with a $\langle 100 \rangle$ direction normal to the wafer. The wafers had flats ground on the edges at the 6:00 o'clock and 9:00 o'clock positions which are perpendicular to $\langle 110 \rangle$ directions. The wafers were boron doped with a 23 μm layer of epitaxially grown silicon. The wafer resistivity was 0.01 (min), 0.02 (max) ohm-cm, and the epitaxially layer resistivity was 14 ohm-cm.

The specimens were laser irradiated at the Air Force Research Laboratory, Albuquerque, New Mexico. Specimens were produced using two different lasers systems, a nanosecond laser and a femtosecond laser.   The nanosecond laser was a flash lamp pumped Nd:YAG laser that produced 1064 nm light.   A KD^*P second harmonic crystal generated a 532 nm wavelength beam that was separated from the 1064 nm light with a prism.   The full-width half-maximum (FWHM) length of the laser pulses was 8 ns and the laser produced pulses at 10 Hz.   The laser beam was focused near the specimen surface using a 100 mm focal length lens.   The specimen was positioned slightly in front of the focal spot at the desired beam diameter.   The $1/e^2$ beam diameter was determined by scanning a razor blade across the beam in front of an energy detector and fitting the

profile to an error function. At the specimen surface the beam was measured 6 times giving an average beam size of 48.5 μm.

The femtosecond laser was a mode locked fiber oscillator laser followed by a Ti:Saphire regenerative oscillator. It produced light of 775 nm wavelength in 150 fs pulses (FWHM) at a rate of 1000 Hz. The laser beam was focused near the specimen surface using a 50 mm focal length lens.

For the femtosecond laser system the beam size was determined by choosing a plane along the optic axis near the focal spot of the beam. A graticule was placed in this plane and the image expanded 10X onto a digital camera system with a two-lens telescope. The image of the beam in the camera was then used to compute the beam size along the horizontal and vertical directions. The $1/e^2$ beam size was roughly elliptically shaped with a 110 μm size in the horizontal direction and an 84 μm size in the vertical direction.

The number of pulses striking the specimen on the nanosecond laser was controlled with a mechanical shutter. With the femtosecond laser, the number of pulses striking the specimen was controlled with a Pockel cell for 1 and 2 pulses per spot, while for 10, 100 and 1000 pulses, a mechanical shutter was used. In both systems, the energy incident on the specimen was adjusted with a wave plate/ polarizing crystal system.

For the nanosecond laser system, the energy incident on the specimen for a laser shot was determined by measuring the energy in a beam produced with a beam splitter upstream of the specimen. An energy meter behind the specimen position was used to record the light energy in the beam striking the specimen with the specimen position empty in a prior calibration procedure. The system was calibrated over the energy range

17

used measuring the energy in both beams off the beam splitter and establishing the ratio over the range of wave plate settings (energy levels) used. A wave plate or a phase retardation plate is a birefringent optical material which introduces a phase difference between perpendicular axes of light. The incoming beam is separated into mutually orthogonal polarized beams that are recombined with a phase difference that is a function of the thickness of the material and the wavelength of the light. The energy incident on the specimen was then determined by measuring the energy off the beam splitter and using the determined ratio value to compute the energy on the specimen. The peak fluence on the specimen was then computed by assuming a radially-Gaussian energy distribution in the beam which gives

$$\phi_{peak} = 2E / A \qquad\qquad (2.1)$$

where ϕ_{peak} is the peak fluence, E is the total energy in the beam cross-section, and A is the $1/e^2$ area illuminated. The factor of two results from the non-uniform distribution of energy in the beam cross-section.
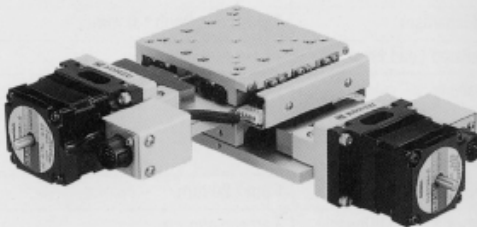
For the femtosecond laser, the peak fluence was determined by using a flip up mirror just in front of the specimen that directed the laser beam into an energy meter. With the mirror flipped up, the energy in the laser beam was measured several times; taking an average, and then the mirror was flipped down to irradiate the specimen [Winholtz, 2003].

2.2 X-ray Diffraction and Topography measurement

The X-ray diffraction and topography measurements of the laser irradiated specimens were carried out at the 2BM beamline of XOR (X-Ray Operations & Research) Sector 2, at Argonne National Laboratory's Advanced Photon Source. A Kohzu double-bounce Si (111) monochromator was used to deliver an approximately monochromatic beam with an angular divergence of 2×10^{-3} rad at beam energy of 12 keV, corresponding to a wavelength of 1.033 Å. A pair of horizontal and vertical slits defined the beam size of the white synchrotron X-radiation.

A four-circle Huber diffractometer was used along with a scintillation crystal and charge-coupled device (CCD) to perform rocking-curve and imaging measurements. Figure 2.1 shows the specifications of the specimen xyz stage attached to the four-circle Huber diffractometer. A screw pattern is used for the mounting of the specimen to the xyz stage.

Table Size	70 mm × 70 mm		
Guidance Mechanism	Precision Crossed Roller		
Motion Range	± 10 mm (2 axes)		
Lead Mechanism	Ground Screw, Pitch 0.5 mm		
Accumulated Lead Error	10 μm / 20 mm		
Repeatability	± 0.5 μm		
Backlash	1 μm		
Lost Motion	1 μm		
Straightness	1 μm / 20 mm		
Momentum Load Stiffness	2 arcsec / kg-cm		
Maximum Speed	2.5 mm / sec		
Load Capacity (Horizontally)	9 kg		
Material	Steel	Actuator	5-phase stepping motor (1000 p / rev)
Finish	Chromium Mat Plating	Resolution	0.25 μm / step (Half Step Mode)
Weight	2.4 kg	Connection	Type "A1" (see p. 272)
Perpendicularity	90° ± 20 arcsec	Cables	Type "CB" (see p. 275)

Figure 2.1. Specimen xyz stage specifications, attached to the 4-circle Huber Diffractometer. The screw pattern is used for mounting the specimen holder to the xyz stage [2BM].

Figure 2.2 shows the geometric height constraint for the specimen holder. The height constraint needs to be followed to center the specimen surface to the center of the diffractometer. This is required since the x-ray beam is setup to pass through this center of the diffractometer. The specimen mounting was done using a kinematic mount for the reproducible positioning of the specimen on the mount. The female kinematic mount is screwed on to the xyz stage and the male kinematic mount along with the specimen is seated on top of the female kinematic mount magnetically. Four hexagonal screws fasten the male-female assembly together, as seen in Figure 2.3.
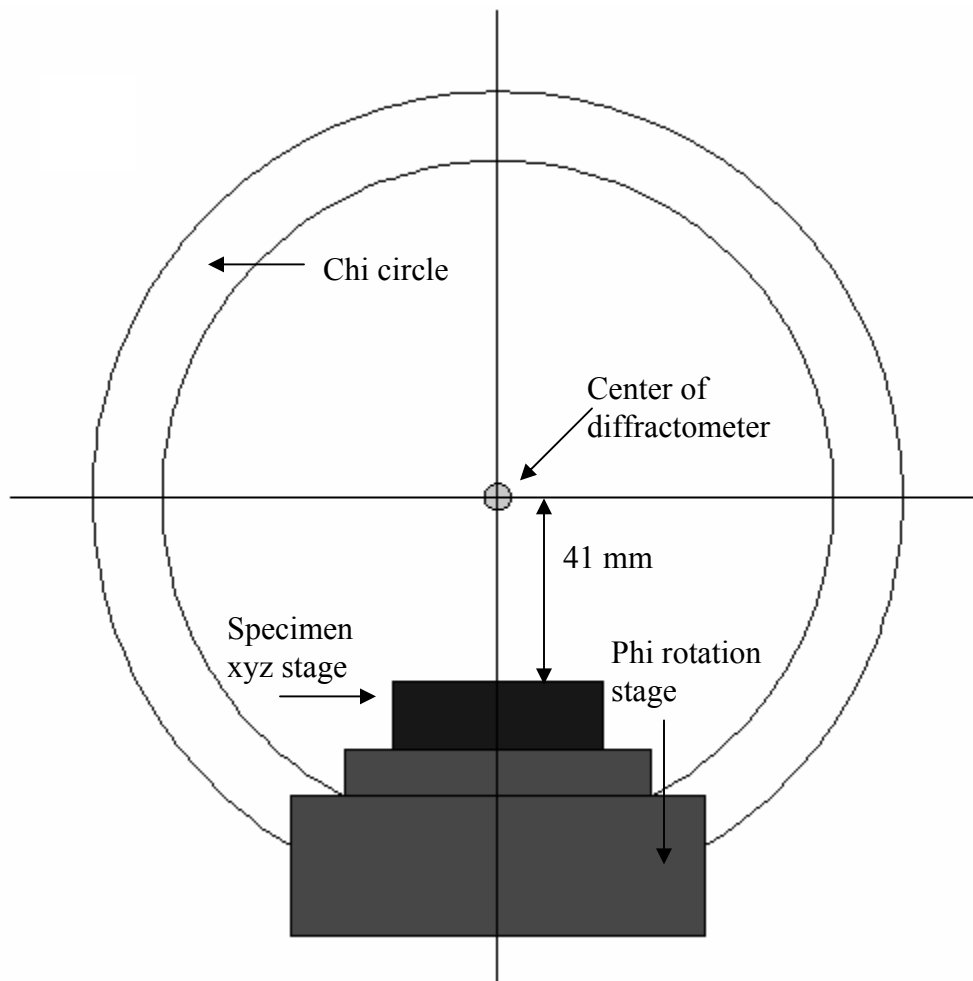
Figure 2.2. Geometric height constraint for the specimen holder required to center the specimen in the diffractometer [adapted from 2BM].
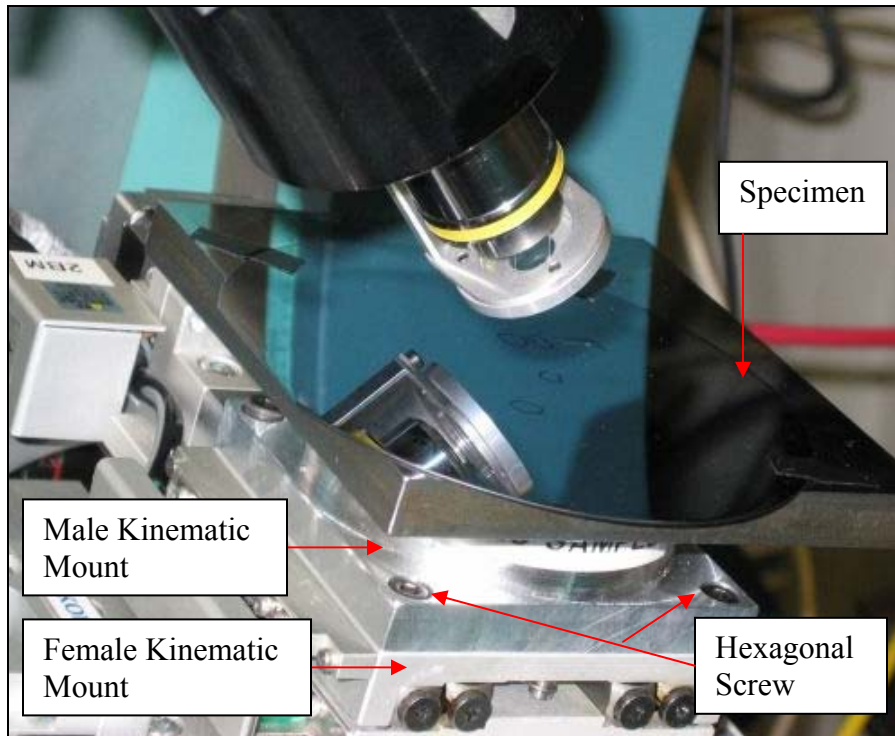
Figure 2.3. Specimen on diffractometer showing kinematic mount to translation stage.

The laser irradiated spots were aligned to the center of the diffractometer with the help of a microscope. The male kinematic assembly had a flat square stage, with a polished finish, to mount the specimen. The center point of this square stage (intersection of the diagonals) was marked with a pen to identify it, as it would be the center of the diffractometer when the translation stages were at the centers of their travels. This was done to facilitate easy mounting of the laser irradiated spots to the center of the diffractometer.

The specimens were then mounted on this marked stage, such that the laser irradiated spot of interest was directly over this center point. This was done under a microscope so that the laser irradiated spot could be placed over the center point of the stage with better accuracy. The specimens were then secured onto the stage, at the corners, with small pieces of electrical insulation tape. Tape was used due to its easy

removal. Care was taken not to strain the specimens while securing them and removing it from the specimen stage. The specimens lay nearly flat during the experiments so the tape did not need to support their weight. If the specimens were flexed during mounting, strains showed up in the topographs interfering the effects from the laser irradiation.

The male kinematic mount along with the specimen was then mounted on the female kinematic mount. The xyz stage was then adjusted such that the laser spot of interest was now at the center of the diffractometer. This was done with the aid of a focusing telescope and a camera positioned in a transit aligned to look along the center of the diffractometer. Figure 2.5 shows a schematic of the experimental setup.
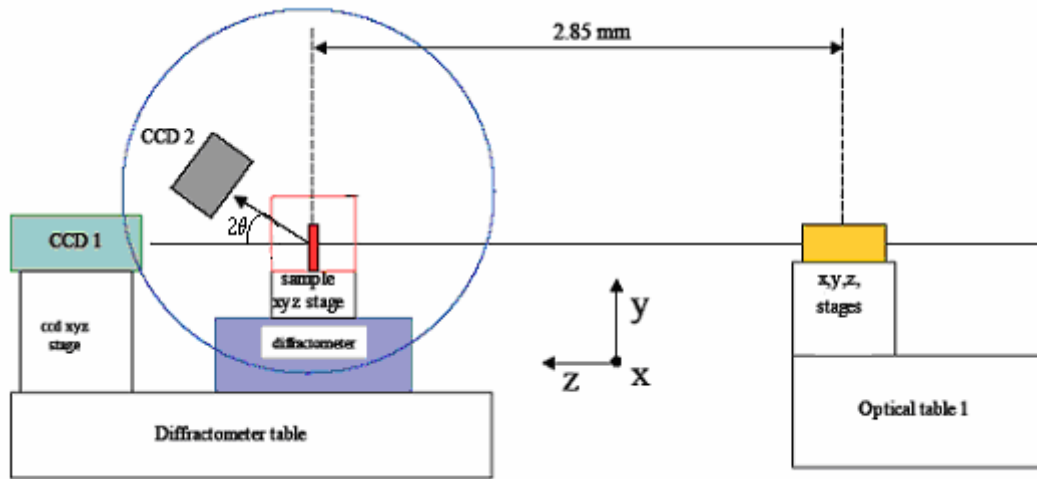
Figure 2.4. Schematic of experimental setup. Specimen xyz stage, four circle diffractometer controlling the angular orientation (theta, phi, chi, three orthogonal rotations for the specimen and 2θ, for the detector CCD2). CCD2 is the detector CCD with 1280 x 1024 pixels [adapted from 2BM].

The specimens had in them nanosecond or femtosecond laser irradiated spots in a 25 mm x 25 mm grid covering coordinates (0,0) to (25,25). Inside the grid there was an irradiated spot every 5 mm apart. Five marker pulses starting from (0,0) and every 0.25 mm apart followed by four marker pulses every 1mm apart in the x-axis, help identify the

22

origin of the coordinate system of the grid [Winholtz, 2003]. The xyz stage servomotor had a travel range of 20 mm in the X and Y directions. This facilitated easy centering of the other laser spots of interest to the center of the diffractometer. Laser spots that could not be centered outside the 20 mm x 20 mm translator range had to be remounted in the same way as described above.

Diffracted x-rays were observed with an x-ray camera constructed by 2BM XOR personnel. The camera consists of a thin scintillating crystal, a magnifying lens and a CCD camera. The scintillating crystal absorbs x-rays and produces visible light. The crystal must be thin so that the lens may focus this light onto the CCD camera with good spatial resolution. The lens produces a visible light image on the CCD of the x-ray intensity incident on the scintillating crystal. The CCD can then be read electronically and gives a digital image of the x-rays incident on the x-ray camera. The CCD camera along with the rest of the optic system provided two dimensional spatial sensitivity, allowing images to be formed of the diffracted beam. The CCD used to record data consists of a 1280 x 1024 pixel CCD chip and has an active area of 0.858 x 0.686 mm^2. The camera had interchangeable lenses and the pixel size was given by

$$Pixel\ Size = 6.7\ /\ Magnification \tag{2.2}$$

Thus the camera with a 10 X objective lens produced images with a 0.67 μm per pixel resolution and with a 20 X objective lens produced images with a 0.335 μm per pixel resolution.

A combination of the microscope objective and scintillation crystal into one piece was done for better efficiency and convenience of x-ray micro-imaging experiments, as shown in Figure 2.5. With this setup, mounts with different crystals/ objectives can easily

be interchanged. The above assembly mounts on the 2θ detector arm of the diffractometer.
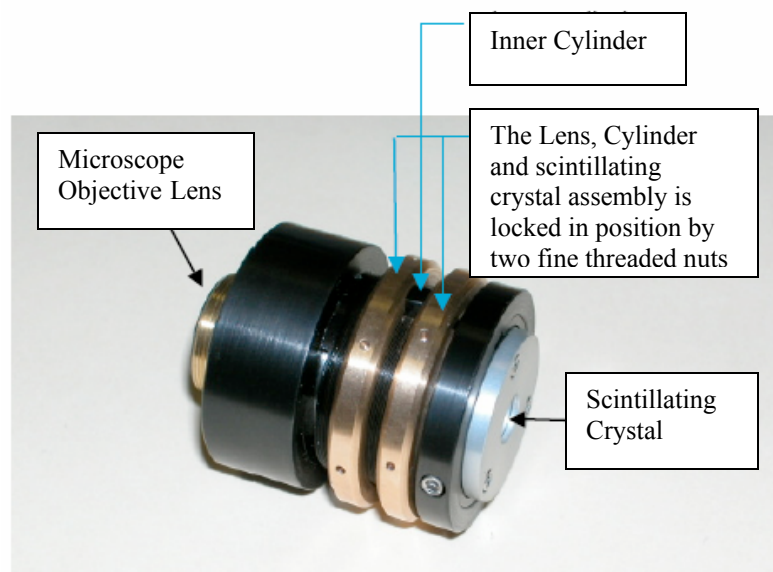
Figure 2.5. Photograph showing microscope objective and scintillation crystal assembly [2BM].

A picture of the entire assembly (4-circle Huber diffractometer, motorized CCD assembly, xyz specimen stage and kinematic mount assembly, along with laser irradiated specimen) is shown in Figure 2.6.

The experiments were performed on a bending magnet beam line, in an experimental hutch to keep the users isolated from high intensity x-rays. The overhead lights in the hutch were turned off during data collection as it would produce signals in the x-ray camera, interfering with data collection.
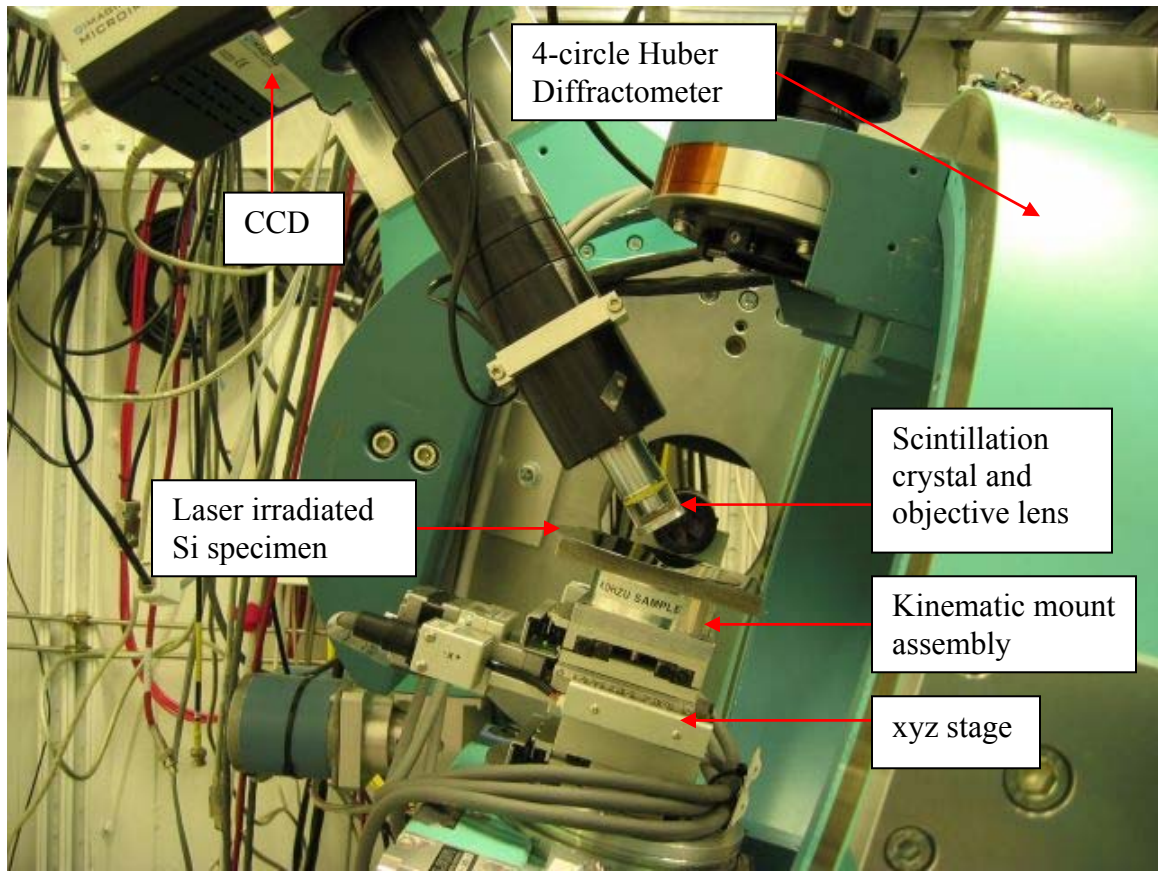
Figure 2.6. Photograph of the hutch showing 4 circle Huber Diffractometer, scintillating crystal and objective lens, kinematic mount with specimen and the xyz stage.

The specimen rocking was not made continuously but stepwise. The step size was determined by defining the length of the scan or range of the rocking curve, and exposure time for each specimen angular position was changed according to requirements of image clarity and brightness. Typical values of specimen rocking step were 0.9 arc (degrees) seconds at 7 GeV and 91.6 mA ring operation. The total exposure time for each photograph typically ranged from 6 s to 30 s for different laser spots. For all the experiments the data was taken using SPEC (X-Ray Diffraction and Data Acquisition software). SPEC is a UNIX-based software package for instrument control and data acquisition widely used for X-ray diffraction at synchrotrons around the world and in

25

university, national and industrial laboratories [Certif]. For each rocking angle of the rocking curve (scan), the images were stored as 16 bit TIFF (Tagged Image File Format) files.

Two work stations controlled most of the experimental setup process at the beamline. A UNIX based workstation controlled the beamline parameters and the data acquisition software. The setup parameters and data from the experiments were recorded by SPEC on this system. Another windows based workstation controlled the x-ray camera and diffractometer setup parameters. This included controls for the slits, diffractometer (chi, phi, theta and two-theta) and specimen xyz stage. Both the systems were networked and communicated with each other.

Table 2.1 summarizes the laser spots, on which the experiments were done, and lists the diffraction peaks and Bragg angles for each experiment.

Table 2.1. Diffraction peaks and Bragg angles used in the experiments.

	Femtosecond Laser Spots			Nanosecond Laser Spots		
	h k l	θ (°)	2θ (°)	h k l	θ (°)	2θ (°)
High Peak Fluence	0 0 4 Trial 1	22.442	44.127	1 1 5 Trial 1	13.742	58.350
				$1\bar{1}5$ Trial 2	13.833	58.350
	$\bar{1}\bar{1}5$ Trial 2	13.923	58.350	$\bar{1}\bar{1}5$ Trial 3	13.849	58.350
				$\bar{1}15$ Trial 4	13.814	58.350
Low Peak Fluence	0 0 4 Trial 1	22.479	44.127	1 1 5	13.928	58.350
	0 0 4 Trial 2	22.445	44.387			

As the specimen is rocked through angle θ, the x-ray camera is located at an angle 2θ and sees true horizontal dimensions. But due to the oblique angle from which it sees

the specimen the vertical dimension is shortened and is not the true vertical dimension on the specimen. The vertical dimension is corrected by the angle from the surface of the specimen. This correction is done by dividing the vertical dimension by Sin $(2\theta - \theta)$, $(2\theta - \theta)$ being the inclination angle. Hence, the topographs displayed have pixels that are not square but rectangular. The pixels were stretched in the vertical direction to compensate for the foreshortening and give a true perspective on features observed in the topographs.

Figure 2.7 shows a stereographic projection for the specimens with the reflections used. The x-ray beam follows the path FOE and hence the plane FOE forms the diffraction plane. The rotation axis for the rocking curves is always perpendicular to the diffraction plane. The $0\,0\,4$ is normal to the surface and four of the 115 type reflections are 15.973° away as indicated at the azimuths 90° apart. Experiments were started by finding the $0\,0\,4$ reflection. To take topographs with one of the 115 type reflections, the x-ray camera was set to the correct 2θ angle and the pole was brought into the diffraction condition. The pole was brought into the diffraction condition by rotating about the specimen normal to the azimuth, bringing the pole into the diffraction plane (using the φ axis). The pole was then tilted in the diffraction plane to bring it into the diffraction condition by rotating about an axis perpendicular to the diffraction plane (the θ axis). This resulted in asymmetric diffraction from the 115 type reflections.
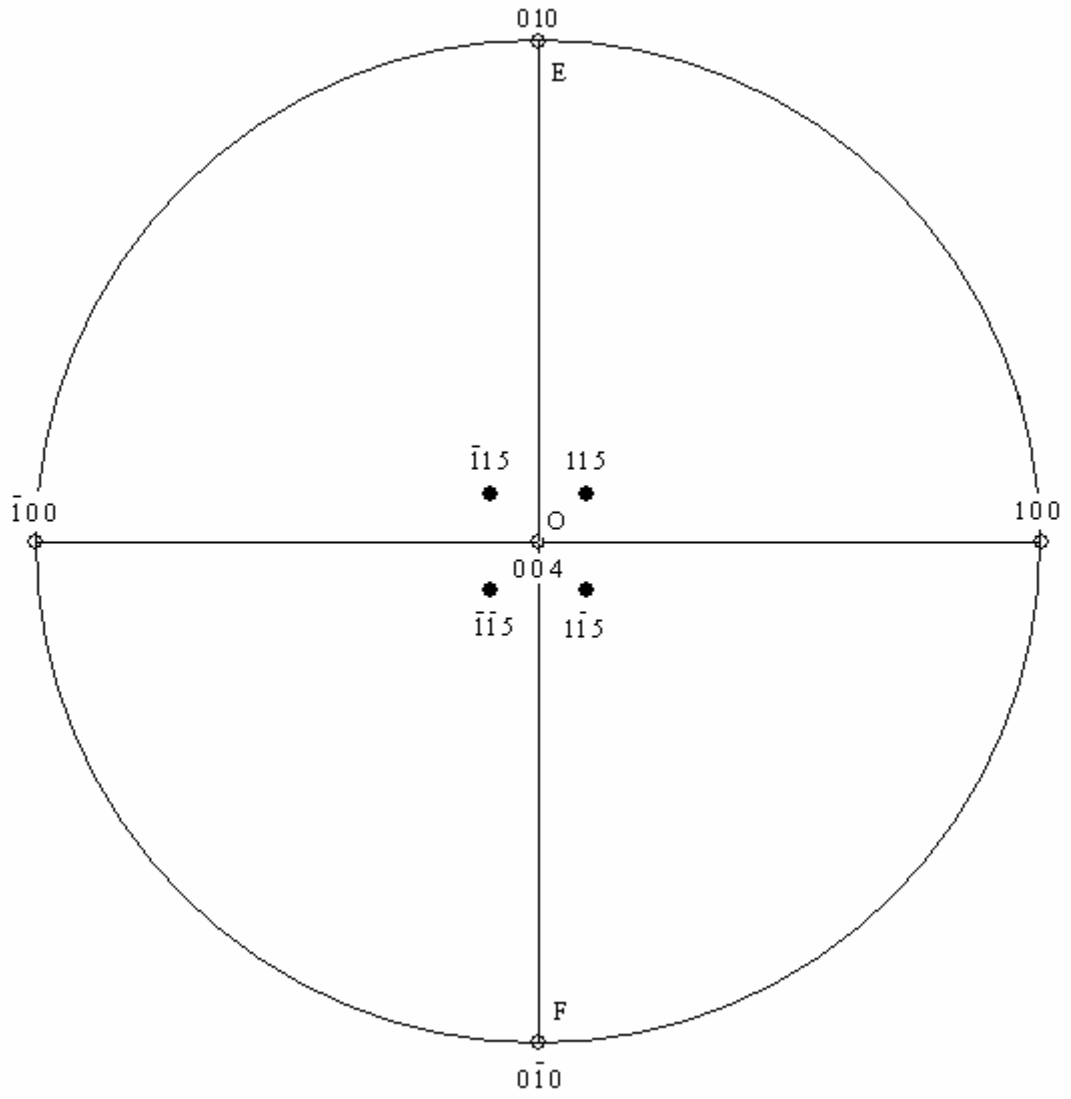
Figure 2.7. Silicon stereographic projections showing the 001 and 115 families of planes.

CHAPTER 3

RESULTS AND DISCUSSION

In the experimental section data was recorded as image scans (specimen rocking curves) for multiple High Peak Fluence and Low Peak Fluence nanosecond (ns) and femtosecond (fs) laser damaged spots. Some of the scans had to be aborted and some were voided during experimentation due to technical errors like the shutdown of the beam and miscalculations of crystal orientation and setup. All the scans were summarized with details about the type of laser, laser beam fluence, specimen coordinate of laser spot, diffraction peak used (h k l), rocking curve angles, exposure time for images, number of images in each scan, successful completion of the scan etc. Keeping all the above summarized details in mind, the image scans were scrutinized and a pattern was laid out to analyze certain scans that would be significant in nature. Table 3.1 shows a summary of the analyzed topographs of the laser spots. This section deals with the details of some of the recorded micrographs and topographs of the laser spots.

Table 3.1. Summary of the laser spots with peak fluence, picked for detailed analysis.

	Femtosecond Laser Spots		Nanosecond Laser Spots	
	h k l	Peak Fluence (J/cm^2)	h k l	Peak Fluence (J/cm^2)
High Peak Fluence	0 0 4 Trial 1	4.83	1 1 5 Trial 1	4.71
			1 $\bar{1}$ 5 Trial 2	
	$\bar{1}$ $\bar{1}$ 5 Trial 2	4.83	$\bar{1}$ $\bar{1}$ 5 Trial 3	
			$\bar{1}$ 1 5 Trial 4	
Low Peak Fluence	0 0 4 Trial 1	0.63	1 1 5	0.40
	0 0 4 Trial 2	0.63		

3.1 Igor Pro

All the image analysis in these experiments was done using the software IGOR Pro 5.0.2, by WaveMetrics, Inc [Wavemetrics]. IGOR Pro is an interactive software environment for experimentation with scientific and engineering data and for the production of publication-quality graphs and page layouts. IGOR Pro handles large data sets very quickly and includes a powerful suite of image processing operations for image filtering, manipulation, engineering analysis, graphing and quantification.

All the 16-bit TIFF files that were acquired as raw images in each scan were first assembled into a three dimensional data structure or stack. The axes or indices of the 3D data structure represent the X and Y axis of each image along with the rocking curve angle as the Z or θ axis (i.e., each constant Z slice represented a single rocking curve angle image).

3.2 Image Shift

The raw data stacks had to be corrected for an image shift, since the camera was stationary at all times as the specimen was rotated through its rocking curve. This caused a vertical shift in the images as shown and explained in Figure 3.1.

Figure 3.1. Image shifting process in a scan

Let point A be the center of rotation of the θ axis. The specimen rotates about this axis in a θ scan. A stationary x-ray camera, HG, is located a distance R from the center of rotation. Point C is an identifiable point on the surface of the specimen. In a topograph, point C is imaged on the x-ray camera at point D. Point B is the point on the specimen surface directly above (below) the center of rotation along the normal to the surface. The distance AB is the deviation of the sample surface from the center of the diffractometer and will be small for a well aligned specimen. Through a θ scan, the specimen rotates.

As the specimen rotates from θ to $\theta+\delta\theta$, the point B moves to point E and point C moves to point F. On the x-ray camera, the image point D moves to point G. The shift of a feature at point D on the topograph due to a rotation of $\delta\theta$ is h_c. h_c can be computed as $R\delta2\theta$ with only a small error, as shown in Appendix 1, for each rocking curve angle. Hence each image at increasing θ was shifted down vertically by $R\delta2\theta$, apportioning intensity to the new pixel proportional to the area overlap. For example, for an $R\delta2\theta$ shift of 4.7 pixels, 70 % of the intensity in each pixel would be shifted 5 pixels down and 30 % shifted 4 pixels down. Figure 3.2 shows an image produced from the sum of all the images in a rocking curve scan before and after the image shift correction. It can be seen clearly that the images seemed to be smeared vertically as an effect of the image shift and the corrected images show how the smearing effect is minimized. It is seen that with the high spatial resolution in the topographs, this correction is needed.

In addition to the image shift described above, another error exists in the system due to the change in the beam footprint on the specimen along with the change in rocking curve angle. As seen in Appendix A, the magnitude of this error is very small, on the order of approximately 0.049 μm (~0.075 pixel vertically) over a rocking curve range of 0.06˚ θ and has not been corrected for.

The data structures were then cropped to focus mainly on the laser irradiated spots. Cropping was done in a way such that only the portion outside the strain field of the feature was removed. The 3 dimensional data structures were then filtered using a 3 dimensional, 3 x 3 x 3 median filter to remove shot noise from the images. Some analysis required conversion to 8-bit data structures. The 8-bit conversion was a requirement of the software such that they could be analyzed using the Graphical Slicer.
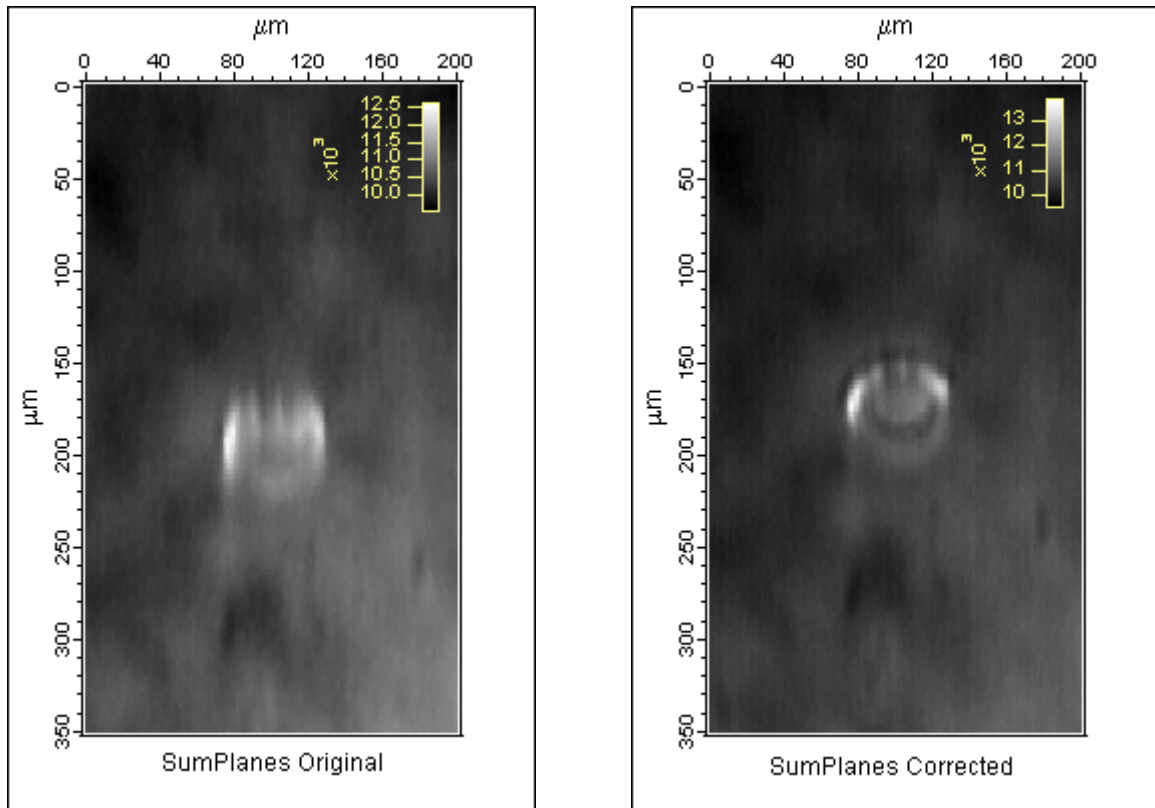
Figure 3.2. Sum of all the images in a scan (left) before and (right) after image shift correction.

The IGOR pro graphical slicer is a tool to analyze a 3D data structure by extracting XY, Yθ or Xθ slices. All the other analysis besides the graphical slicer analysis was done on 16 bit TIFF images.

Figures 3.3, 3.4 and 3.5 show screenshots of the Graphical Slicer which show how a XY, Yθ or an Xθ slice can be viewed from a 3D data structure. The image on the left side of a screenshot shows the 3D data structure and the image on the right side shows the slice chosen. In this way each slice can be previewed before extracting it.
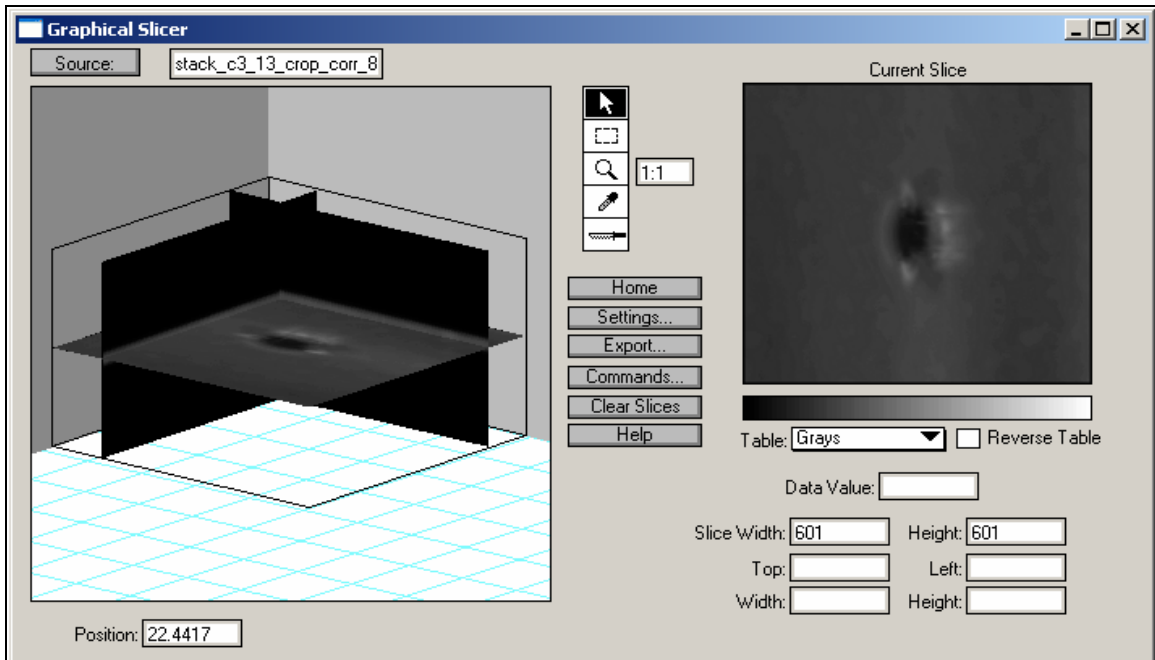
Figure 3.3. Screenshot of the graphical slicer showing an XY slice from a 3D data structure.
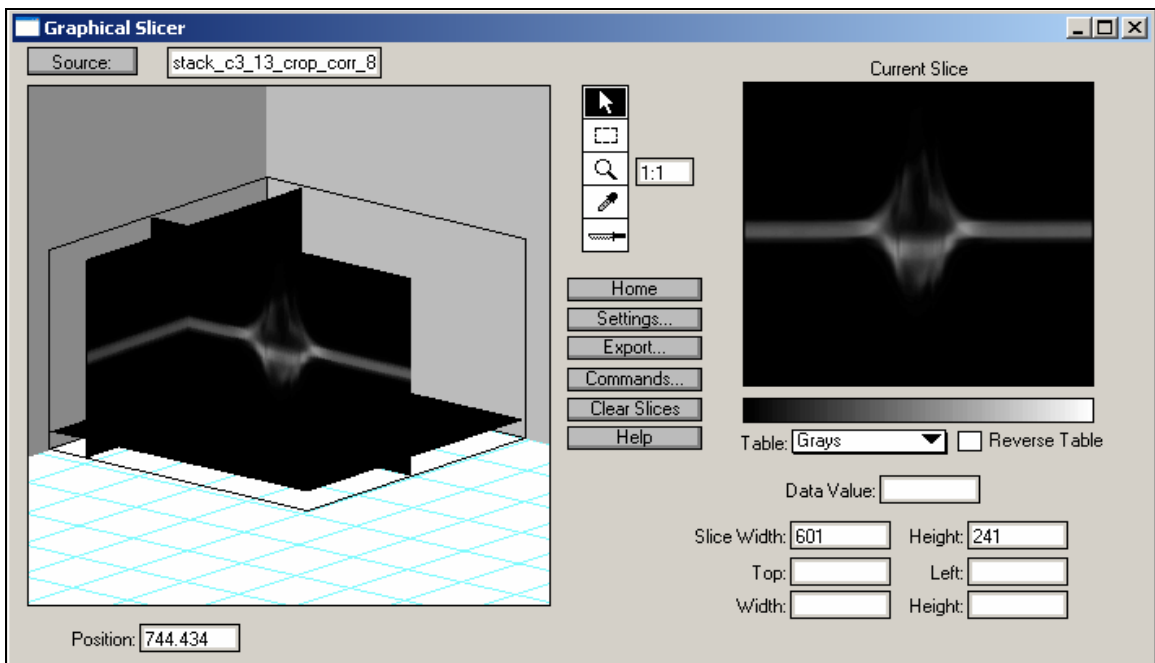
Figure 3.4. Screenshot of the graphical slicer showing an Xθ slice from a 3D data structure.
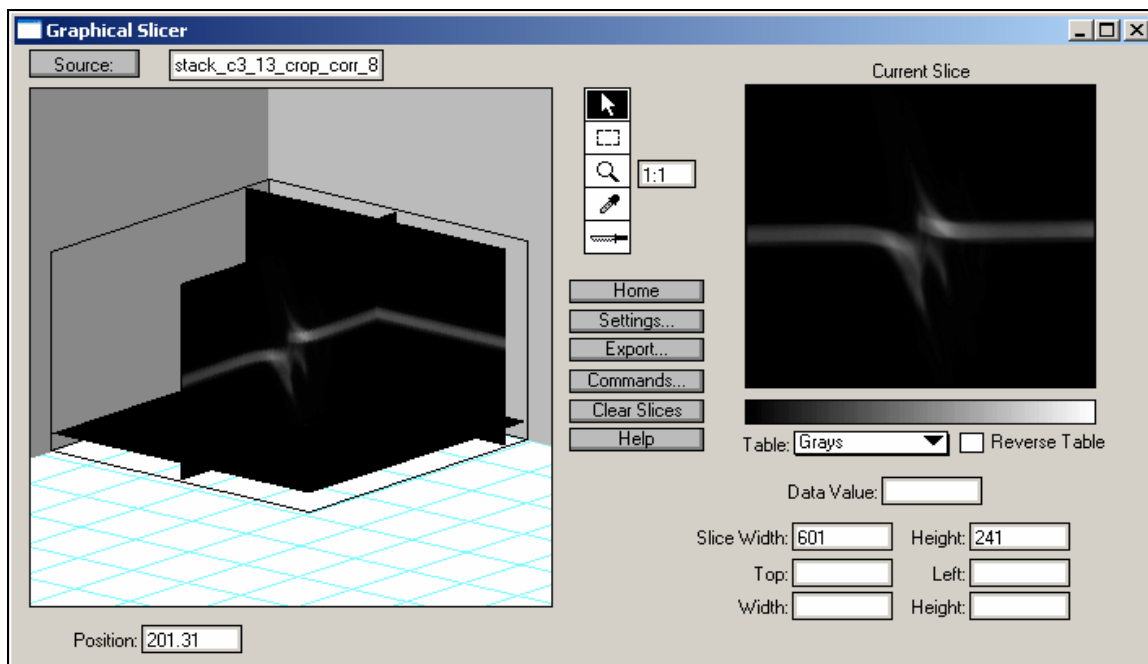
Figure 3.5. Screenshot of the graphical slicer showing a Yθ slice from a 3D data structure.

A line scan in the vertical direction in an Xθ or Yθ slice corresponds to the rocking curve of one pixel. A rocking curve is a plot of intensity verses the rocking angle. A rocking curve gives us useful information about the crystal. Figure 3.6 shows a rocking curve of the crystal at a location far away from the damaged region. This rocking curve of one pixel is extracted from the X axis of the Xθ slice. This rocking curve is an almost symmetric bell shaped curve and peaks only once with smooth tails and a full-width at half maximum (FWHM) of 11.6 arc sec. Figure 3.7 shows a rocking curve of the same crystal at the center of the damaged region. This curve is a highly asymmetric curve with multiple peaks and uneven tails and a FWHM of 31.4 arc sec.

Rocking curves show variation from the undamaged material based on crystal damage and other factors and can hence be used as a tool to analyze the damage in crystals.
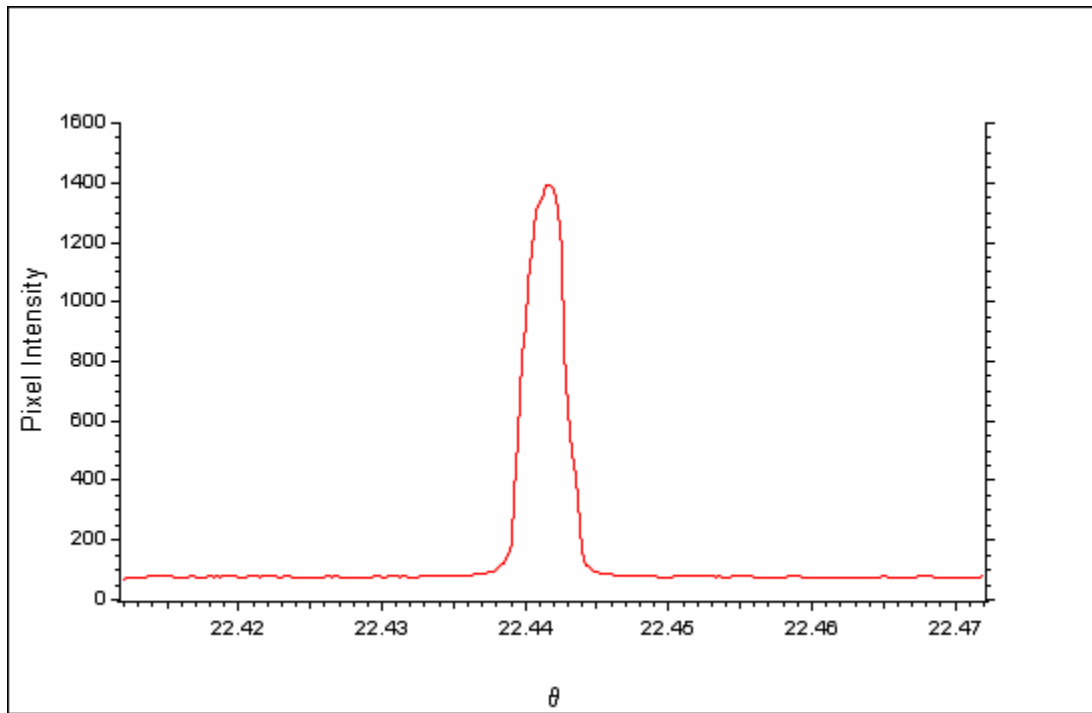
Figure 3.6. Undamaged crystal rocking curve of Si 0 0 4 taken away from the damaged region.
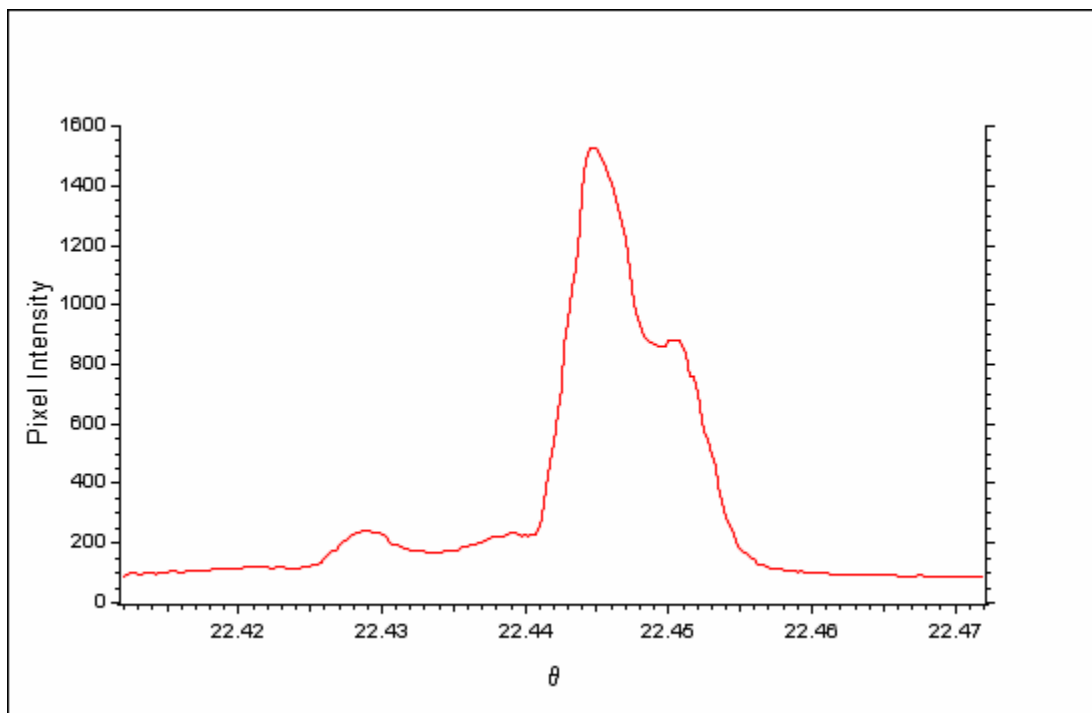
Figure 3.7. Damaged region rocking curve of Si 0 0 4 taken at the center of the damaged region.

36

Based on the outline in Table 3.1, micrographs and topographs slices for each of the laser irradiated spots listed were examined. Each of the laser spots will be discussed in detail with respect to topograph damage analysis using characterizations and moments, topograph vs. micrograph feature size comparison, femtosecond vs. nanosecond damage comparison, damage comparison for different diffraction peaks, high peak laser fluence vs. low peak laser fluence damage comparison and rocking curve comparisons.

3.3   High Peak Fluence Femtosecond Laser Spot, 4.83 J/cm^2

The following section will deal with optical micrographs, electron micrographs and topographs of a femtosecond laser spot irradiated with a peak fluence of 4.83 J/cm^2. Two sets of experiments were conducted on this spot, one set in November 2003 and one set in April 2004.

3.3.1   Optical and Electron Microscopy

Figures 3.8 and 3.9 show optical and scanning electron micrographs (SEM) of the high fluence femtosecond laser spot irradiated with 100 pulses, peak fluence on the spot being 4.83 J/cm^2. Care was taken to orient the micrographs in the same orientation as the $00\bar{4}$ X-ray topographs so that a valid comparison can be made between the features being examined.

The horizontal size of the spot or crater in the optical micrographs is 68 μm with damage spreading horizontally as much as 108 μm. The vertical size of the spot or crater is about 62 μm with damage extending out to 92 μm. The pixel readings on the edges of the feature and the resolution of the micrographs were used to determine the feature sizes. A horizontal and vertical linescan across the center of the micrograph reveals the contrast in more detail. Linescans are light intensity readings on the photographs and not a surface profile.

Figures 3.10 and 3.12 show horizontal and vertical linescans across the center of the irradiated spot on the optical micrograph. The horizontal size of the spot or crater in the SEM is 70 μm with damage spreading horizontally as much as 104 μm. The vertical size of the spot or crater is about 64 μm with damage extending out to 92 μm.

Figures 3.11 and 3.13 show horizontal and vertical linescans across the center of the irradiated spot on the SEM. The linescan shows the maximum width and height profiles of the damage.
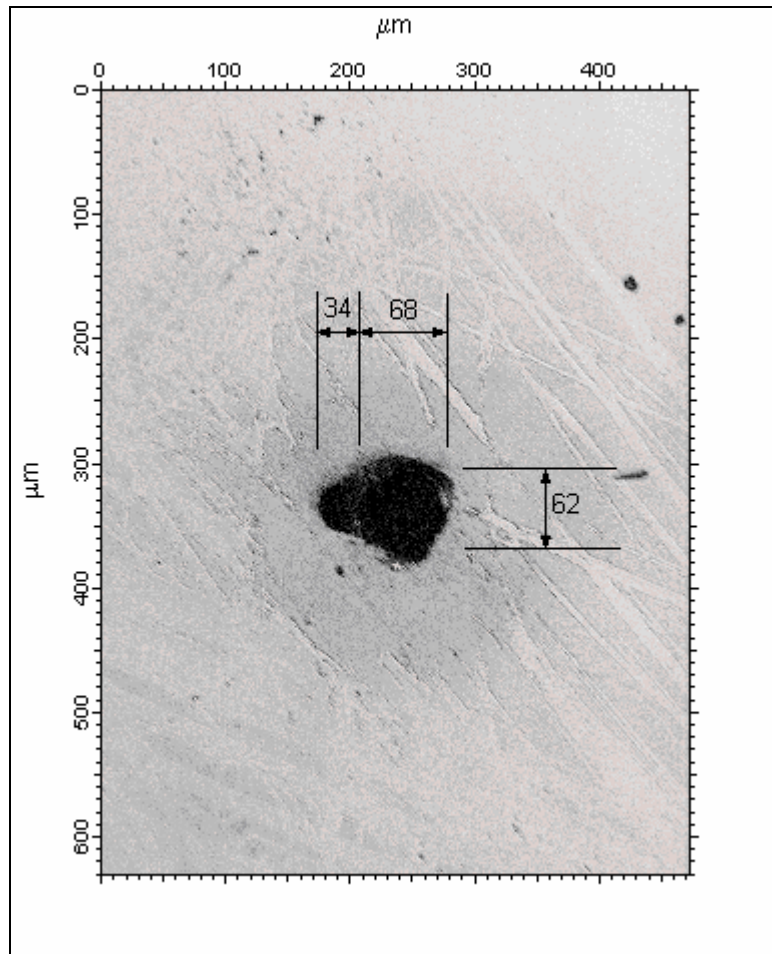
Figure 3.8. Optical micrograph showing feature size of high peak fluence (4.83 J/cm^2) femtosecond laser spot.
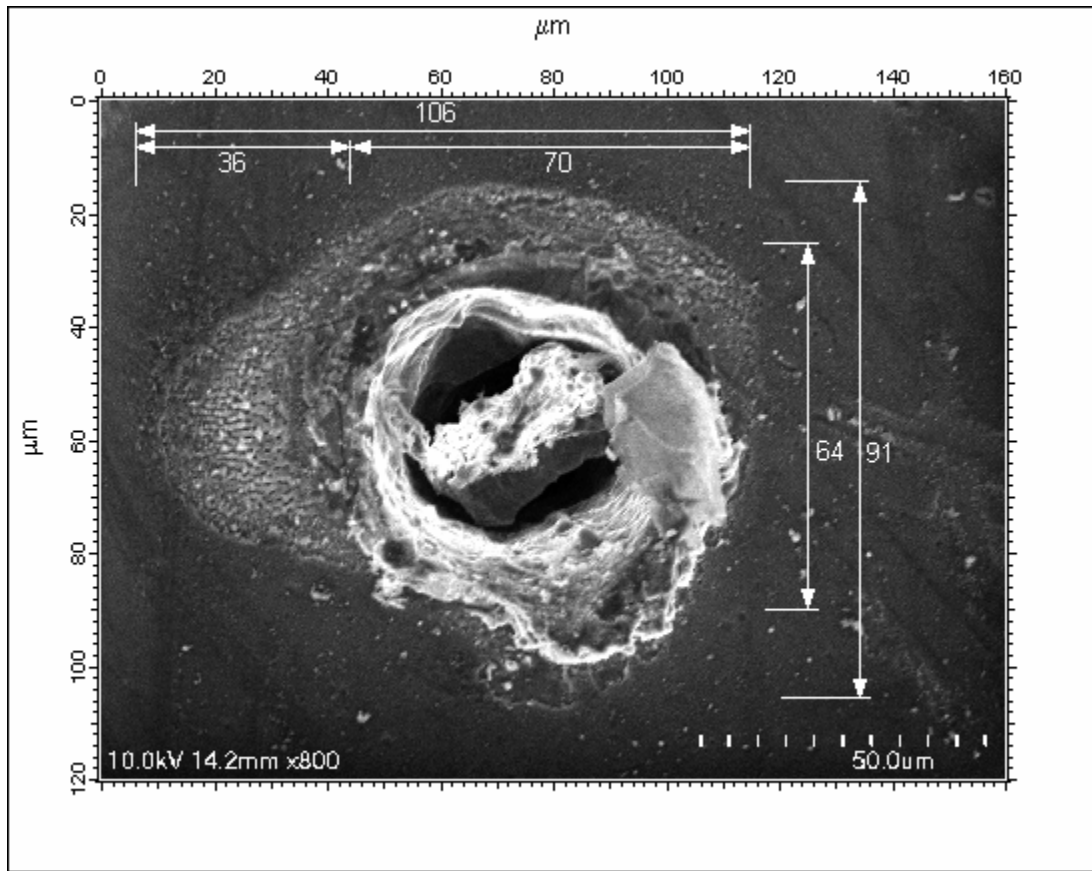
Figure 3.9. SEM showing feature size of high peak fluence (4.83 J/cm^2) femtosecond laser spot.
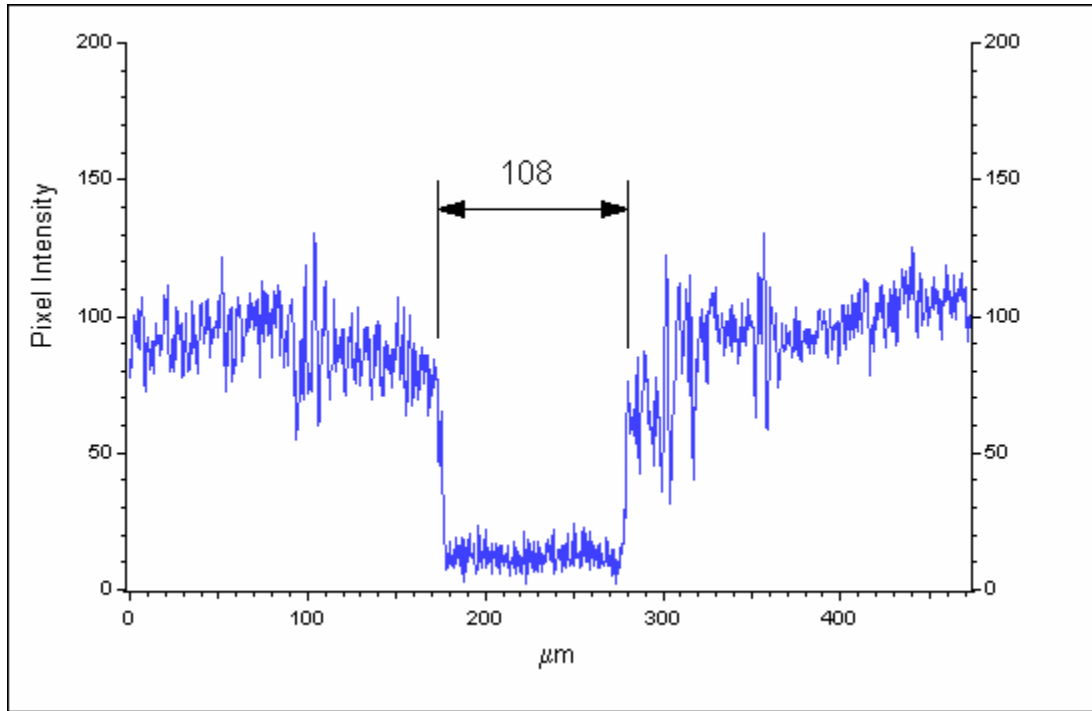
Figure 3.10. Horizontal linescan across optical micrograph of high peak fluence fs laser spot, showing feature size.
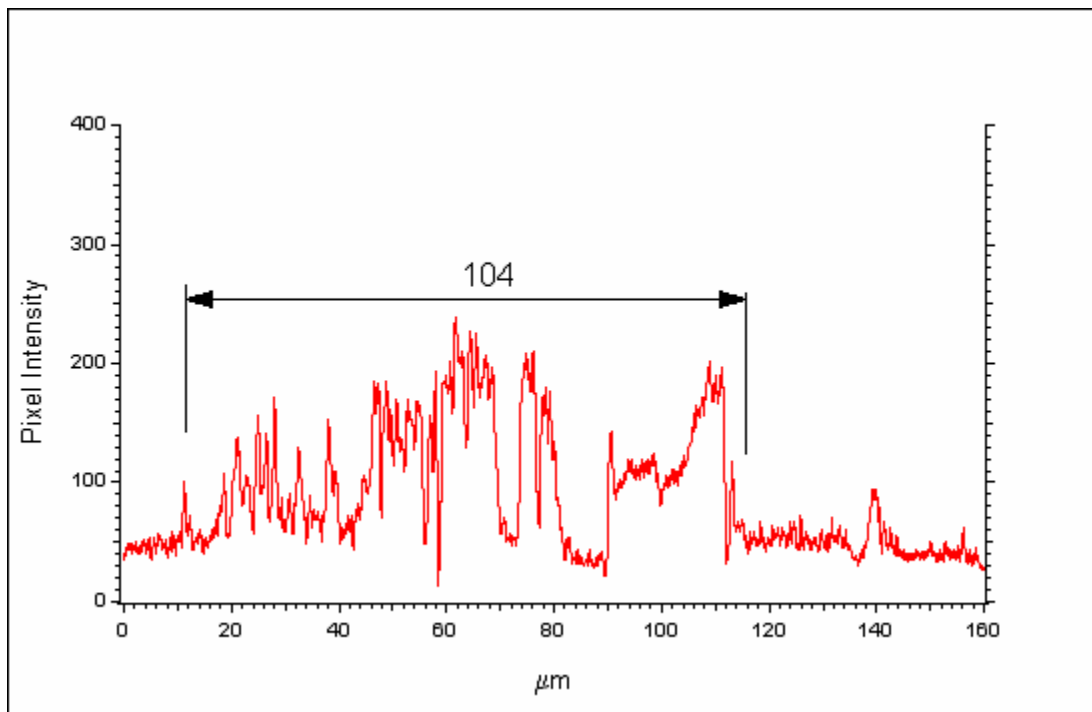
Figure 3.11. Horizontal linescan across SEM of high peak fluence fs laser spot, showing feature size
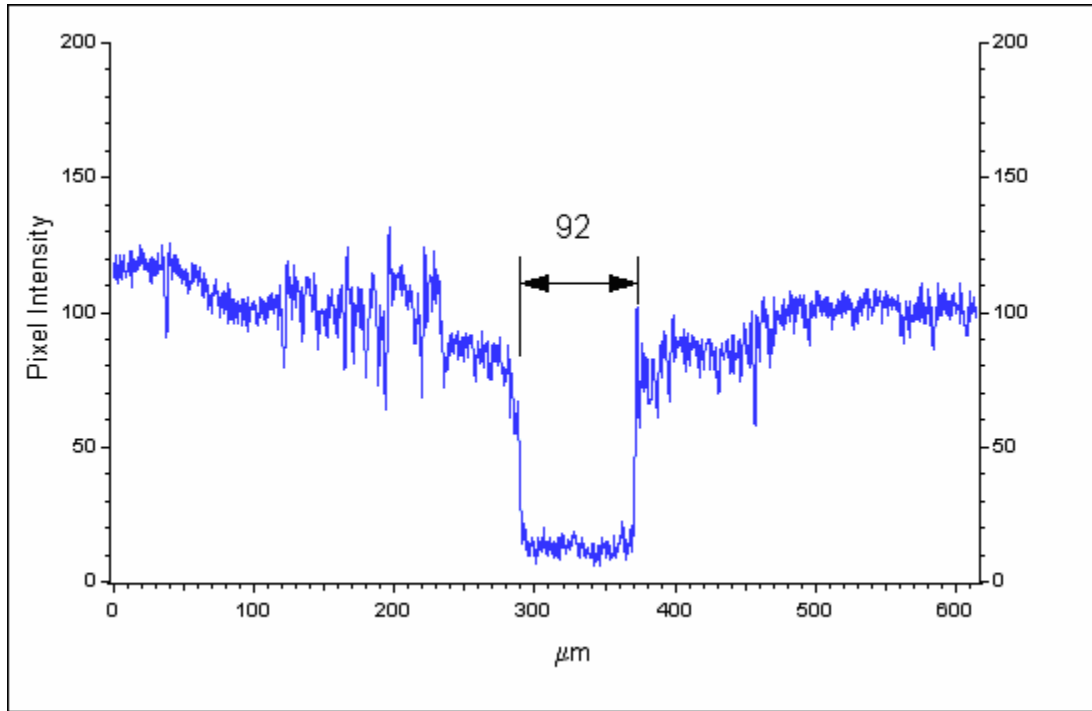
Figure 3.12. Vertical linescan across optical micrograph of high peak fluence fs laser spot, showing feature size.
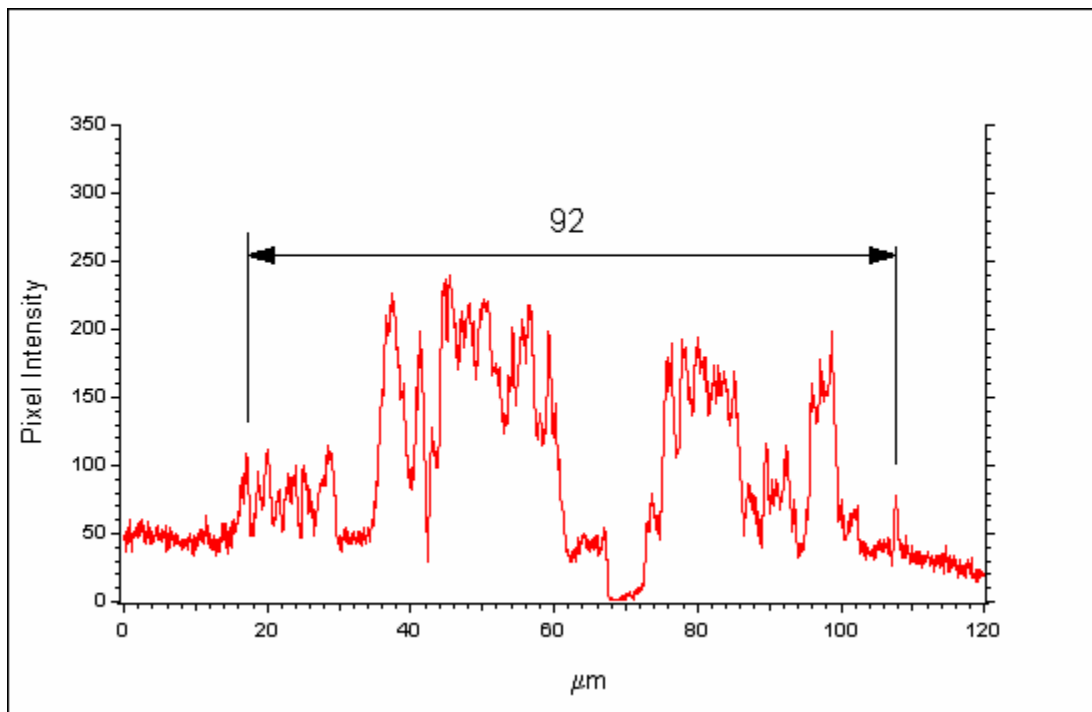
Figure 3.13. Vertical linescan across SEM of high peak fluence fs laser spot, showing feature size.

3.3.2   Topography – Trial 1 (April 2004) - $0\,0\,4$

The following section deals with the topographs of the femtosecond irradiated laser spot, with an h k l of $0\,0\,4$. The topographs presented in this section were obtained during experimentation in April 2004 at the APS. The camera was at a radius of 47 mm from these topographs. Since the crystal is an $1\,0\,0$ oriented crystal, the $0\,0\,4$ diffraction geometry was symmetric in the diffraction plane.

3.3.2.1 Slice Analysis

Figure 3.14 is an XY slice at the peak of the rocking curve. The XY slice is an image of the crystal diffracting at its Bragg peak, as seen by the CCD camera.
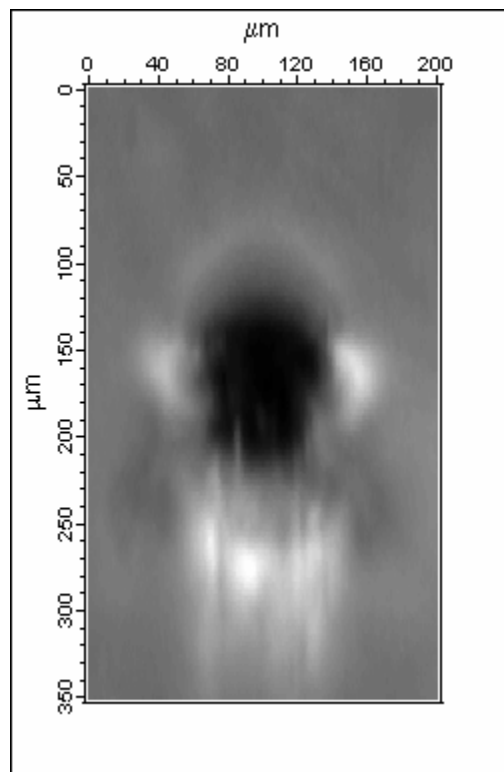
Figure 3.14. XY slice of high peak fluence fs laser spot $0\,0\,4$ at the center of the Bragg peak showing damage, as seen by the CCD camera.

Figure 3.15 is an image of the Xθ slice with adjusted intensity range showing the extent of diffracted intensity in the horizontal direction. The Xθ slice is extracted approximately across the center of the feature at a Y coordinate of 175 μm of the XY slice. The superimposed red line across the image is the image line profile that shows the change in intensity along the horizontal direction across the feature at a θ value of 22.4415°. The damage horizontally extends to 189 μm, which is about 1.75 times more than the damage as seen in the optical micrograph and SEM. The optical micrograph feature size of 68 μm is also marked in this slice. This spread of damage shows that the effects induced by the high fluence femtosecond laser beam extend beyond what can be seen on the surface with a microscope.

Figure 3.16 is an image of the Yθ slice with adjusted intensity range showing the extent of contrast in the vertical direction. The Yθ slice is extracted at X coordinate of 100 μm of the XY slice. The damage in the vertical direction across the feature measures 416 μm, which is about 4.5 times more than the feature size as seen in the optical micrograph and SEM. The extent of the contrast seen in the vertical plane is more than the horizontal plane since the measurements are more sensitive to strain and lattice rotation in the diffraction plane and broadened by the width of the rocking curve by the diffraction process.
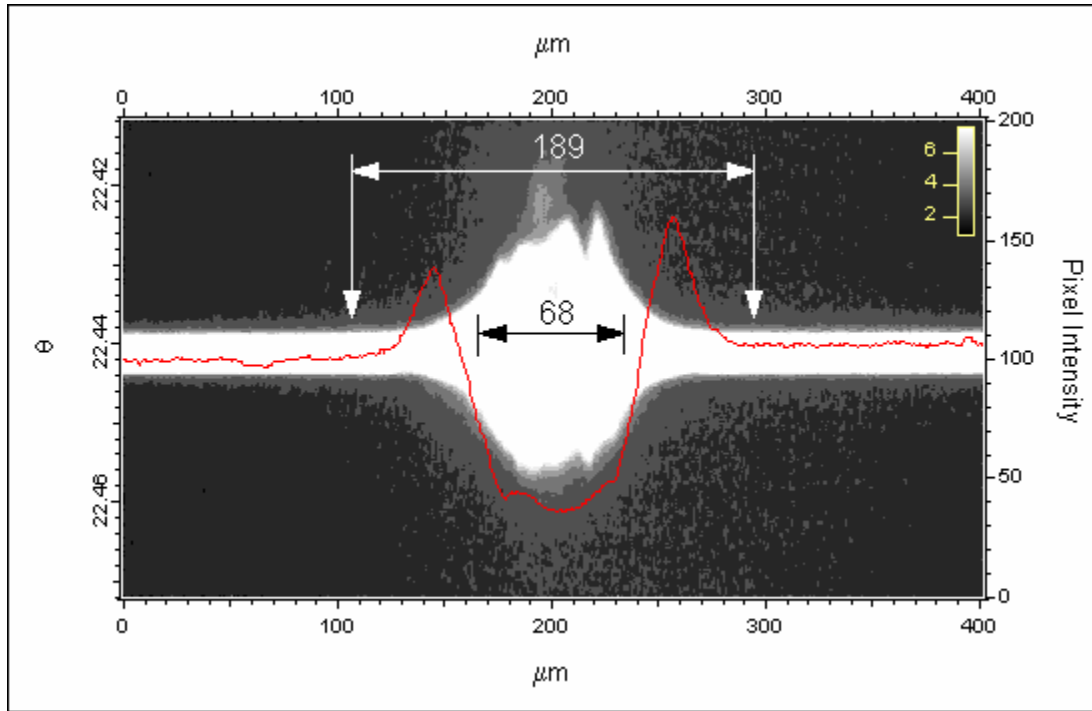
Figure 3.15. Xθ slice of high peak fluence fs laser spot 0 0 4 showing region of horizontal damage. The Xθ slice is taken at a Y value of 175 μm on the XY slice.
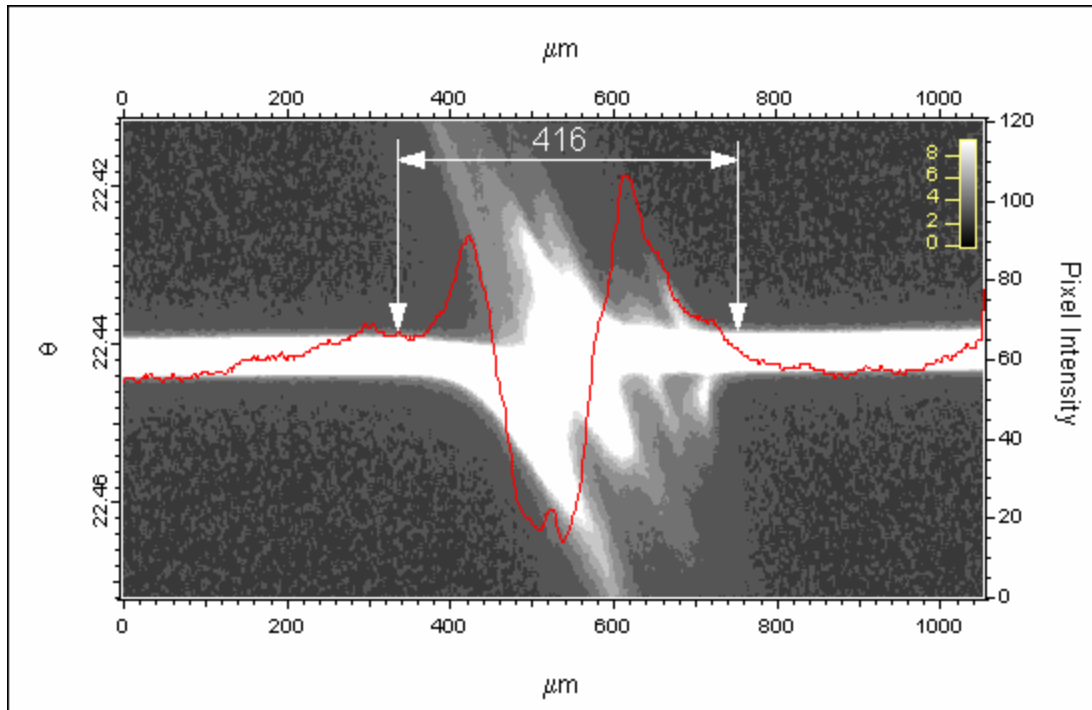
Figure 3.16. Yθ slice of high peak fluence fs laser spot 0 0 4 showing region of vertical damage. The Yθ slice is taken at an X value of 100 μm on the XY slice.

Figure 3.17 shows an Xθ slice extracted approximately across the center of the feature at a Y coordinate of 175 μm of the XY slice. The lines A, B, C, D, E, F & G trace the path of a single pixel through the entire rocking angle and thus represent rocking curves. A is the rocking curve of the undamaged crystal that is recorded at 10 μm on slice Xθ, far away from the extent of the strain field in the horizontal direction. B & G are recorded at the peak value of intensity in the horizontal direction and C, D, E & F are rocking curves that show various different behaviors than the rest of the rocking curves. Figures 3.18, 3.19 and 3.20 show the comparisons of different rocking curves and Table 3.2 gives the data recorded from the seven rocking curves.
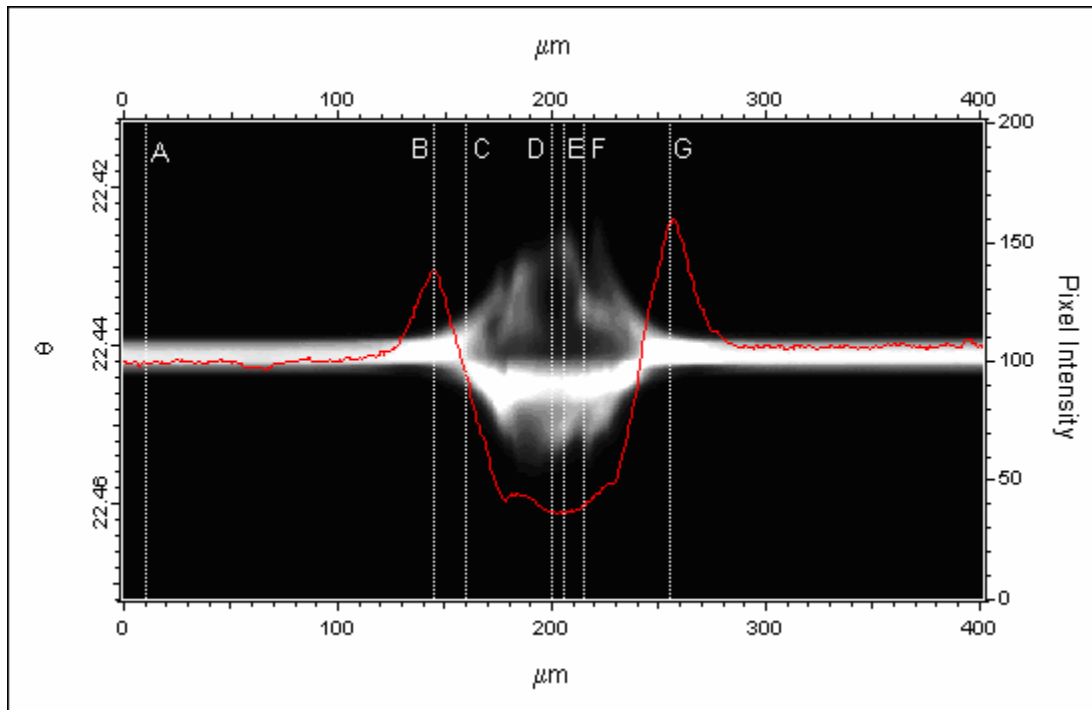
Figure 3.17. Xθ slice of high peak fluence fs laser spot 0 0 4 showing positions of rocking curves A, B, C, D, E, F & G. The Xθ slice is taken at a Y value of 175 μm of the XY slice.
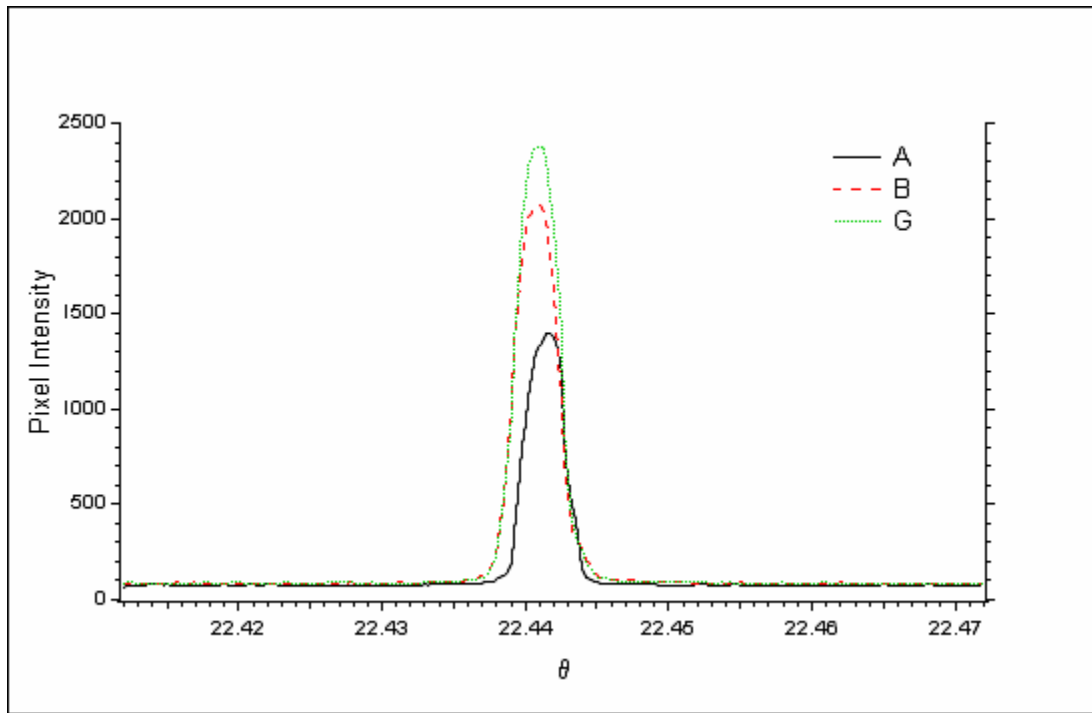
Figure 3.18. Comparison of rocking curves A, B & G of high peak fluence fs laser spot $0\,0\,4$.
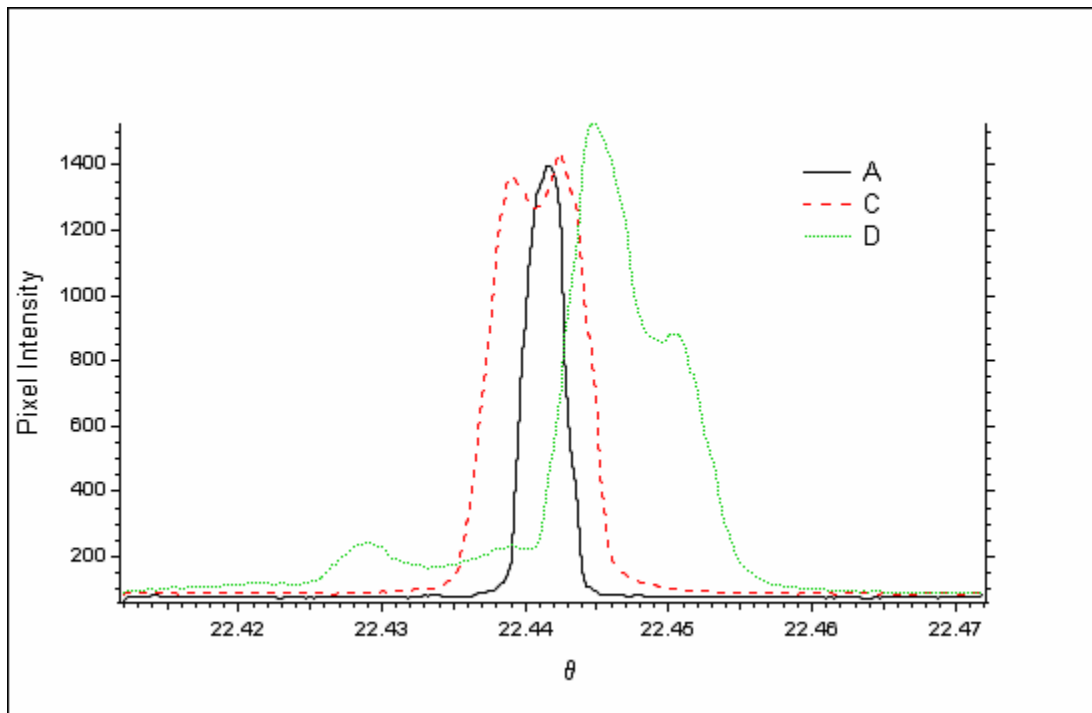
Figure 3.19. Comparison of rocking curves A, C & D of high peak fluence fs laser spot $0\,0\,4$.
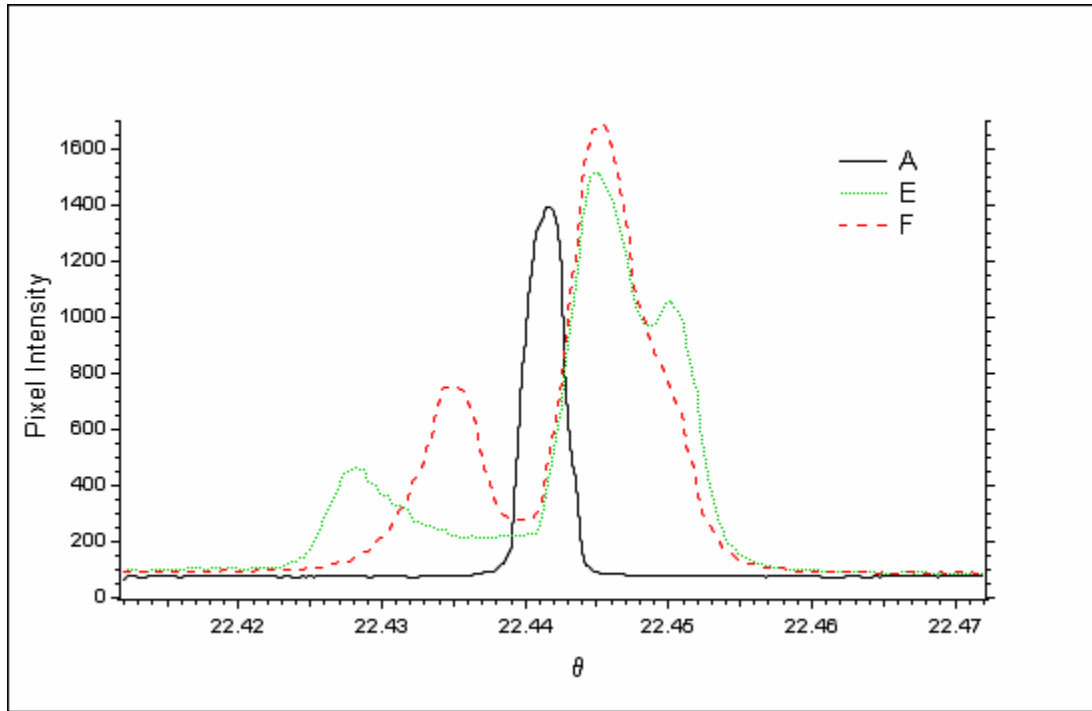
Figure 3.20. Comparison of rocking curves A, E & F of high peak fluence fs laser spot 004.

Table 3.2. Rocking curve details of high peak fluence fs laser spot 004.

Rocking Curve	Rocking Curve Position (μm)	Peak Intensity	Background Intensity	FWHM (arc sec)	$\dfrac{\text{FWHM (Curve)}}{\text{FWHM (A)}}$
A	10	1394	65	11.56	1.00
B	145	2073	82	12.32	1.07
C	160	1430	83	27.25	2.36
D	200	1525	87	31.36	2.71
E	206	1513	85	32.00	2.77
F	215	1683	82	22.59	1.95
G	255	2378	83	12.29	1.06

It can be seen in Table 3.2 and in Figure 3.18, the FWHM of the rocking curves, B and G, outside the crater are almost the same as that of the rocking curve, A, of the undamaged crystal and show very little variation. There is only a difference in the peak intensity of each of them which are supported from the linescans. Rocking curve C is at a location where the curve starts to behave differently than curve B. It can be seen that

48

rocking curve C has a notch at the peak and this notch becomes wider as it progresses through locations D, E and F. It is also seen that the FWHM of rocking curves of C, D, E and F are almost two times or more, than the FWHM of the undamaged crystal. It can hence be seen that the rocking curves can be used to characterize damage in the crystal.

3.3.2.2 Image Analysis on Rocking Curve Characterizations

In this section topograph analysis rocking curves were extracted from each pixel of the XY axes of the 3D data structures through the rocking angle (Z axis or θ axis). These rocking curves were then used to calculate certain characterizations. N new 2-dimensional XY images were then reconstructed pixel by pixel using these characterizations from rocking curves. Figures 3.21 and 3.22 show characterization images for the high peak fluence femtosecond spot. The characterizations used in this analysis are described below.

- *Maximum* denotes the maximum value of Intensity in each of the rocking curve. It has arbitrary units.

- *Standard Deviation (σ)* is given by

$$\sigma = \sqrt{\frac{1}{n-1}\sum(I_i - \text{avg})^2} \tag{3.1}$$

where, n is the number of points in the rocking curve, I_i is the intensity value at location i, and avg is the average of all the y values. It has arbitrary units. This is not a measure of the width of the rocking curve; the rocking curve angles are not included in this statistic.

- *FWHM* is the Full Width at Half Maximum of the rocking curve. Its units are in arc seconds.

- *Maximum location* is the θ location of the maximum intensity value of the rocking curve. Its units are in degrees.

- *Skewness* is a measure of symmetry, or more precisely, the lack of symmetry of a distribution, or data set. This is not a measure of the width of the rocking curve; the rocking curve angles are not included in this statistic. *Skewness* is given by

$$Skew = \frac{1}{n}\sum_{i=0}^{n-1}\left[\frac{I_i - \bar{I}}{\sigma}\right]^3 \qquad (3.2)$$

Its units are arbitrary.

- *Kurtosis* is given by

$$Kurtosis = \frac{1}{n}\sum_{i=0}^{n-1}\left[\frac{I_i - \bar{I}}{\sigma}\right]^4 - 3 \qquad (3.3)$$

This is not a measure of the width of the rocking curve; the rocking curve angles are not included in this statistic. Its units are arbitrary.

- *Integral* represents the 0th moment of a distribution given by

$$\mu_0 = \sum_i I_i \qquad (3.4)$$

This gives us the sum of all the Y values of a distribution. Its units are arbitrary.

- *Center of Gravity* represents the 1st moment of a distribution given by

$$\mu_1 = \frac{\sum_i \theta_i I_i}{\sum_i I_i} \qquad (3.5)$$

Its units are in degrees.

- *Moment 2* represents the 2nd moment about the center of gravity of a distribution given by

$$\mu_2 = \frac{\sum_i (\theta_i - \mu_1)^2 I_i}{\sum_i I_i} \tag{3.6}$$

Its units are arbitrary.

- *Moment 3* represents the 3rd moment about the center of gravity of a distribution given by

$$\mu_3 = \frac{\sum_i (\theta_i - \mu_1)^3 I_i}{\sum_i I_i} \tag{3.7}$$

Its units are arbitrary. The 3rd moment is sensitive to asymmetry in the rocking curve, being positive for skew right and negative for skew left.

- *Moment 4* represents the 4th moment about the center of gravity of a distribution given by

$$\mu_4 = \frac{\sum_i (\theta_i - \mu_1)^4 I_i}{\sum_i I_i} \tag{3.8}$$

Its units are arbitrary. Because it takes the fourth power of values away from the center of gravity, the fourth moment is sensitive to differences in the tails of the rocking curves than the other characterizations.
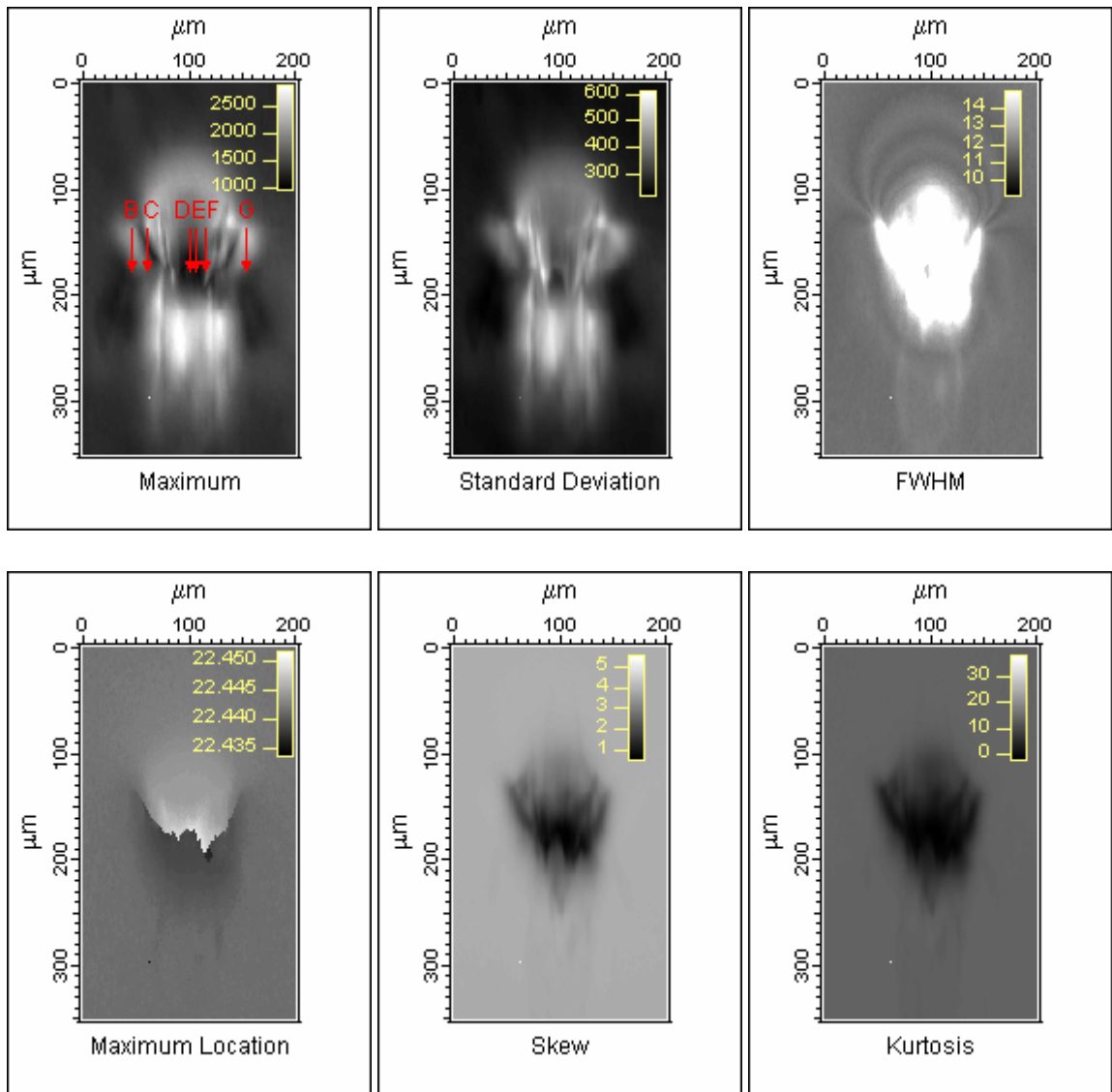
Figure 3.21. High peak fluence fs laser spot 0 0 4 images showing characterizations Maximum, Standard Deviation, FWHM, Maximum Location, Skew & Kurtosis. The maximum image shows the location of the rocking curves in Figure 3.17, at the arrow head.
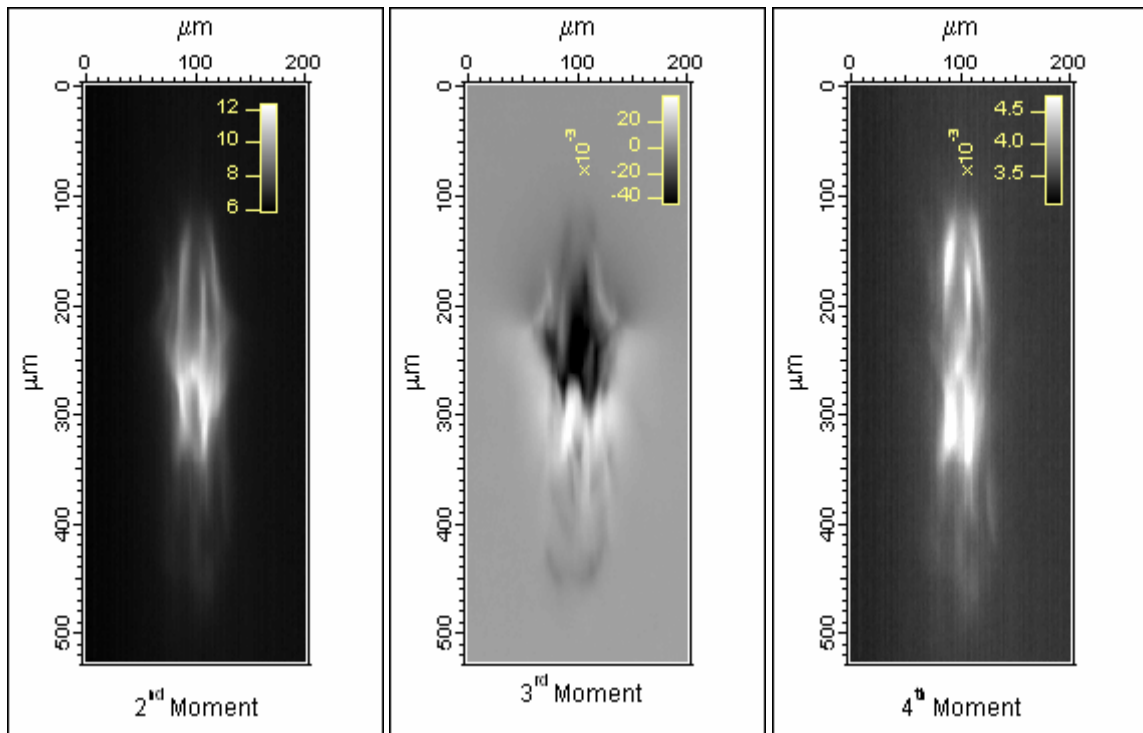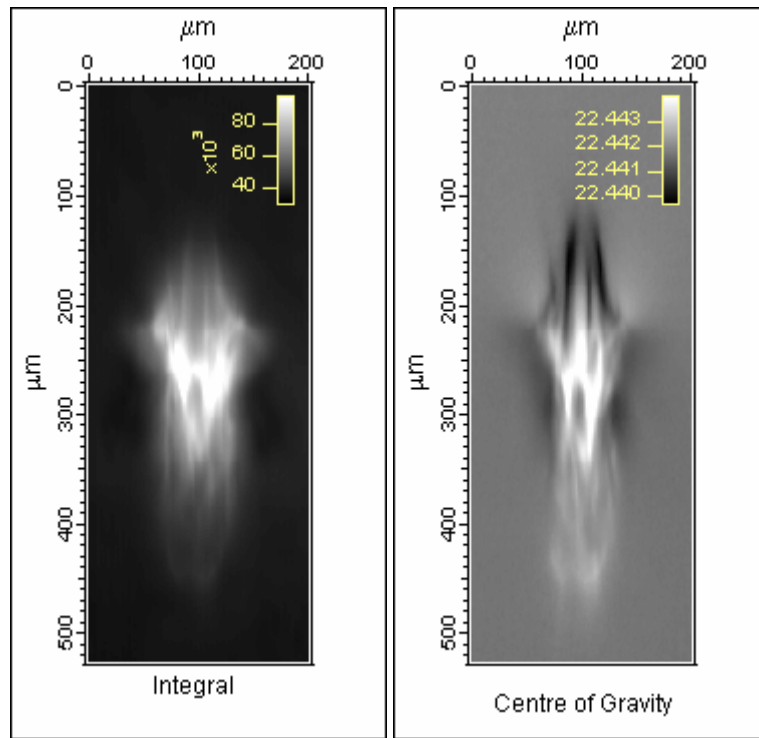
Figure 3.22. High peak fluence fs laser spot 0 0 4 images showing moments Integral and Center of Gravity, 2nd, 3rd & 4th Moment about the Center of Gravity.

Each of the characterization images is useful in analyzing the material damage. It should be noted that they are characterizations of the shape and location of the rocking curves and not ties to structural models of the material and the diffraction process giving rise to the rocking curves. Horizontal and vertical linescans across the center of the image show the extent of the damage in the crystal. The horizontal linescans are taken at a Y location of 175 μm for the characterization images and at a location of 263 μm for the moments images, which is about the horizontal center of the feature. The vertical linescans are taken at an X location of 100 μm for both sets of images. It can be seen that the linescans at the same position across all the characterization images give the same consistent extent of damage. The damage extends horizontally to about 125-130 μm approximately in all the images. Figures 3.23 and 3.24 show the horizontal linescan comparisons across the characterizations images and Figures 3.25 and 3.26 show the horizontal linescan comparisons across the moments images.

Figures 3.27 and 3.28 show the vertical linescan comparisons across the characterizations images and Figure 3.29 and 3.30 the show the vertical linescan comparisons across the moments images. As discussed before the damage in the vertical plane shows up more than that in the horizontal plane due to the greater sensitivity in the diffraction plane. It can be noticed that the vertical scale of the moments images is larger than the characterization images. This scale was increased since the moments images showed more vertical damage than the characterization images. In Figure 3.27 it can be noticed that the maximum location graph makes a sharp transition at 170 μm. Interestingly in Figure 3.28 the FWHM graph makes a similar sharp transition at 170 μm showing consistency in the details revealed by the characterization and moments images.

Looking at the Maximum Location curve and corresponding image, we see that the upper portion of the damaged region shows a maximum in the rocking curves at higher angles while the lower portion show their maximum at lower angles. Both effects gradually die off as you go way from sharp transition. Interestingly, the center of gravity of the rocking curves show a much different behavior. Because the rocking curves get very asymmetrical in the middle of the damaged region, the maximum location and center of gravity behave differently.
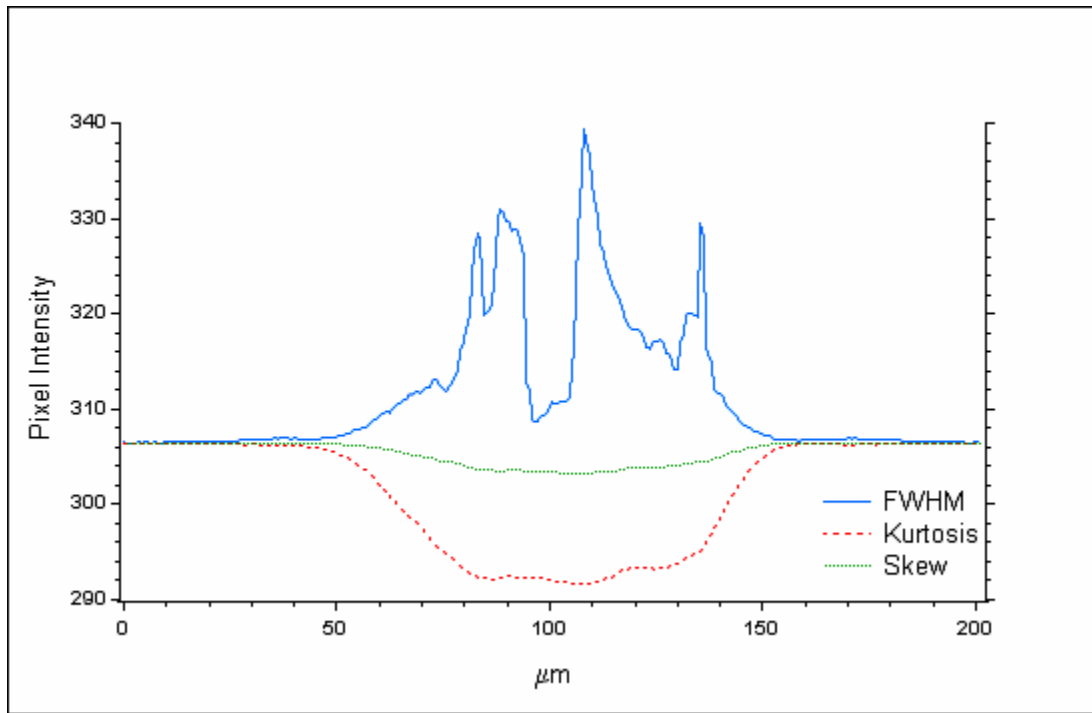
Figure 3.23. Horizontal linescans across FWHM, Kurtosis and Skew images, showing extent of damage across the center of the feature.
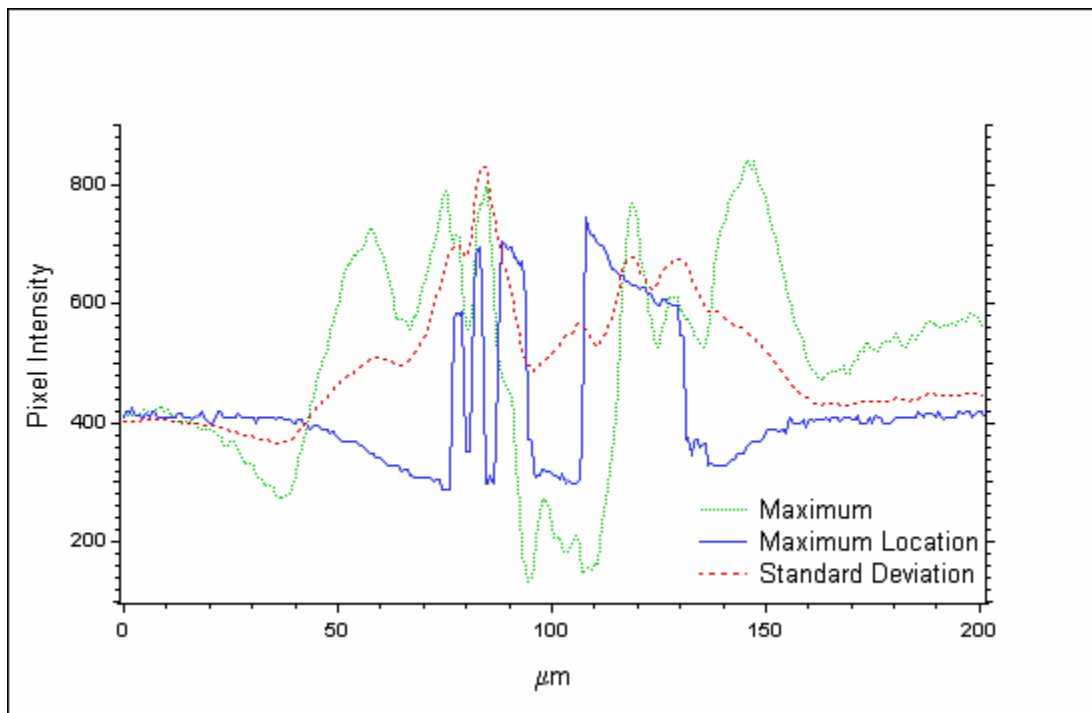
Figure 3.24. Horizontal linescans across Maximum, Maximum Location and Standard Deviation images, showing extent of damage across the center of the feature.
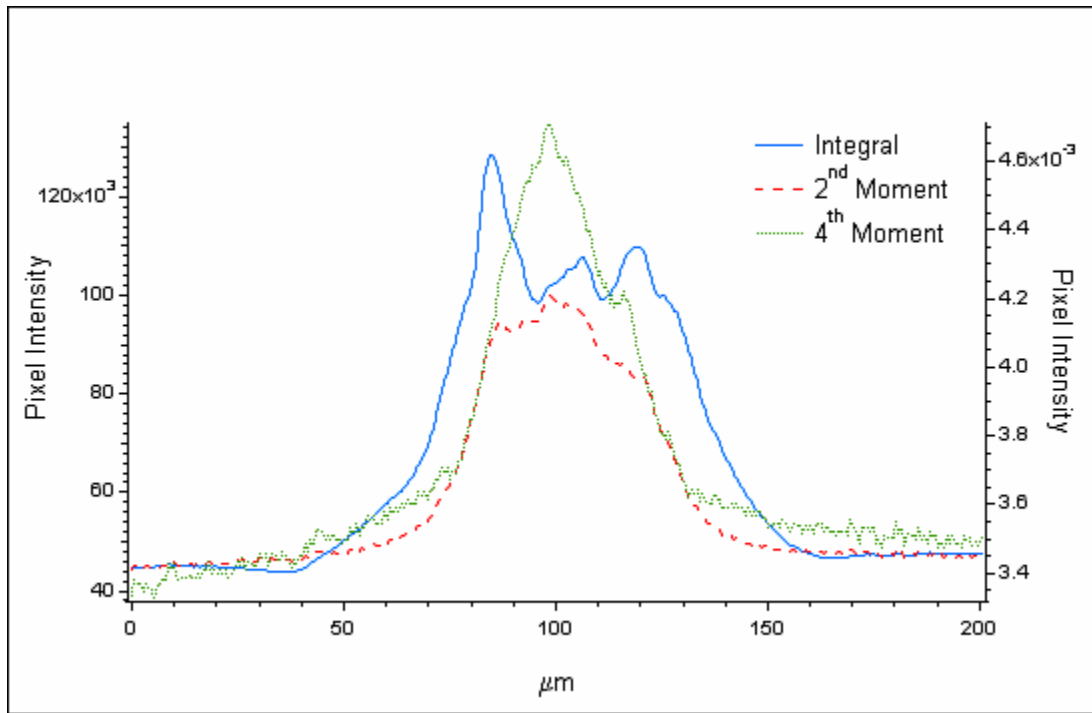
Figure 3.25. Horizontal linescans across Integral, 2nd and 4th Moment images, showing extent of damage across the center of the feature.
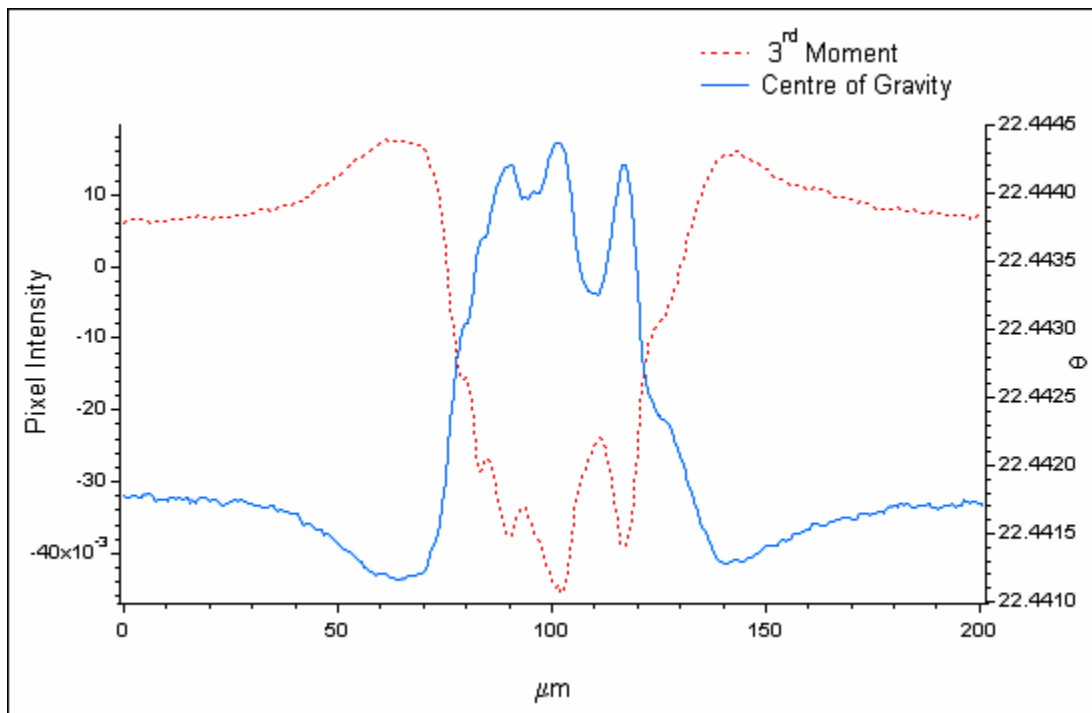
Figure 3.26. Horizontal linescans across 3rd Moment and Center of Gravity images, showing extent of damage across the center of the feature.
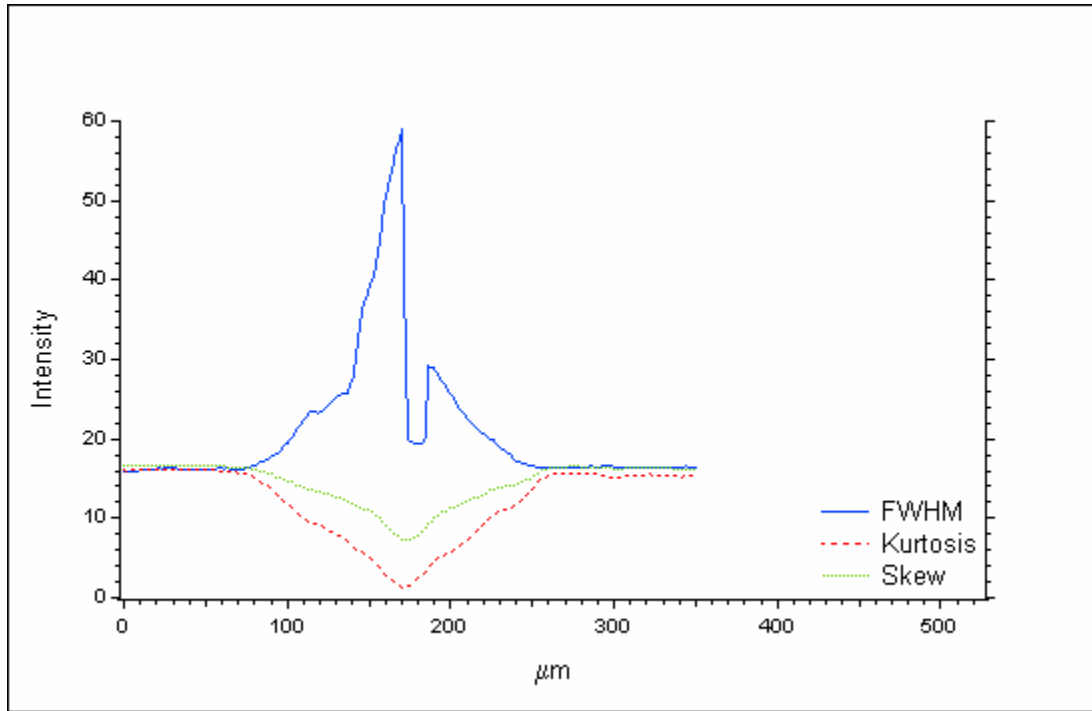
Figure 3.27. Vertical linescans across FWHM, Kurtosis and Skew images, showing extent of damage across the center of the feature.
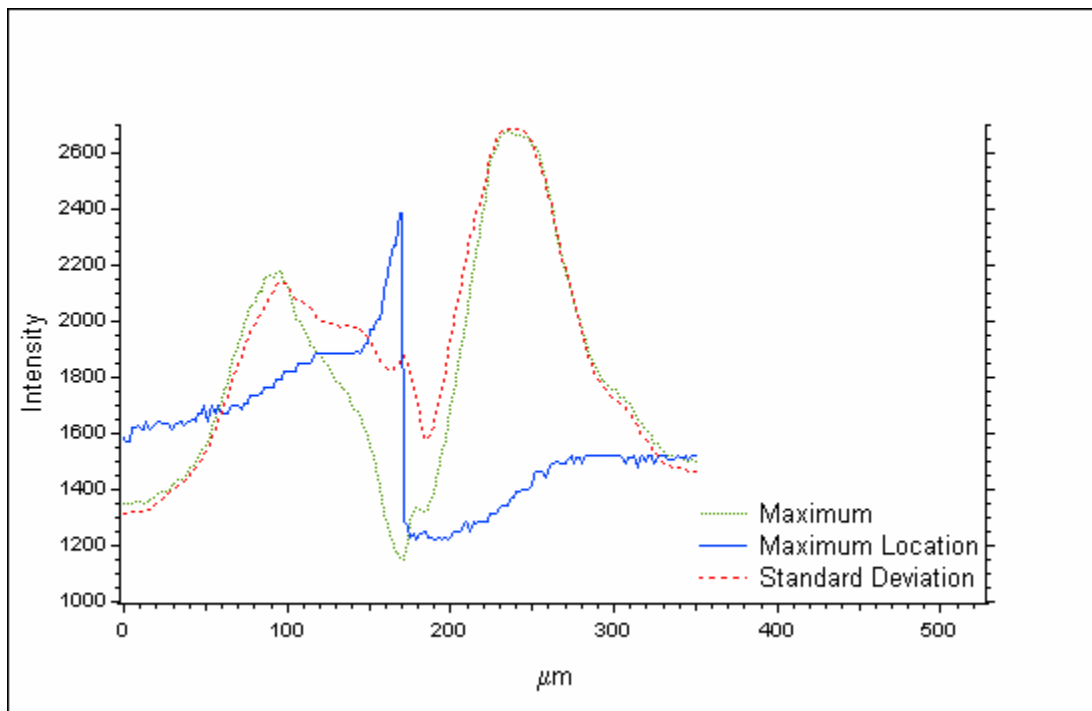
Figure 3.28. Vertical linescans across Maximum, Maximum Location and Standard Deviation images, showing extent of damage across the center of the feature.

59
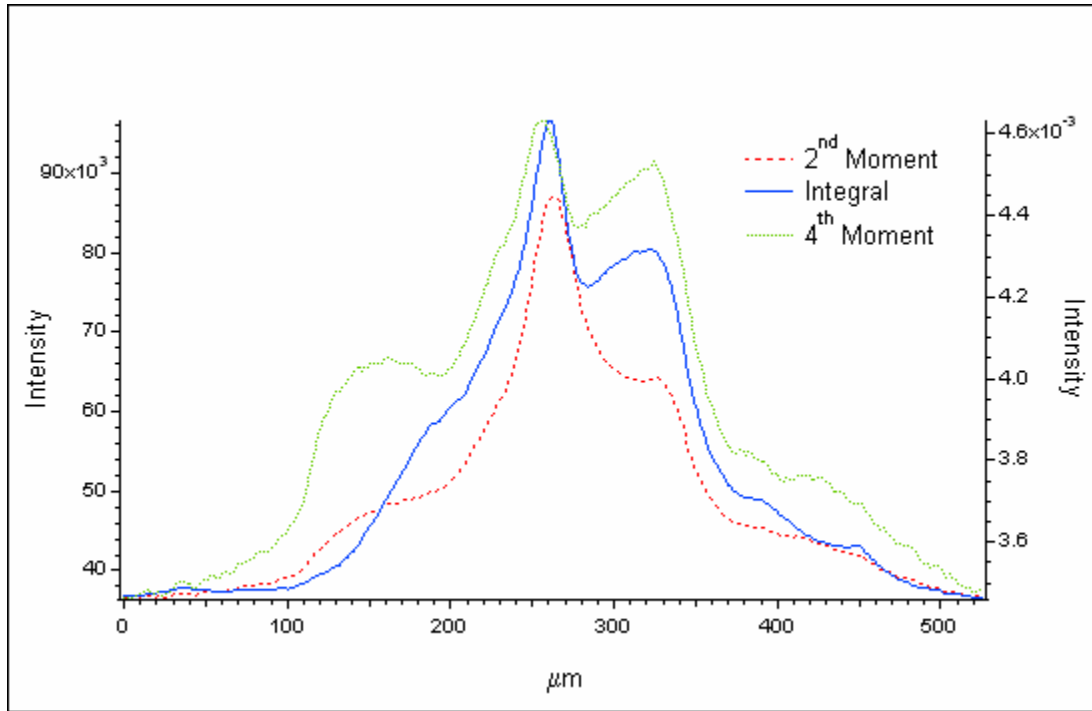
Figure 3.29. Vertical linescans across Integral, 2nd and 4th Moment images, showing extent of damage across the center of the feature.
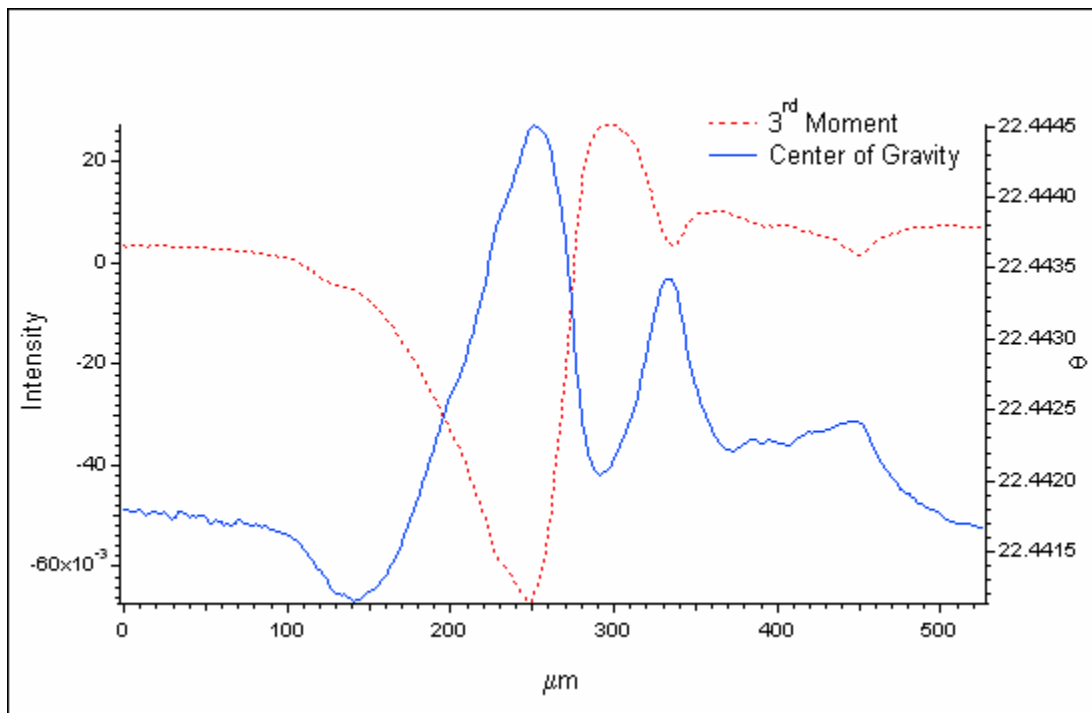
Figure 3.30. Vertical linescans across 3rd Moment and Center of Gravity images, showing extent of damage across the center of the feature.

3.3.3 Topography – Trial 2 (November 2003) - $\bar{1}\bar{1}5$

The following section deals with the topographs of the femtosecond irradiated laser spot, with an h k l of $\bar{1}\bar{1}5$. The topographs presented in this section were obtained during experimentation in November 2003 at the APS. Since the crystal is an $1\,0\,0$ oriented crystal, the $\bar{1}\bar{1}5$ peak was done in asymmetrical geometry as explained in the experimental section. The azimuth for the viewpoint of these topographs is 45˚ from the $0\,0\,4$ topographs of the same spot. The topographs in this section can be used effectively to draw comparisons with the topographs taken in April 2004.

3.3.3.1 Slice Analysis

Figure 3.31 is an XY slice at the peak of the rocking curve. The XY slice is an image of the crystal diffracting at its Bragg peak, as seen by the CCD camera.
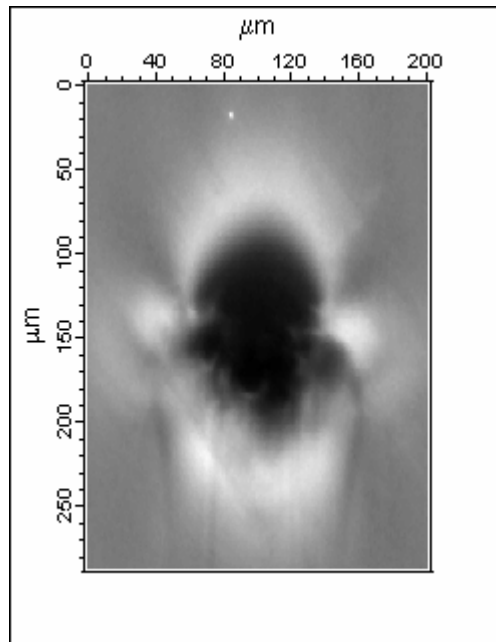
Figure 3.31. XY slice of high peak fluence fs laser spot $\bar{1}\bar{1}5$ at the center of Bragg peak showing damage, as seen by the CCD camera.

61

Figure 3.32 shows the Xθ slice with adjusted intensity range showing the extent of diffracted intensity in the horizontal direction. The Xθ slice is extracted approximately across the center of the feature at a Y coordinate of 143 μm of the XY slice. The superimposed red line across the image is the image line profile that shows the change in intensity along the horizontal direction across the feature at a θ value of 13.92425˚. The damage horizontally extends to 154 μm, which is about 1.4 times more than the feature size as seen in the optical micrograph and SEM. Also this $\bar{1}\bar{1}5$ topograph slice shows a little less horizontal contrast compared to the $0\,0\,\bar{4}$ topograph in Figure 3.15, which shows 189 μm. The extent of the contrast shown may reflect the crystallographic nature of the damage as the two reflections originate from different sets of planes.

Figure 3.33 shows the Yθ slice with adjusted intensity range showing the extent of contrast in the vertical direction. The Yθ slice is extracted at X coordinate of 100 μm of the XY slice. The extent of contrast in the vertical direction across the feature measures 288 μm, which is about 3.1 times more than the feature size as seen in the optical micrograph and SEM. Also this $\bar{1}\bar{1}5$ topograph slice shows less vertical contrast as seen in the $0\,0\,\bar{4}$ topograph in Figure 3.16, which shows 416 μm. The extent of contrast in the diffraction plane is quite different with the two h k l planes. Qualitatively the slices from topographs based on the two different h k l's show many similarities.
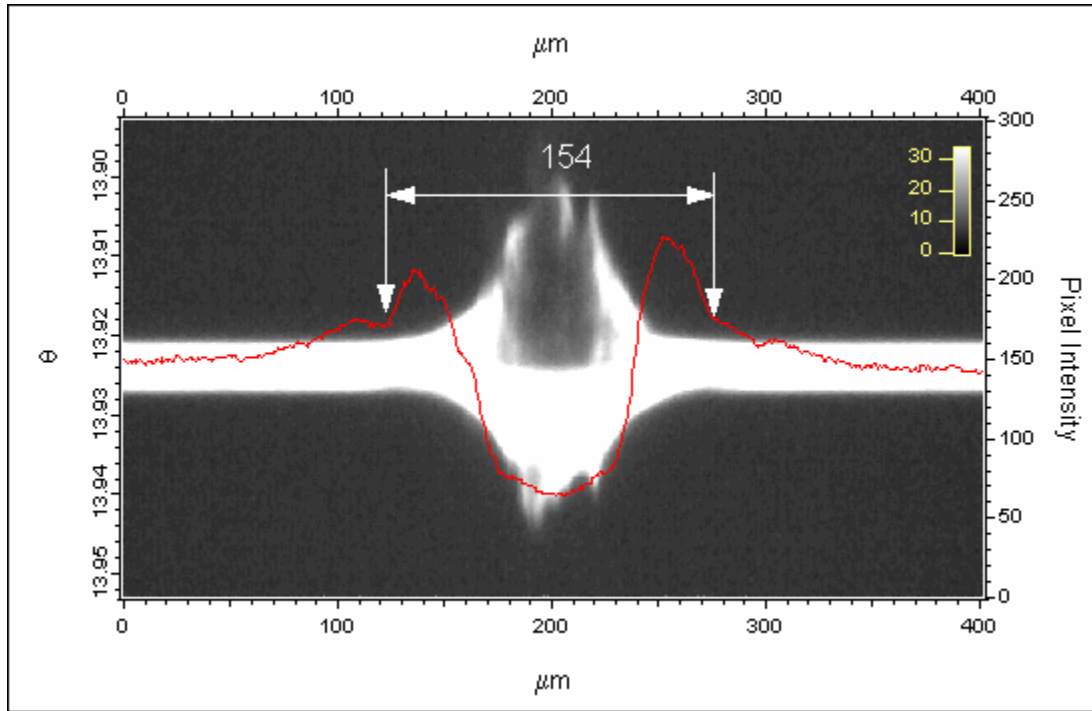
Figure 3.32. Xθ slice of high peak fluence fs laser spot $\overline{1}\overline{1}5$ showing region of horizontal damage. The Xθ slice is taken at a Y value of 143 μm of the XY slice.
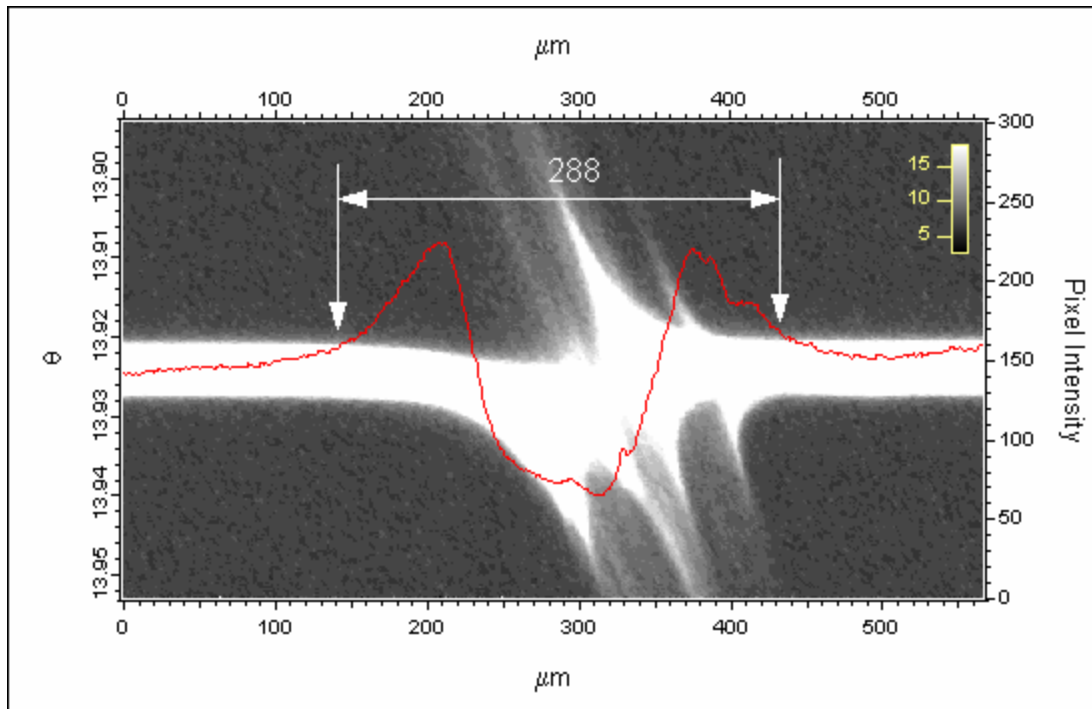
Figure 3.33. Yθ slice of high peak fluence fs laser spot $\overline{1}\overline{1}5$ showing region of vertical damage. The Yθ slice is taken at an X value of 100 μm on the XY slice.

Figure 3.34 shows an Xθ slice extracted approximately across the center of the feature at a Y coordinate of 143 μm of the XY slice. The lines A, B, C, D, E, F & G represent the rocking curves of a single pixel. A is the rocking curve of the undamaged crystal that is recorded at 10 μm on slice Xθ, far away from the extent of the damage in the horizontal direction. B & G are recorded at the peak value of intensity in the horizontal direction and C, D, E & F are rocking curves that show different behaviors. Figures 3.35, 3.36 and 3.37 show comparisons of the different rocking curves and Table 3.3 gives the data recorded from the seven rocking curves.
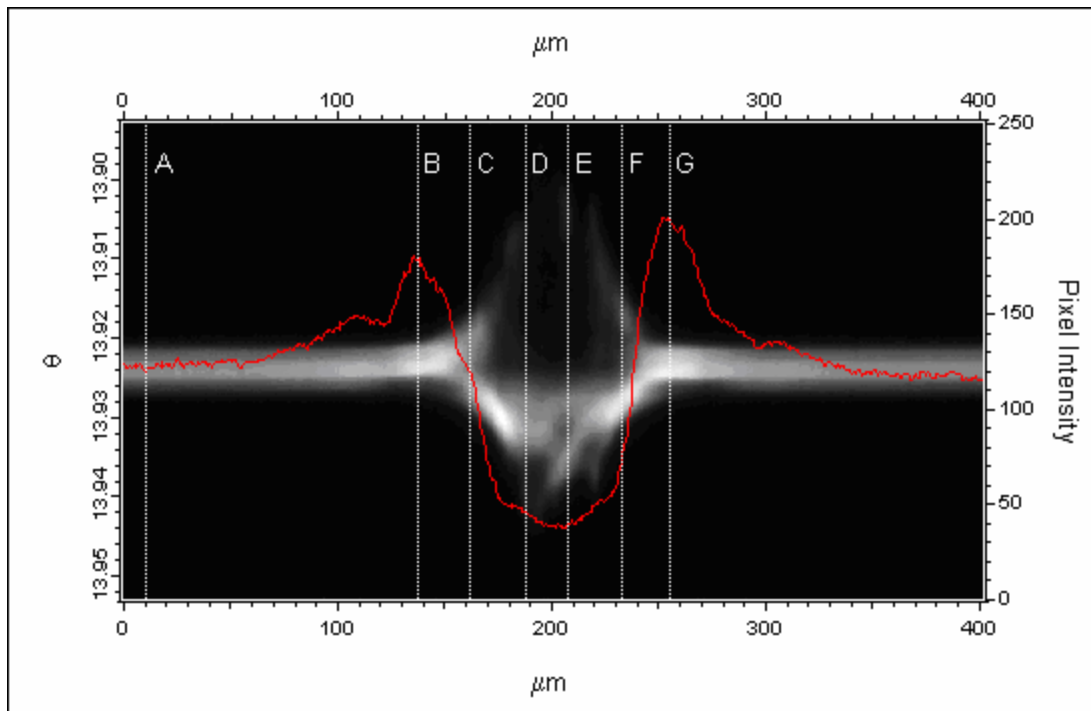
Figure 3.34. Xθ slice of high peak fluence fs laser spot 115 showing positions of rocking curves A, B, C, D, E, F & G. The Xθ slice is taken at a Y value of 143 μm of the XY slice.
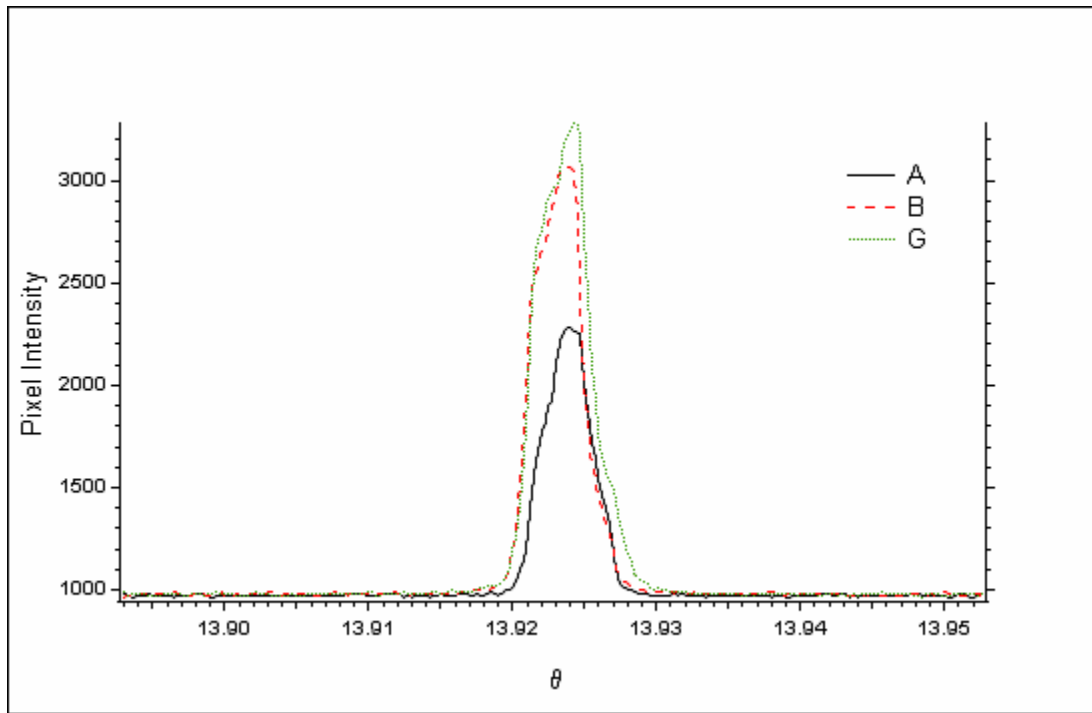
Figure 3.35. Comparison of rocking curves A, B & G of high peak fluence fs laser spot $\bar{1}\bar{1}5$.
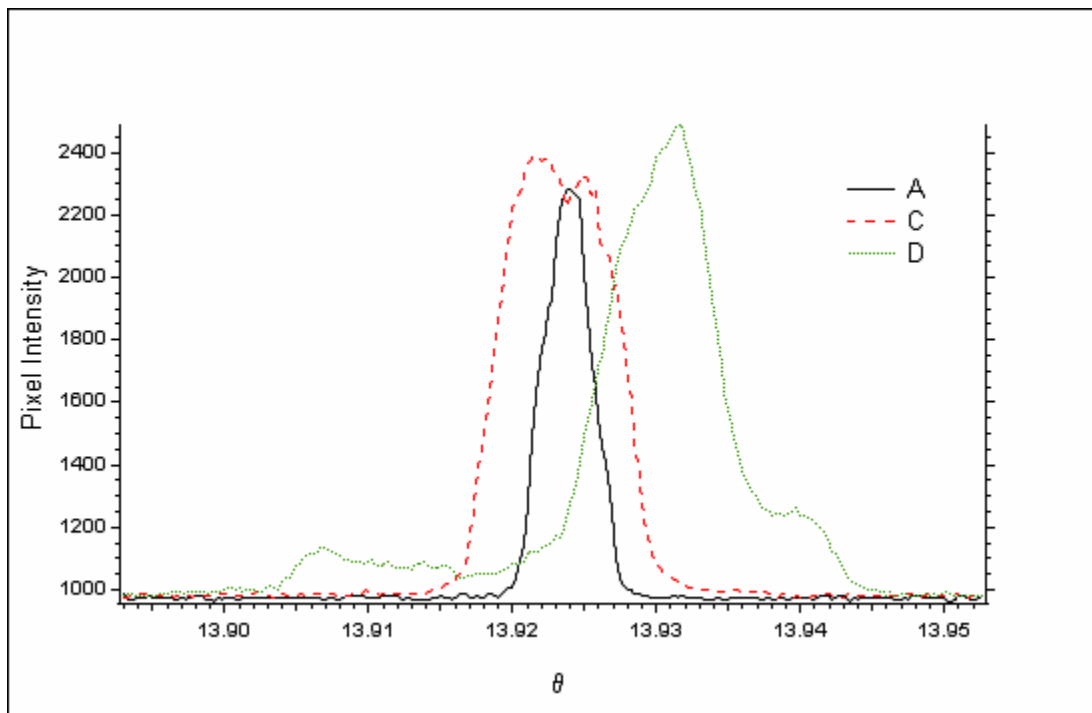
Figure 3.36. Comparison of rocking curves A, C & D of high peak fluence fs laser spot $\bar{1}\bar{1}5$.
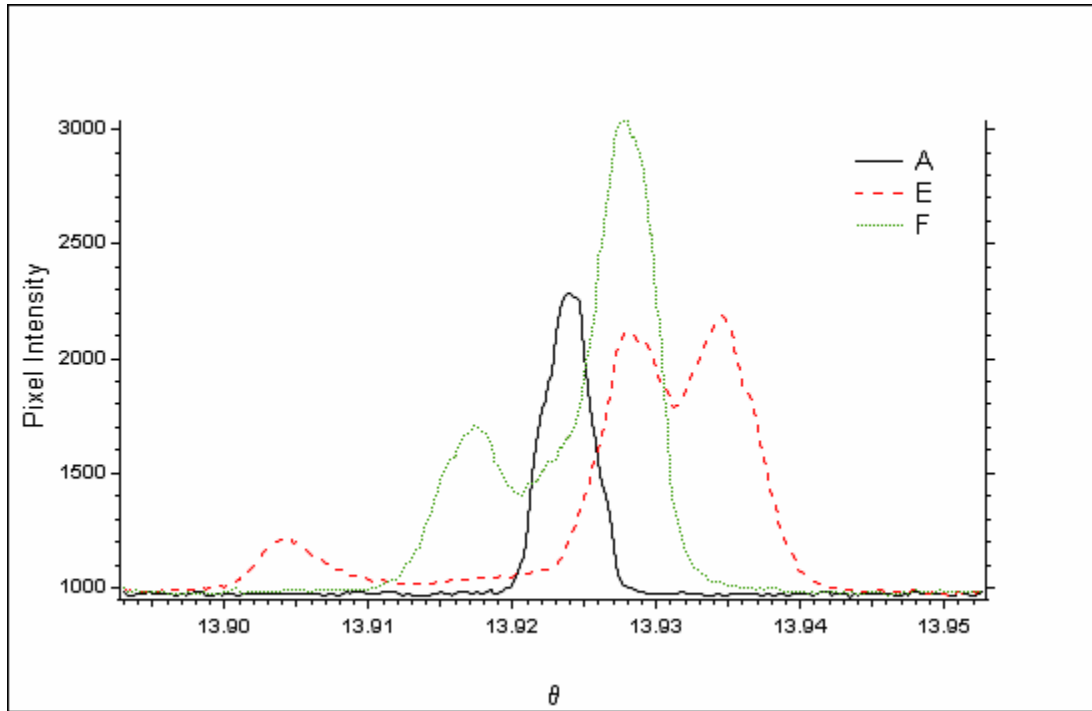
Figure 3.37. Comparison of rocking curves A, E & F of high peak fluence fs laser spot $\overline{1}\overline{1}5$.

Table 3.3. Rocking curve details of high peak fluence fs laser spot $\overline{1}\overline{1}5$.

Rocking Curve	Rocking Curve Position (μm)	Peak Intensity	Background Intensity	FWHM (arc sec)	FWHM (Curve) / FWHM (A)
A	10	2281	961	15.03	1.00
B	137	3063	953	14.76	0.98
C	162	2392	970	34.32	2.28
D	188	2488	969	30.14	2.04
E	208	2189	957	42.03	2.80
F	233	3036	970	18.66	1.24
G	255	3279	967	15.57	1.04

It can be seen in Table 3.3 and in Figure 3.35 the FWHM of the rocking curves, B and G, outside the crater are almost the same as that of the rocking curve, A, of the undamaged crystal and show very little variation. There is only a difference in the peak intensity of each of them which are supported from the linescans. Rocking curve C is at a

66

location where the curve starts to behave differently than curve B. It can be seen that rocking curve C has a notch at the peak and this notch becomes wider as it progresses through locations D, E and F. It is also seen that the FWHM of rocking curves of C, D, E and F are almost two times or more than the FWHM of the undamaged crystal. All the FWHM values obtained in Table 3.3, from this trial (Trial 2), vary with the FWHM values of the same spot obtained in Table 3.2 from Trial 1. The FWHM values in Trial 1 vary from 11-32 arc sec while the FWHM values in Trial 2 vary from 15-42 arc sec.

For a theoretically perfect Silicon crystal incident with 12 keV x-ray, the Darwin width for an 004 reflection (symmetric case) is 1.9776 arc sec with σ- polarization and 1.4050 arc sec with π- polarization. The Darwin width for a 115 reflection (asymmetric case) is 0.960 arc sec with σ- polarization and 0.4910 arc sec with π- polarization. Theoretically the 115 rocking curve width should be narrower than the 004 rocking curve width, but this changes with the asymmetry condition [Bowen et al., 1998]. Hence, the FWHM values of the rocking curves in Trial 2 show are broader as compared to the FWHM values of the rocking curves in Trial 1.

The characterization images in Figure 3.38 and 3.39 clearly show that the extent of the damage is well beyond the extent seen with a microscope. The images also show the nature and variation of the damage at different points in the feature. This helps in picking up certain points of interest for rocking curve and slice analysis. The maximum image shows the location where the different rocking curves were extracted to analyze the damage.

Comparing the high fluence fs laser spot observed with the two different Bragg peaks, we see some differences in details of these characterization images, but overall the

different images are quite similar in shape and extent of the damaged region. In particular, the Maximum Location images both show a sharp boundary between the areas diffracting with a peak at higher locations and a peak at lower locations.

3.3.3.2 Image Analysis on Rocking Curve Characterizations
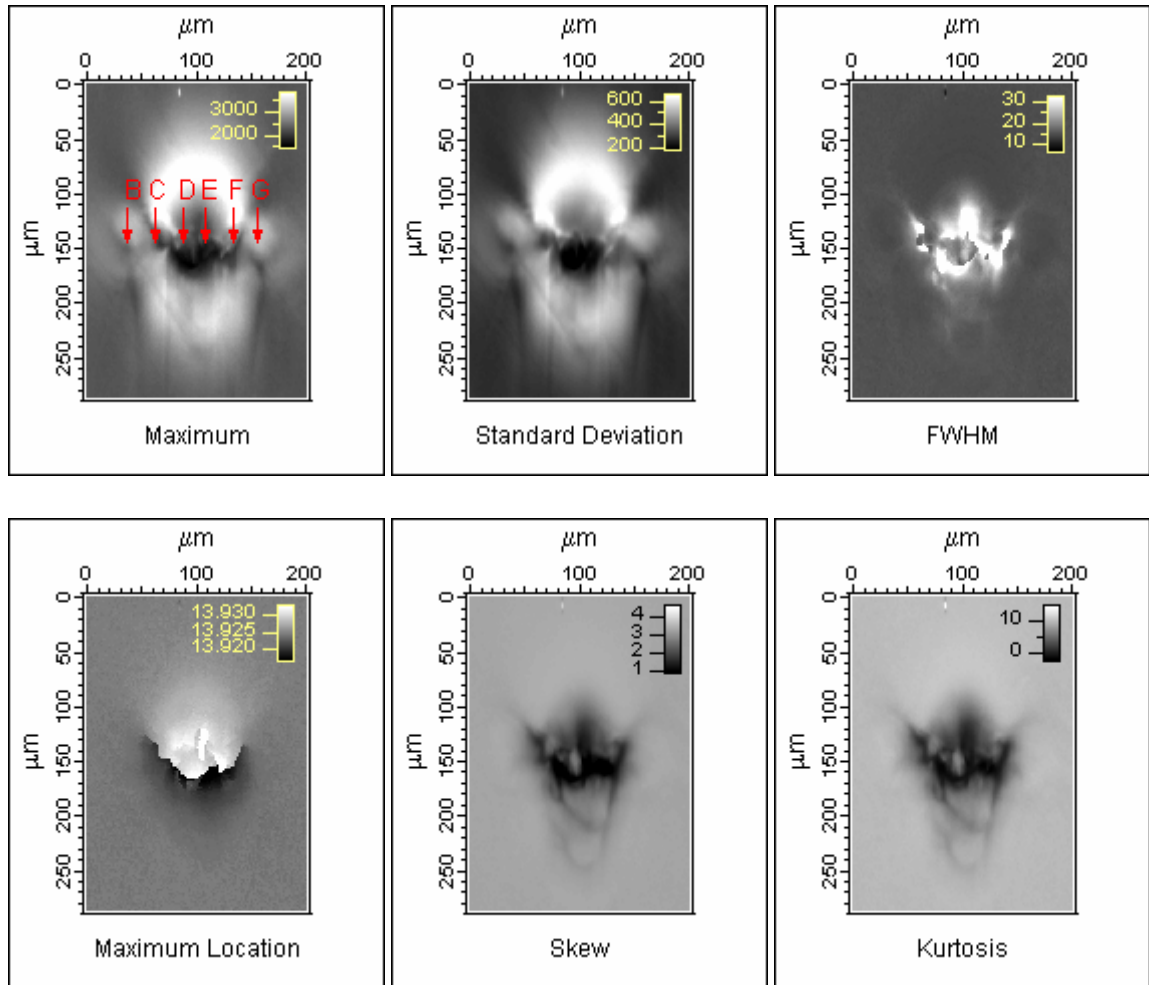
Figure 3.38. High peak fluence fs laser spot $\overline{1}1\overline{5}$ images showing characterizations Maximum, Standard Deviation, FWHM, Maximum Location, Skew & Kurtosis. The maximum image shows the location of the rocking curves, at the arrow head.
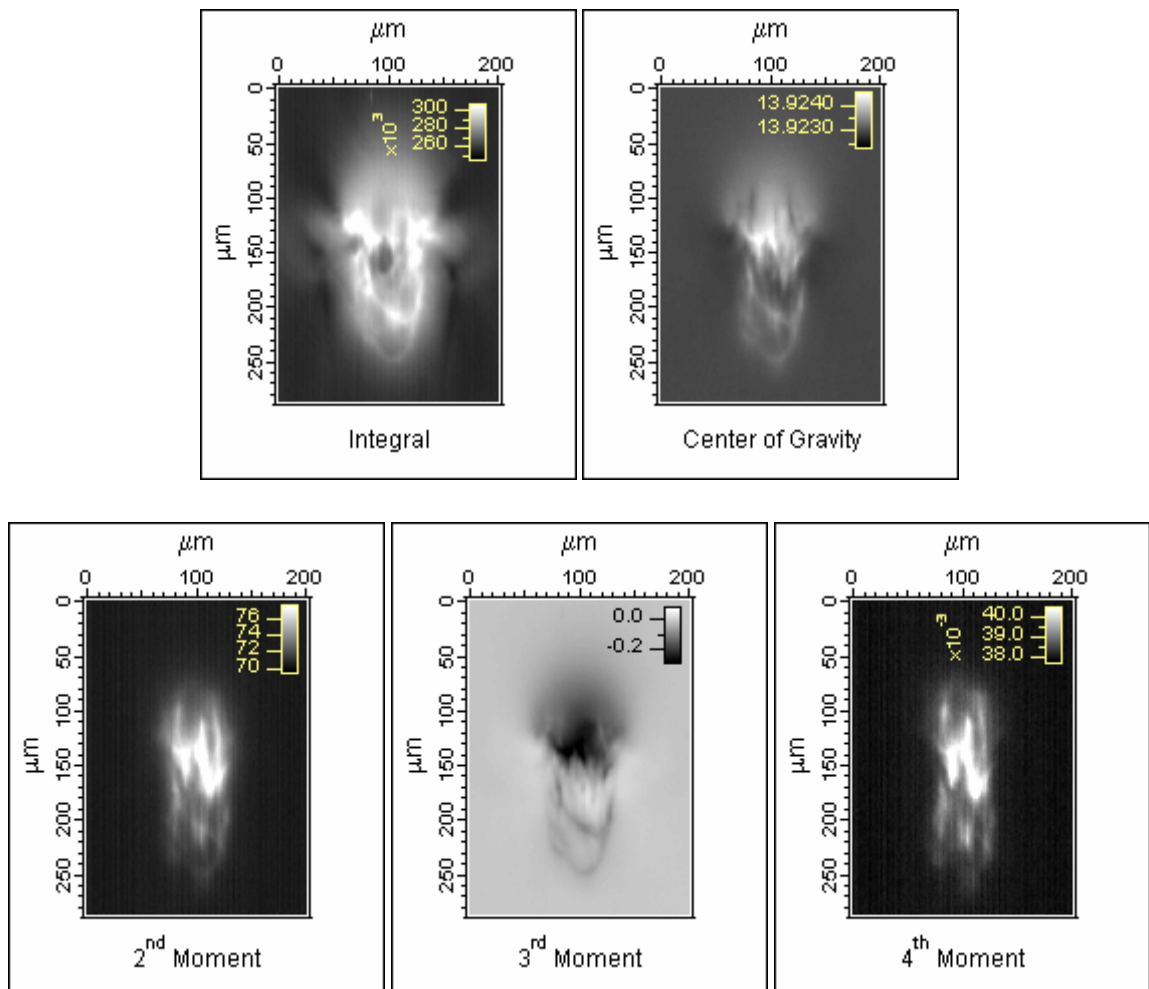
Figure 3.39. High peak fluence fs laser spot $\overline{1}\overline{1}5$ images showing moments Integral and Center of Gravity, 2nd, 3rd & 4th Moment about the Center of Gravity.

3.4   Low Peak Fluence Femtosecond Laser Spot, 0.63 J/cm^2

The following section will deal with micrographs and topographs of a femtosecond laser spot irradiated with a peak fluence of 0.63 J/cm^2. Two sets of experiments were conducted on this spot, one set in November 2003 and one set in April 2004.

3.4.1   Optical and Electron Microscopy

Figures 3.40 and 3.41 show optical and scanning electron micrographs (SEM) of the high fluence femtosecond laser spot irradiated with 100 pulses, peak fluence on the spot being 0.63 J/cm^2. Care was taken to orient the micrographs in the same orientation as the $0\,0\,4$ X-ray topographs so that a valid comparison can be made between the features being examined. The optical micrographs show horizontal and vertical size of the spot as 70 μm and 72 μm respectively. The SEM shows horizontal and vertical size of the spot as 74 μm and 76 μm respectively. The pixel readings on the edges of the feature and the resolution of the micrographs were used to determine the feature sizes. The SEM also shows a circle of 96 μm which is not visible in the optical micrograph. This circle could be condensed plasma. The SEM also shows a crater of about 50 μm in diameter. A horizontal and vertical linescan across the center of the micrographs reveals the contrast in more detail.

Figure 3.42 shows an enlarged view of region A from Figure 3.41. This enlarged region shows the presence of small holes or ablated region. Diffraction from these holes may be the origin of the circular ring that is seen in the topographs.

Figures 3.43 and 3.45 show horizontal and vertical linescans across the center of the irradiated spot on the micrograph. The linescan shows the extent of the laser damage. Figures 3.44 and 3.46 show horizontal and vertical linescans across the center of the irradiated spot on the SEM. The linescan shows the maximum width and height profiles of the damage.
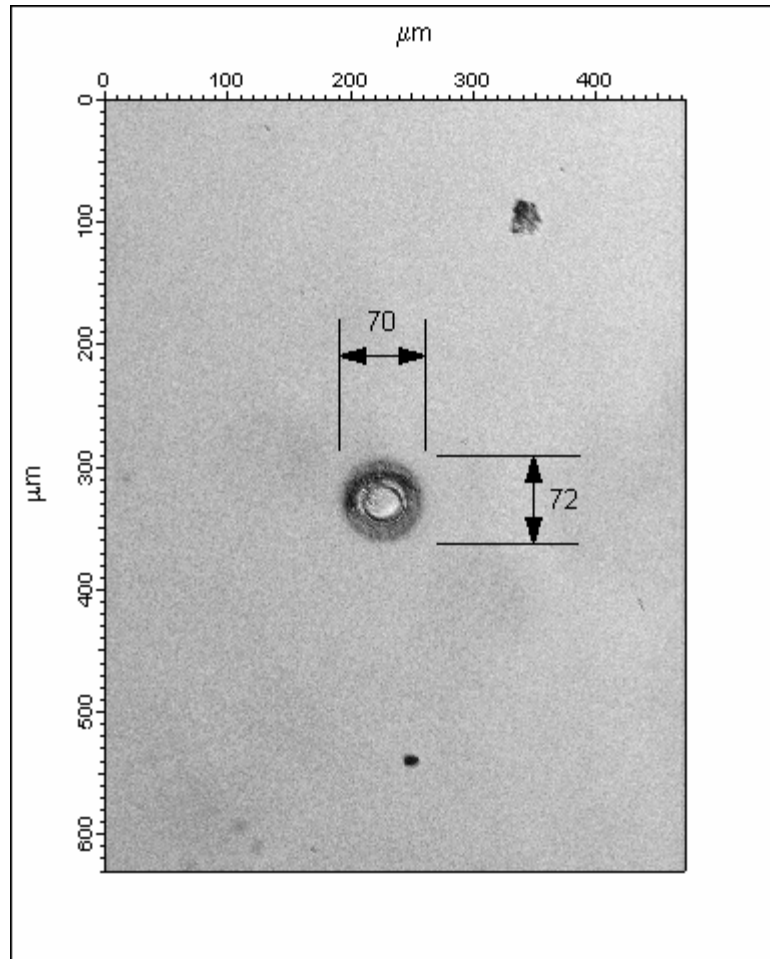
Figure 3.40. Optical micrograph showing feature size of low peak fluence (0.63 J/cm^2) femtosecond laser spot.
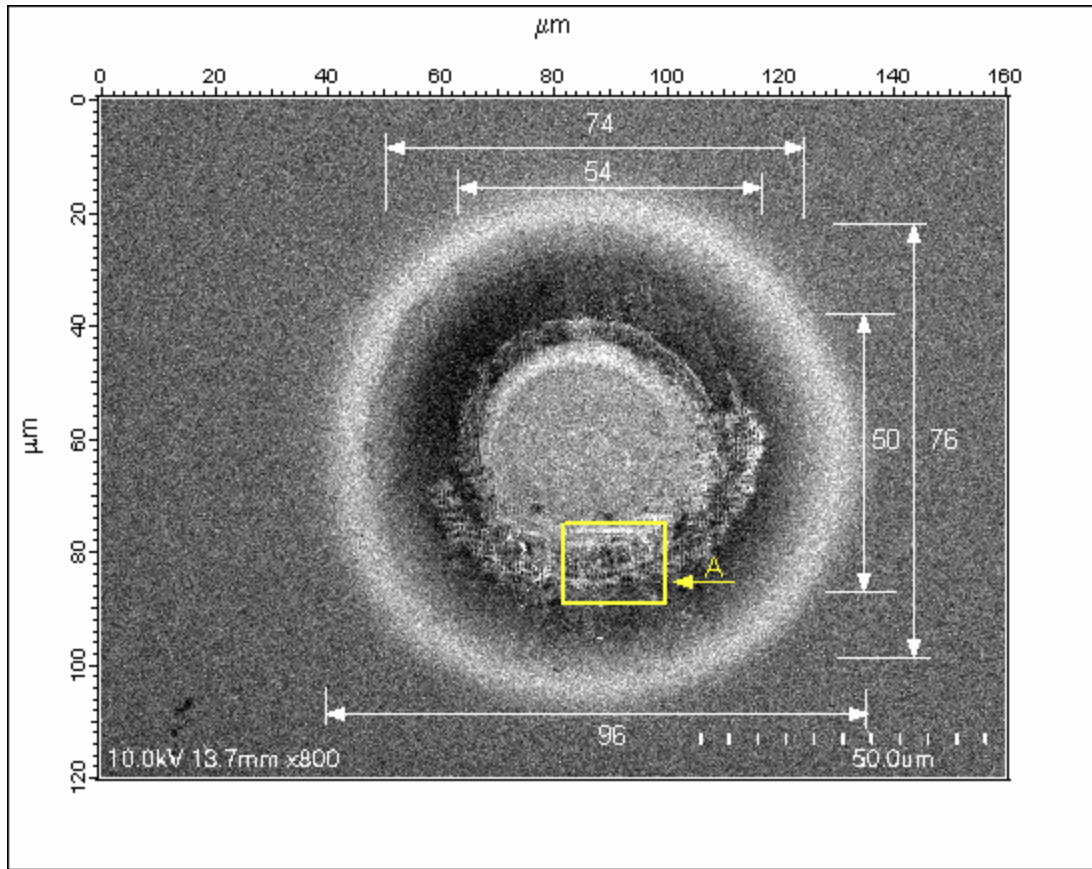
Figure 3.41. SEM showing feature size of low peak fluence (0.63 J/cm^2) femtosecond laser spot.
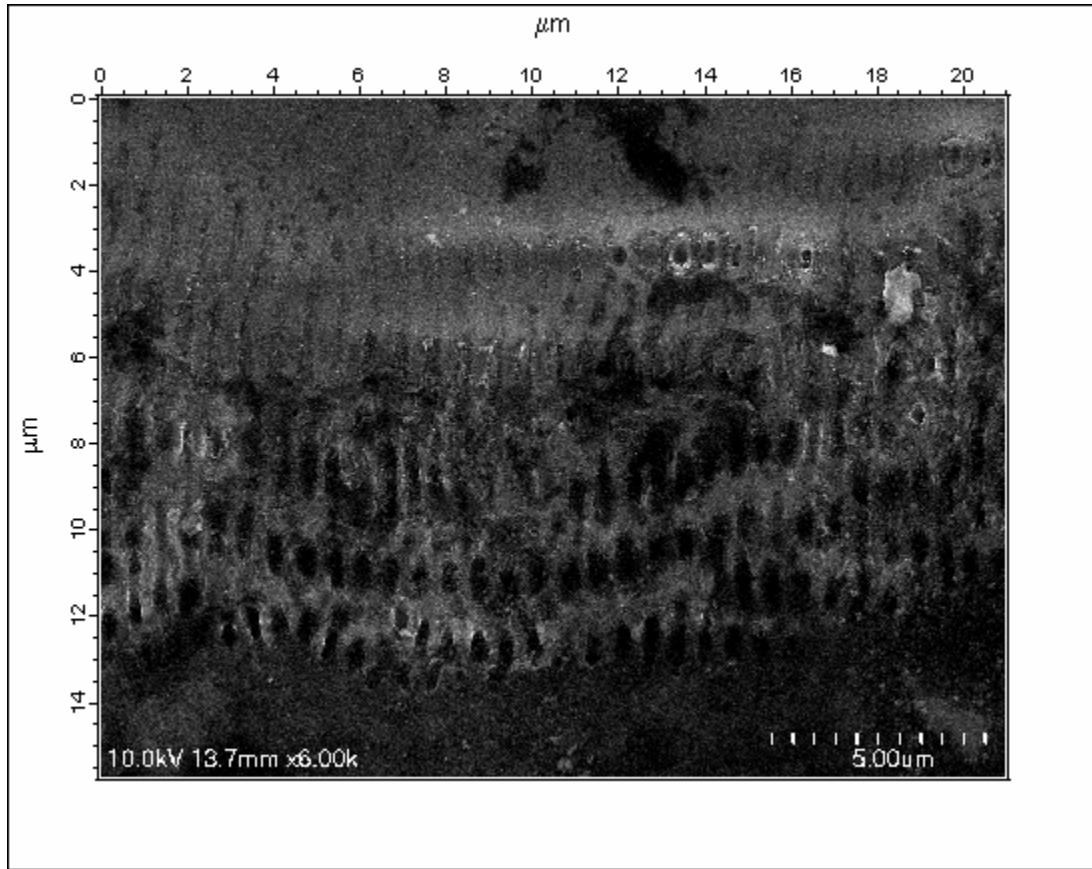
Figure 3.42. SEM showing enlarged region A, from Figure 3.41. The figure shows the presence of small hole like structures on the circumference of the ablated region.
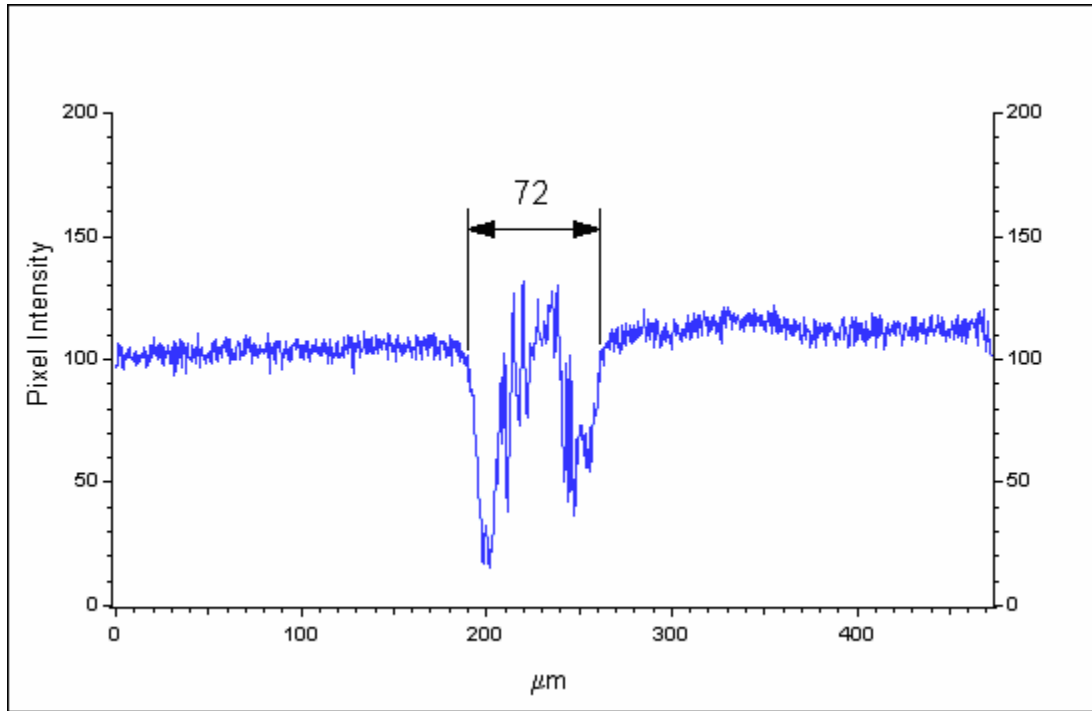
Figure 3.43. Horizontal linescan across micrograph of low peak fluence fs laser spot, showing feature size.
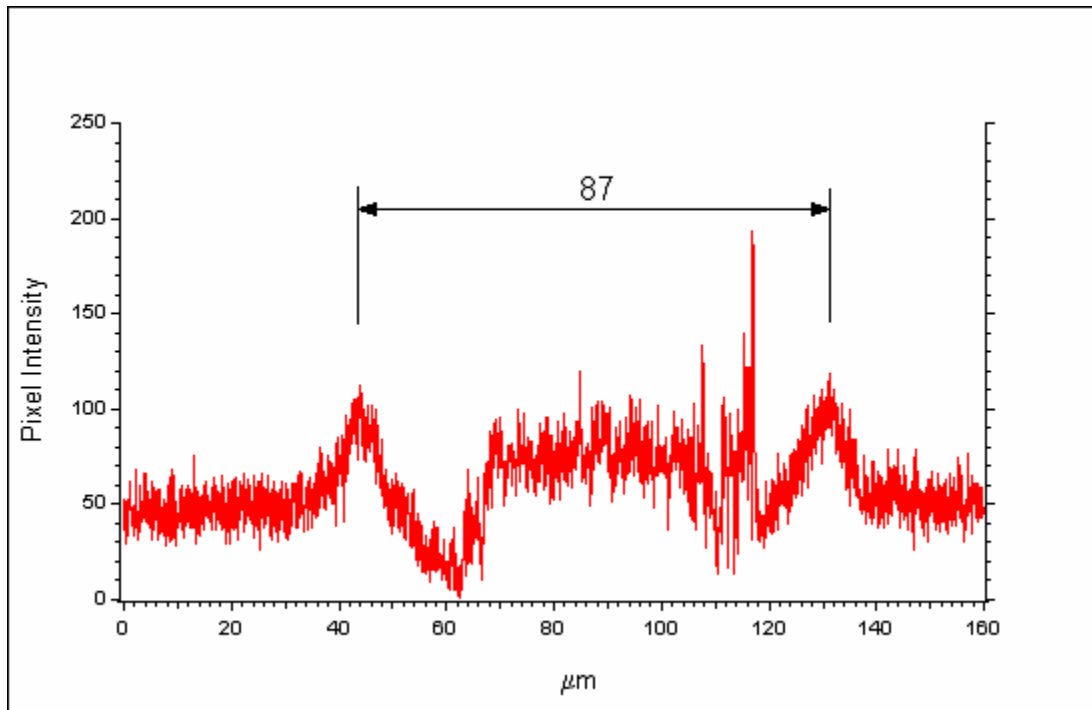
Figure 3.44. Horizontal linescan across SEM of low peak fluence fs laser spot, showing feature size.
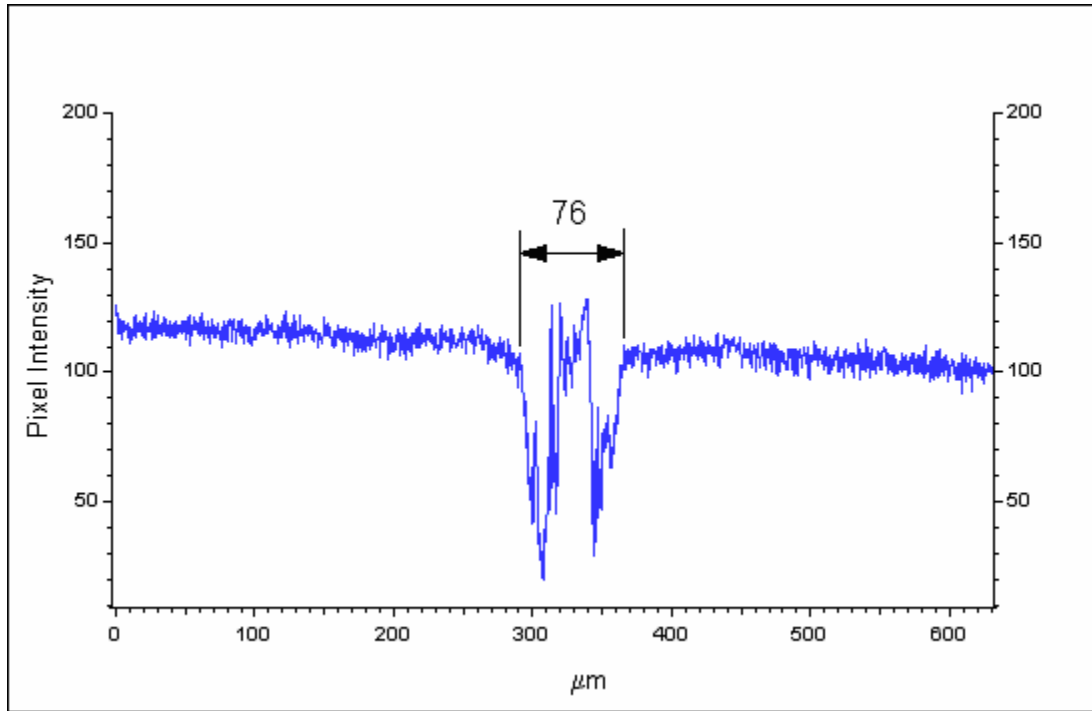
Figure 3.45. Vertical linescan across micrograph of high peak fluence fs laser spot, showing feature size.
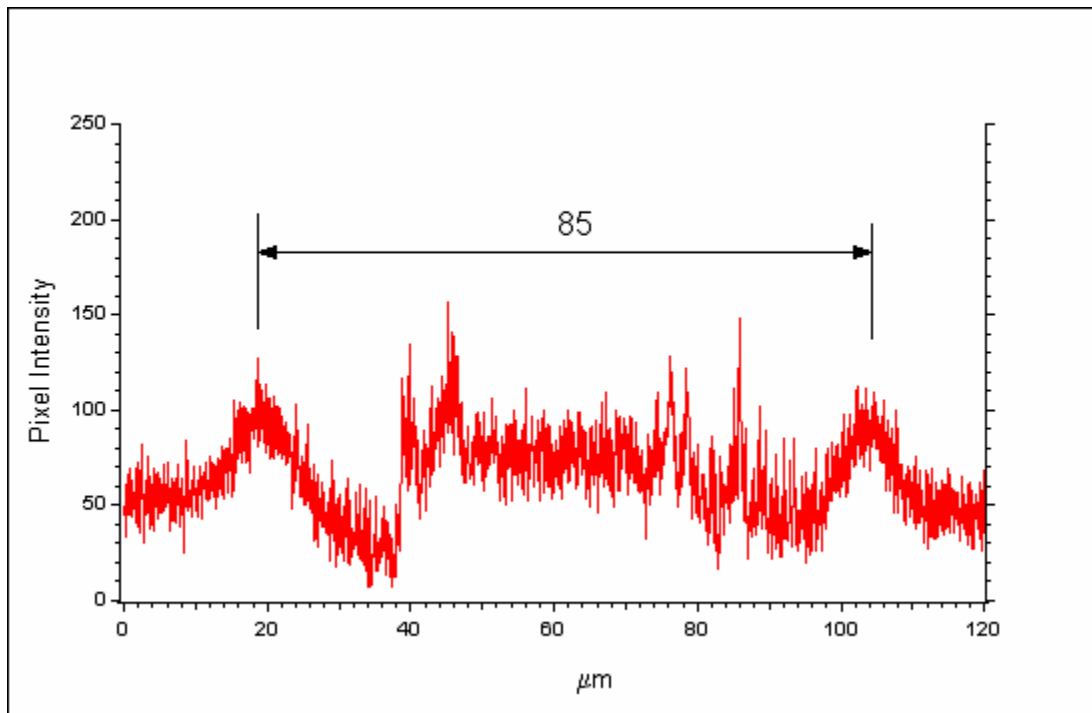
Figure 3.46. Vertical linescan across SEM of high peak fluence fs laser spot, showing feature size.

3.4.2   Topography – Trial 1 (April 2004) - 0 0 4

        The following section deals with the topographs of the femtosecond irradiated laser spot, with an h k l of 0 0 4 . The topographs presented in this section were obtained during experimentation in April 2004 at the APS. The topographs in this section can be used effectively to draw damage comparisons with the high power femtosecond topographs taken in April 2004 and November 2003.

3.4.2.1 Slice Analysis

        Figure 3.47 is an XY slice at the peak of the rocking curve. The XY slice is an image of the crystal diffracting at its Bragg peak, as seen by the CCD camera.

Figure 3.47. XY slice of low peak fluence fs laser spot 0 0 4 at the center of Bragg peak showing damage, as seen by the CCD camera (Trial 1).

Figure 3.48 is an image of the Xθ slice showing the diffracted intensity in the horizontal direction. The Xθ slice is extracted approximately across the center of the feature at a Y coordinate of 175 μm of the XY slice. The superimposed red line across the image is the image line profile that shows the change in intensity along the horizontal direction across the feature at a θ value of 22.4796˚. Contrast horizontally extends to 59 μm, which is about 11 μm less than the feature size as seen in the optical micrograph and 15μm less than the feature size as seen in the SEM.

Figure 3.49 is an image of the Yθ slice with adjusted intensity range showing the extent of contrast in the vertical direction. The Yθ slice is extracted at X coordinate of 100 μm of the XY slice. The contrast in the vertical direction across the feature measures 58 μm, which is about 14 μm less than the feature size as seen in the optical micrograph and SEM.

A major point to be noted here is that the extent of damage horizontal in the topographs above is confined to the extent of the damage seen in the microscope images and does not show any extended damage as the high fluence spots does. The horizontal linescans across the Xθ slice show a sharp fall in the intensity at the edges of the feature. In contrast, the line horizontal linescans across the high power femtosecond laser spots showed a gradual decrease in intensity around them that gradually extended out horizontally to about 2.8 times more than what the optical damage showed. Note how the diameter of the holes like structures seen in Figure 3.2 matches the diameter of the ring in the topographs and the outer white rim doesn't. This structure may be the source of the diffracted intensity and the contrast in the images. A dynamical diffraction model of the structure is needed.

Figure 3.48. Xθ slice of low peak fluence fs laser spot 0 0 4 showing region of horizontal damage (Trial 1). The Xθ slice is taken at a Y value of 175 μm of the XY slice.

Figure 3.49. Yθ slice of low peak fluence fs laser spot 0 0 4 showing region of vertical damage (Trial 1). The Yθ slice is taken at an X value of 100 μm on the XY slice.

Figure 3.50 shows an Xθ slice extracted approximately across the center of the feature at a Y coordinate of 175 μm of the XY slice. The lines A, B, C & D are rocking curves of a single pixel in the vertical direction of the Xθ slice. A is the rocking curve of the undamaged crystal that is recorded at 10 μm on slice Xθ, far away from the damaged region in the horizontal direction. B & D are recorded at the peak value of strain in the horizontal direction and C is recorded at the center of the feature. Figure 3.51 shows the comparisons of the four different rocking curves and Table 3.4 gives the data recorded from the four rocking curves.

Figure 3.50. Xθ slice of low peak fluence fs laser spot 0 0 4 showing positions of rocking curves A, B, C & D (Trial 1). The Xθ slice is taken at a Y value of 175 μm of the XY slice.

Figure 3.51.Comparisons of rocking curve A, B, C & D of low peak fluence fs laser spot 0 0 4 (Trial 1).

Table 3.4. Rocking curve details of low peak fluence fs laser spot 0 0 4 (Trial 1).

Rocking Curve	Rocking Curve Position (μm)	Peak Intensity	Background Intensity	FWHM (arc sec)	FWHM (Curve) FWHM (A)
A	10	1133	74	11.58	1.00
B	177	1525	74	12.30	1.06
C	202	1222	83	11.63	1.00
D	227	1260	80	12.04	1.03

It can be seen in Table 3.4 and in Figure 3.51, the FWHM of all the rocking curves B, C & D are almost the same as that of the rocking curve, A, of the undamaged crystal. There is only a difference in the peak intensity of each of them which are supported from the linescans. Note the maximum difference in the peak intensity of the curve is 36 %. Hence, the rocking curves show that the laser damage to the spot is minimal and does not show the presence of any strain field beyond the visible feature.

The characterization images, Figures 3.53 and 3.54, also show very little damage as compared to the characterization images of the high fluence femtosecond laser spot.

3.4.2.2 Image Analysis on Rocking Curve Characterizations

Figure 3.52. Low peak fluence fs laser spot 004 images showing characterizations Maximum, Standard Deviation, FWHM, Maximum Location, Skew & Kurtosis. The maximum image shows the location of the rocking curves, at the arrow head (Trial 1).

Figure 3.53. Low peak fluence fs laser spot 0 0 4 images showing moments Integral and Center of Gravity, 2nd, 3rd & 4th Moment about the Center of Gravity (Trial 1).

3.4.3 Topography – Trial 2 (November 2003) - 0 0 4

The following section deals with the topographs of the femtosecond irradiated laser spot, with an h k l of 0 0 4. The topographs presented in this section were obtained during experimentation in November 2003 at the APS. The topographs in this section can be used to draw comparisons with the topographs taken in April 2004.

3.4.3.1 Slice Analysis

Figure 3.54 is an XY slice at the peak of the rocking curve. The XY slice is an image of the crystal diffracting at its Bragg peak, as seen by the CCD camera.
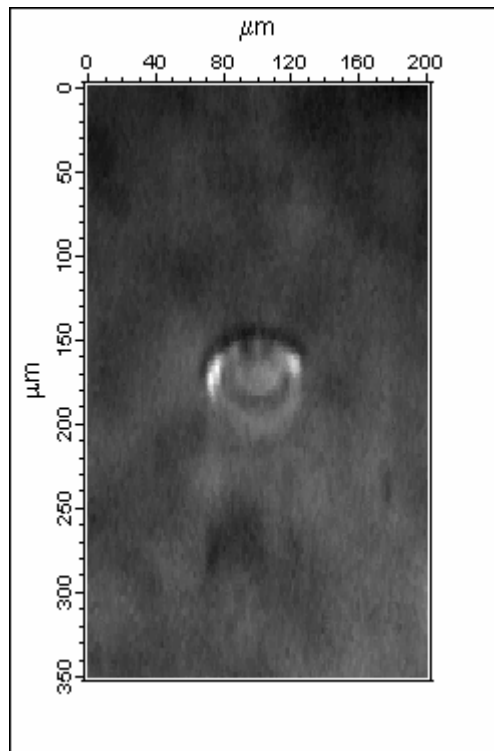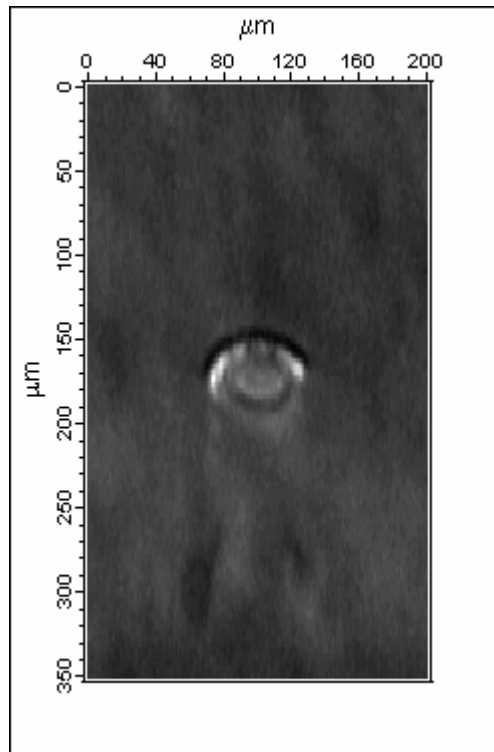

Figure 3.54. XY slice of low peak fluence fs laser spot 0 0 4 at the center of Bragg peak showing damage, as seen by the CCD camera (Trial 2).

Figure 3.55 is an image of the Xθ slice showing the diffracted intensity in the horizontal direction. The Xθ slice is extracted approximately across the center of the feature at a Y coordinate of 175 μm of the XY slice. The superimposed red line across the image is the image line profile that shows the change in intensity along the horizontal direction across the feature at a θ value of 22.445˚. The contrast horizontally extends to 61 μm, which is very consistent with the horizontal feature size as seen in the topograph from Trial 1 (59 μm).

Figure 3.56 is an image of the Yθ slice with showing the extent of contrast in the vertical direction. The Yθ slice is extracted at X coordinate of 100 μm of the XY slice. The contrast in the vertical direction across the feature measures 55 μm, which once again is very consistent with the vertical feature size as seen in the topograph from Trial 1 (58 μm).

The topographs shown in Figures 3.55 and 3.56 supports the conclusion there is very little damage produce with the lower spread of horizontal damage in low peak fluence femtosecond laser. The horizontal linescans across the Xθ slice in both the trials show a sharp fall in the intensity at the edges of the feature.

The consistency obtained with this method is also remarkable. Trial 1 and Trial 2 were conducted on the same laser spot and same crystal plane $0\,0\,\bar{4}$ with a span of six months in between them, but both the trials give very nearly the same results, showing the results are reproducible.
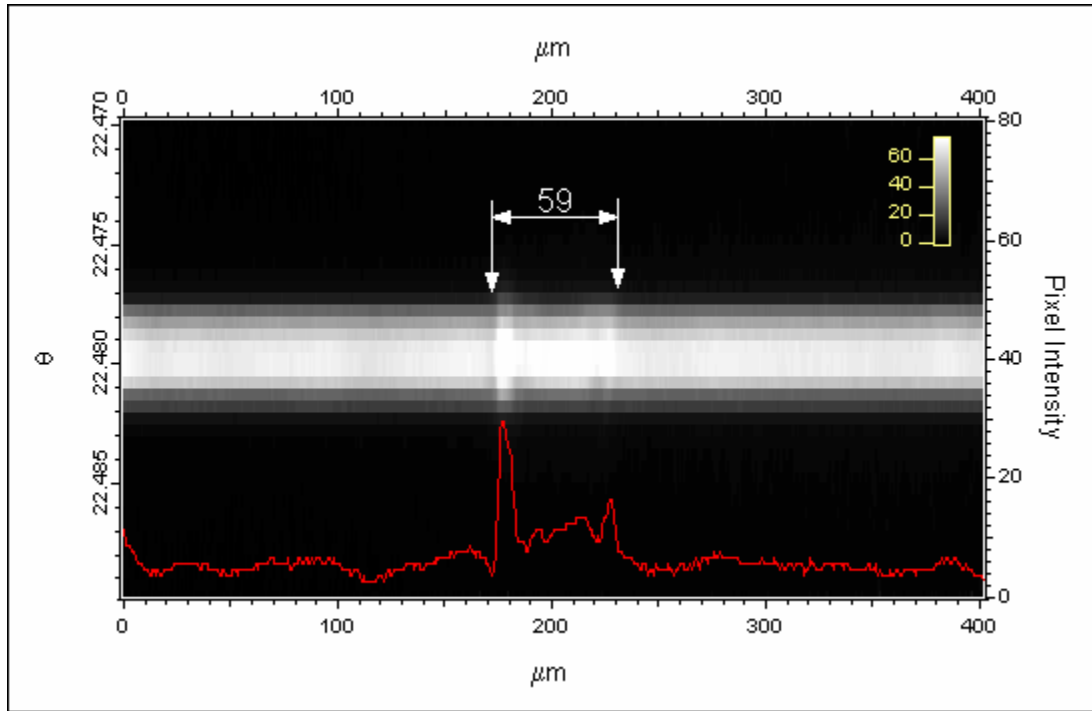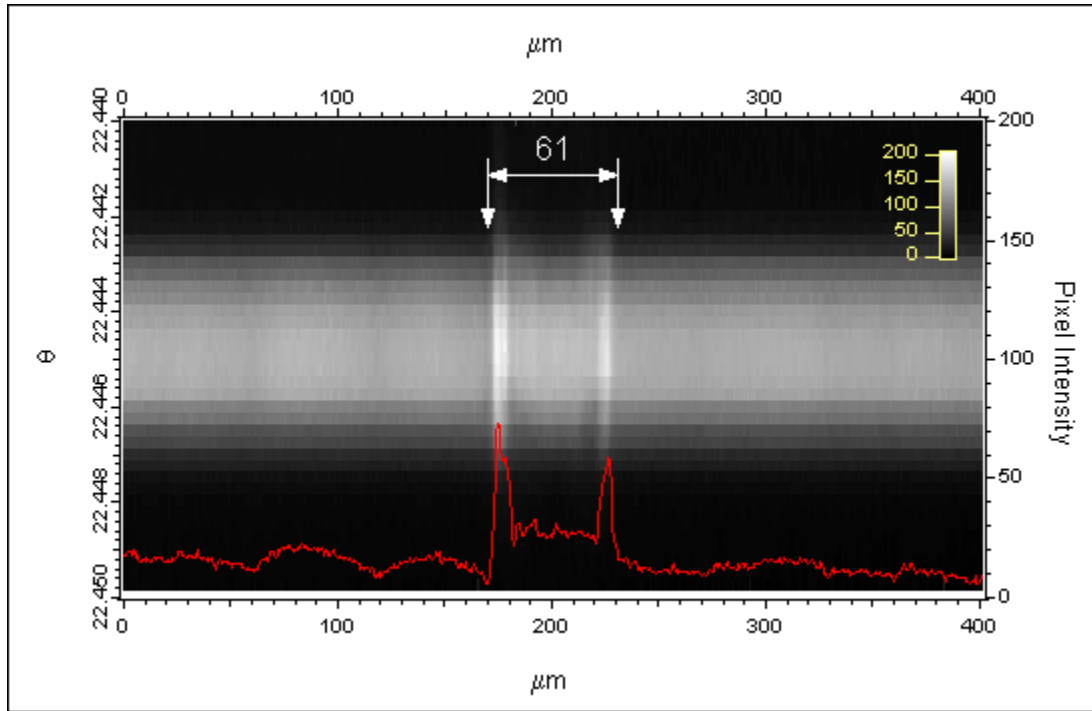
Figure 3.55. Xθ slice of low peak fluence fs laser spot 0 0 4 showing region of horizontal damage (Trial 2). The Xθ slice is taken at a Y value of 175 μm of the XY slice.
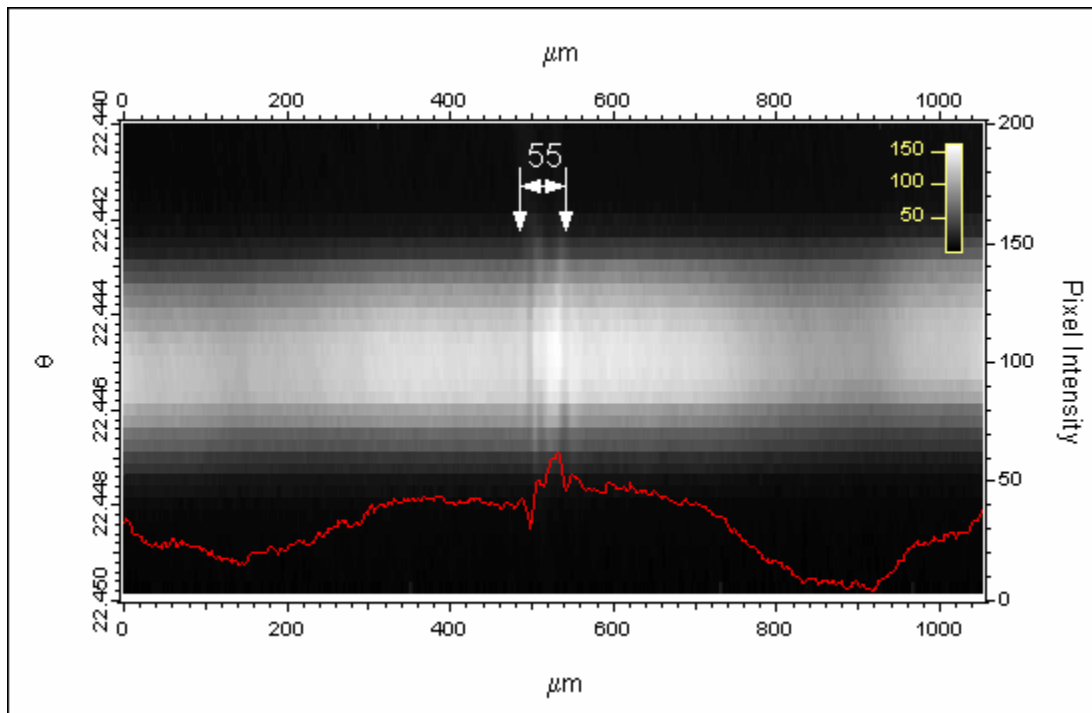
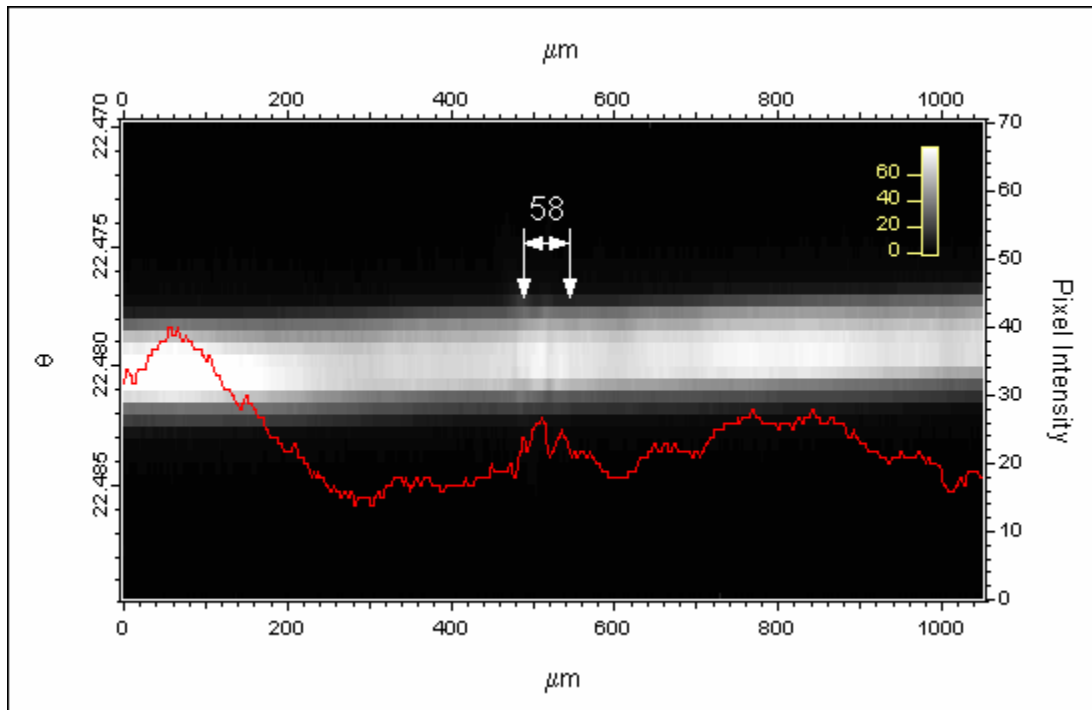Figure 3.56. Yθ slice of low peak fluence fs laser spot 0 0 4 showing region of vertical damage (Trial 2). The Yθ slice is taken at an X value of 100 μm on the XY slice.

Figure 3.57 shows an Xθ slice extracted approximately across the center of the feature at a Y coordinate of 175 μm of the XY slice. The lines A, B, C & D are rocking curves of a single pixel in the vertical direction of the Xθ slice. A is the rocking curve of the undamaged crystal that is recorded at 10 μm on slice Xθ, far away from the damaged region in the horizontal direction. B & D are recorded at the peak value of strain in the horizontal direction and C is recorded at the center of the feature. Figure 3.57 shows the comparisons of the four different rocking curves and Table 3.5 gives the data recorded from the four rocking curves.
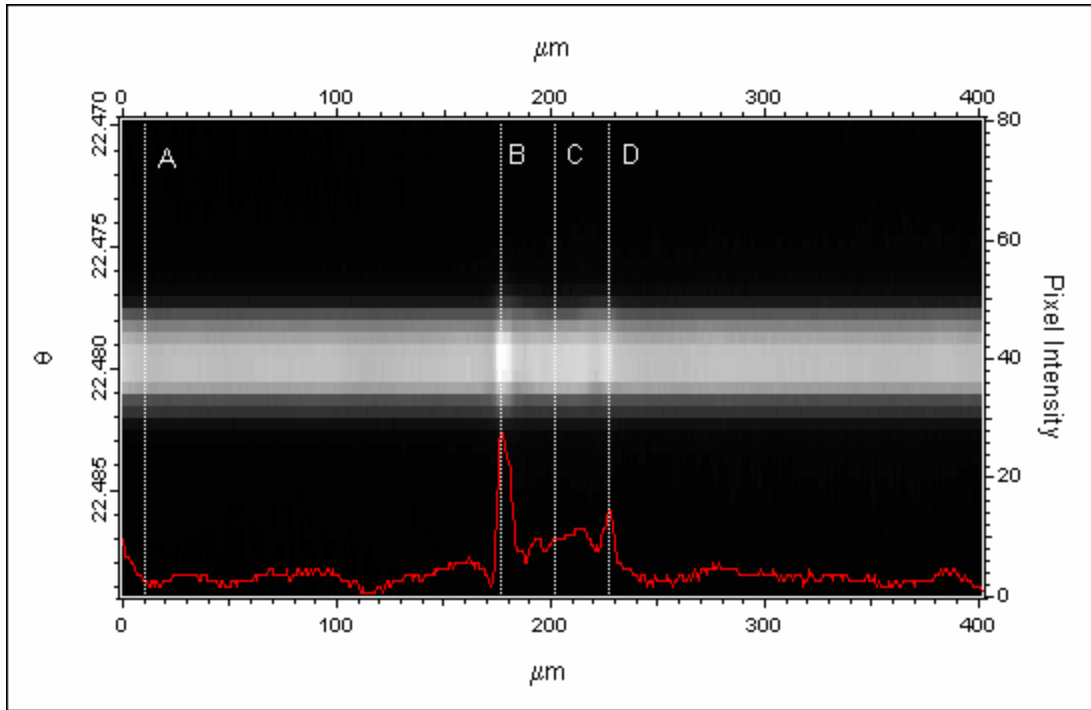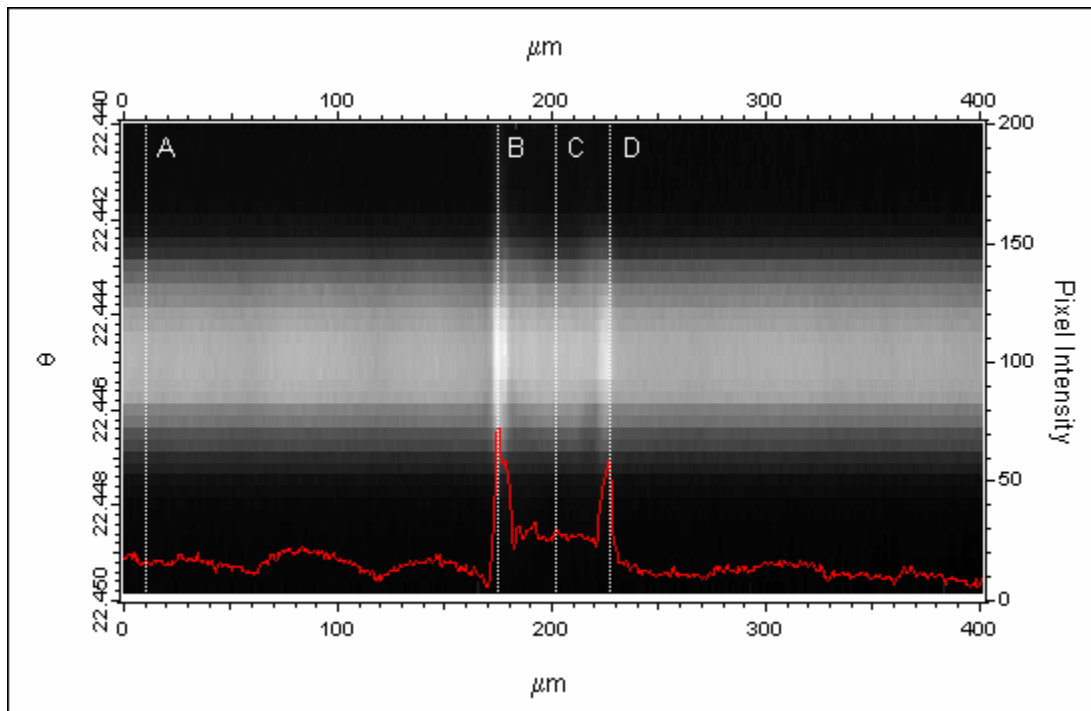

Figure 3.57. Xθ slice of low peak fluence fs laser spot 0 0 4 showing positions of rocking curves A, B, C & D (Trial 2). The Xθ slice is taken at a Y value of 175 μm of the XY slice.
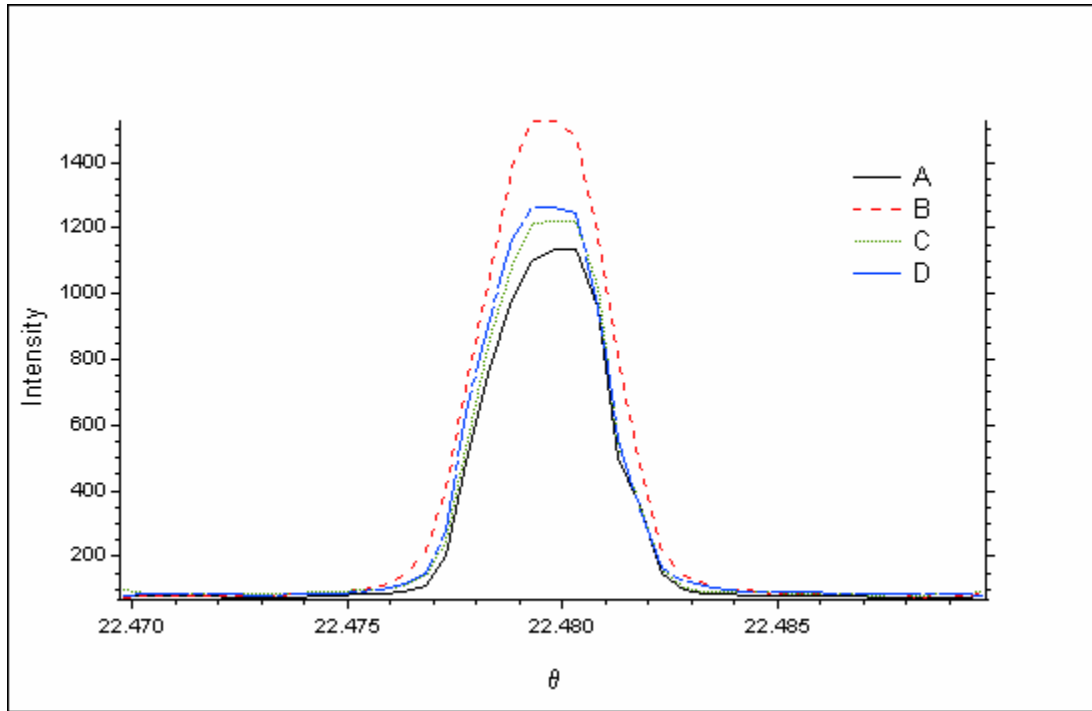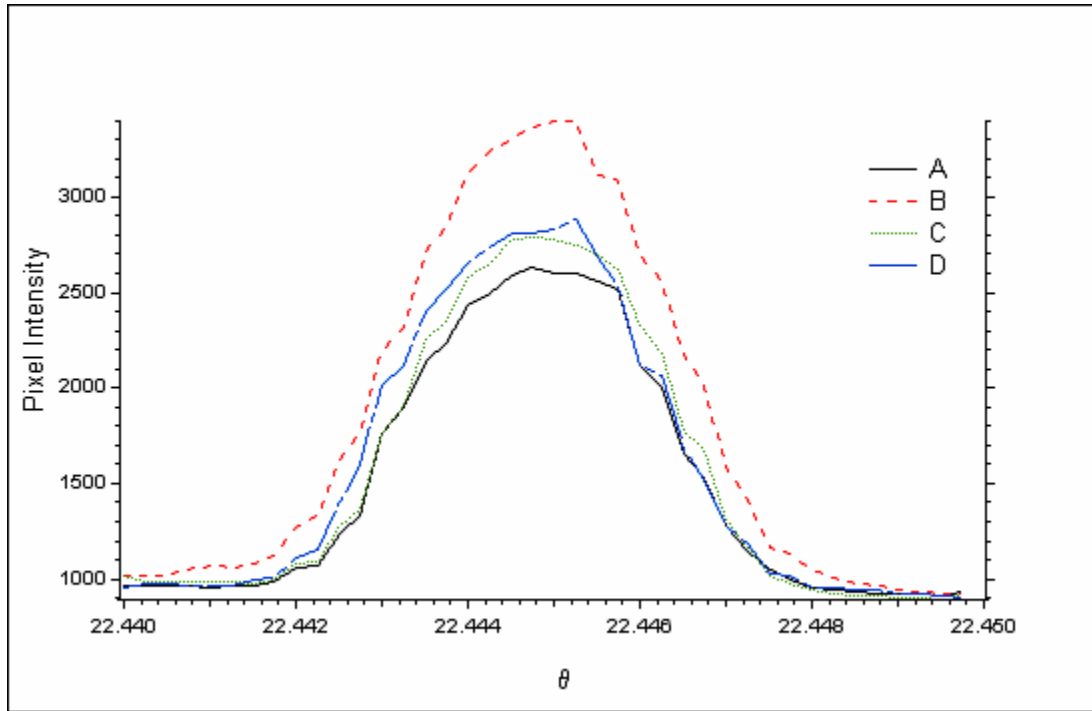
Figure 3.58.Comparisons of rocking curve A, B, C & D of low peak fluence fs laser spot 0 0 4 (Trial 2).

Table 3.5. Rocking curve details of low peak fluence fs laser spot 0 0 4 (Trial 2).

Rocking Curve	Rocking Curve Position (μm)	Peak Intensity	Background Intensity	FWHM (arc sec)	FWHM (Curve) FWHM (A)
A	10	2636	910	12.23	1.00
B	175	3396	920	12.74	1.04
C	202	2783	904	11.95	0.98
D	227	2882	902	12.36	1.01

It can be seen in Table 3.5 and in Figure 3.58 the FWHM of all the rocking curves B, C & D are almost the same as that of the rocking curve, A, of the undamaged crystal. The FWHM of the four curves in this trial also show remarkable consistency with the FWHM of the curves in Trial 1. They all show only a difference in the peak intensity, with a maximum variation of 29 %. The characterization images in Figure 3.59 and 3.60 also show very little visible contrast, just as they showed in Trial 1.

3.4.3.2 Image Analysis on Rocking Curve Characterizations
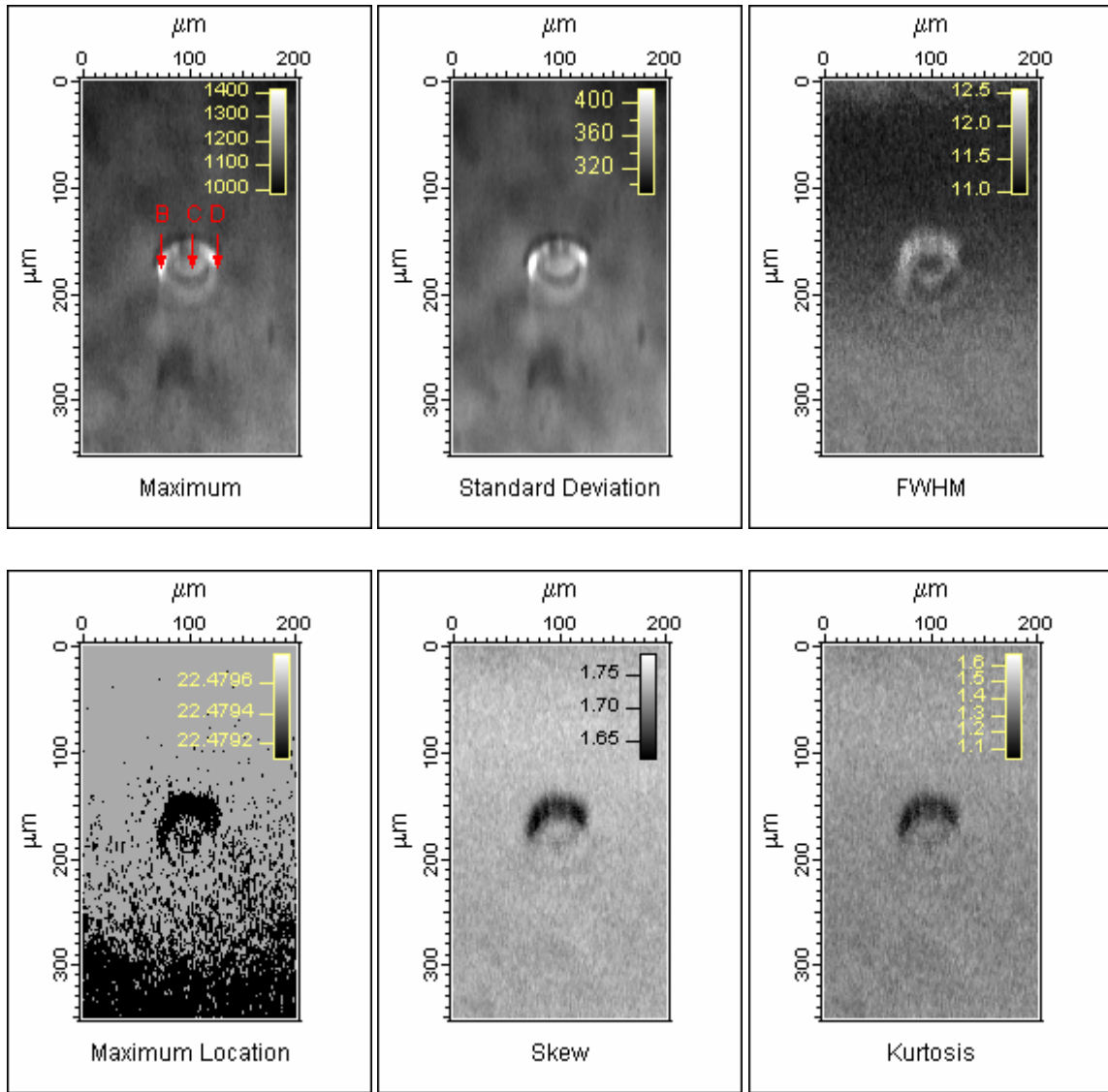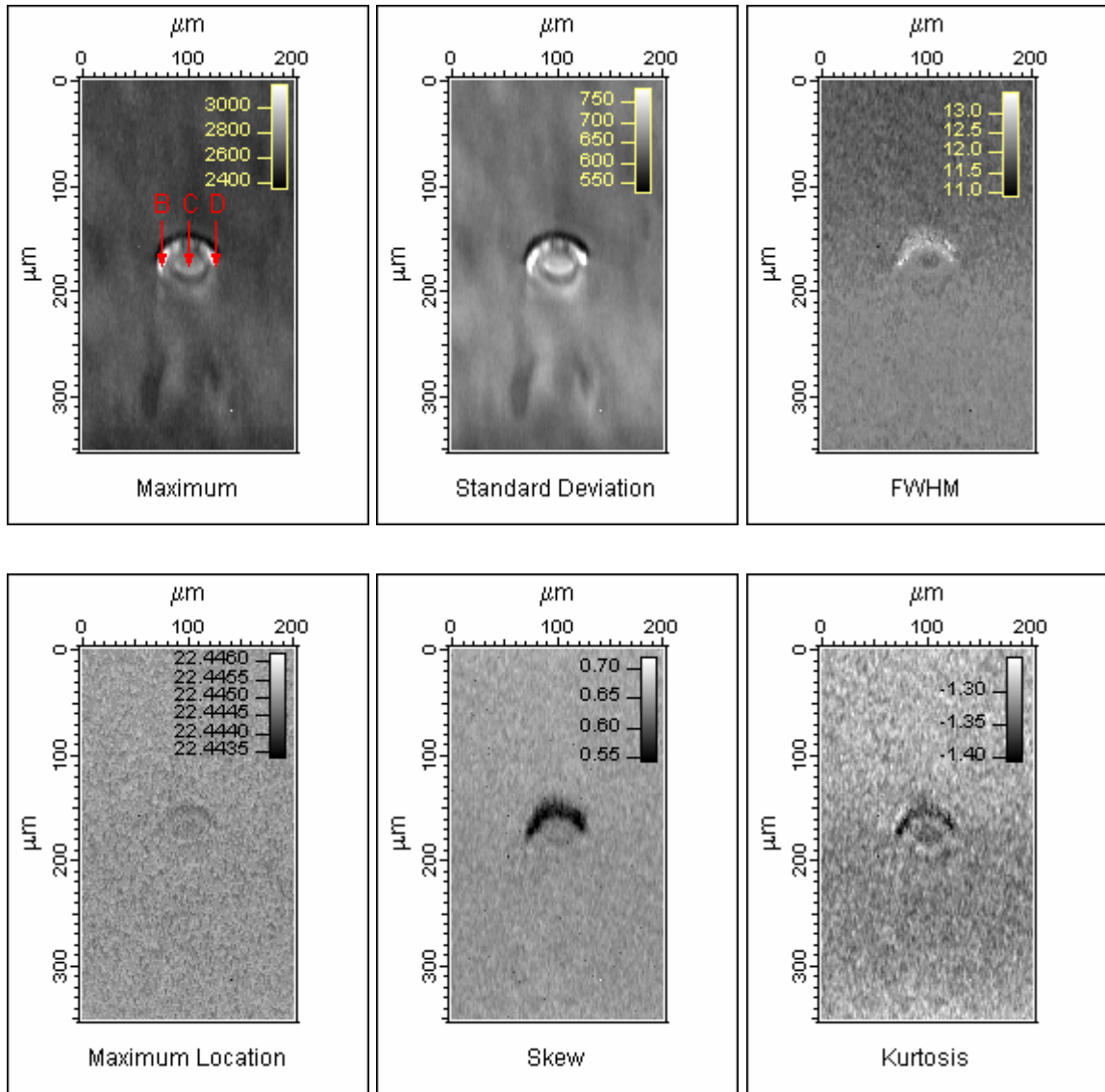

Figure 3.59. Low peak fluence fs laser spot $(0\,0\,4)$ images showing characterizations Maximum, Standard Deviation, FWHM, Maximum Location, Skew & Kurtosis. The maximum image shows the location of the rocking curves, at the arrow head (Trial 2).
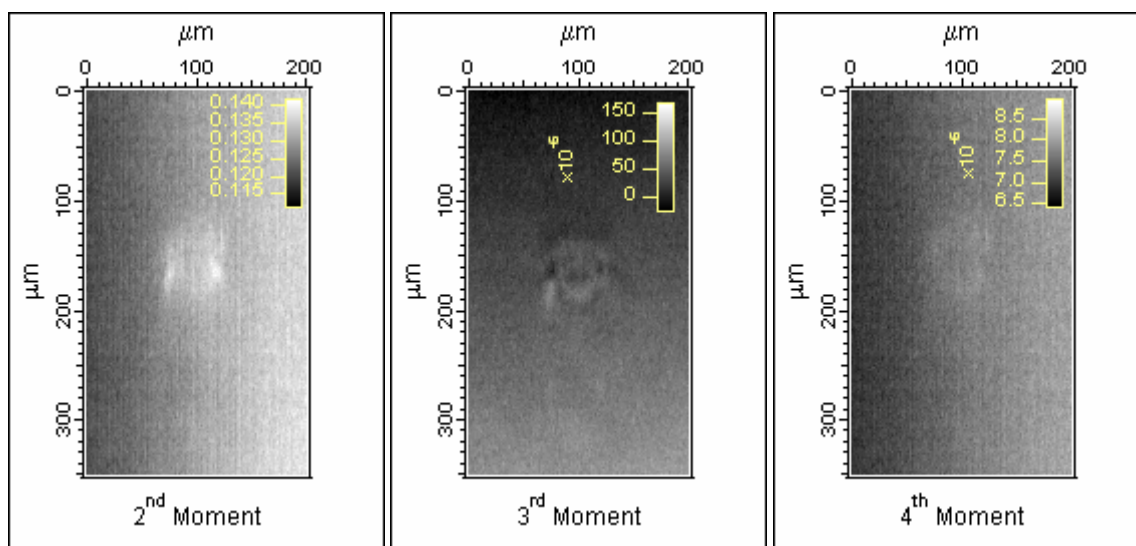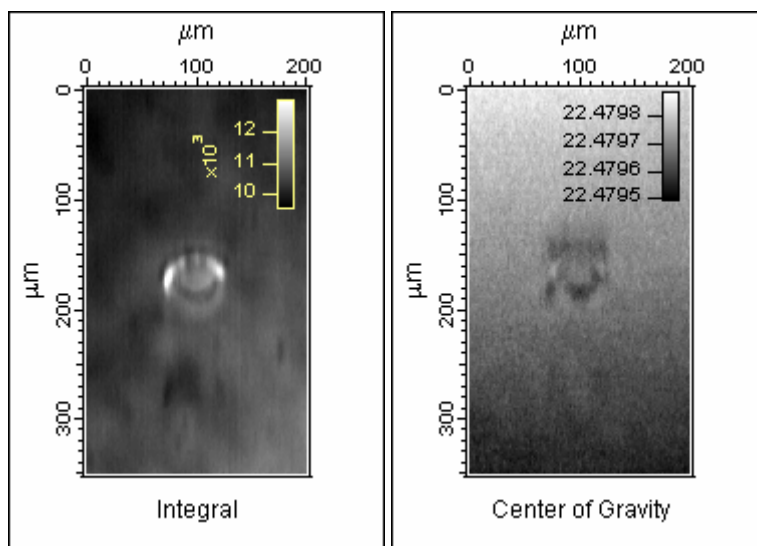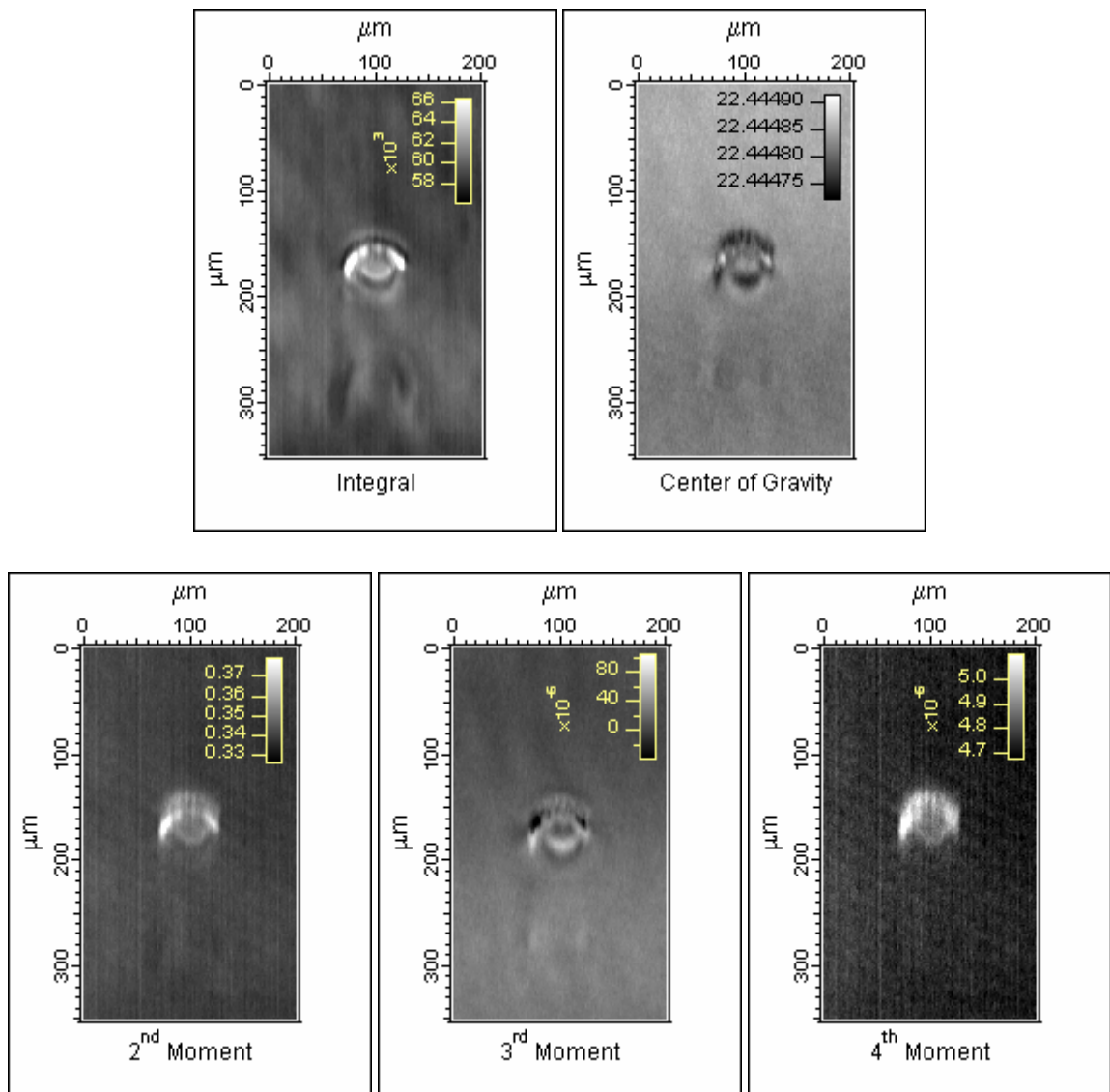
Figure 3.60. Low peak fluence fs laser spot 0 0 4 images showing moments Integral and Center of Gravity, 2nd, 3rd & 4th Moment about the Center of Gravity (Trial 2).

3.5   High Peak Fluence Nanosecond Laser Spot, 4.71 J/cm^2

The following section will deal with micrographs and topographs of a nanosecond laser spot irradiated with a peak fluence of 4.71 J/cm^2. Four sets of experiments were conducted on this spot in November 2003. The four sets of experiments were conducted to analyze topographs produced with the four different crystal reflections $115, 1\bar{1}5, \bar{1}\bar{1}5$ and $\bar{1}15$. As discussed earlier in the experimental section, the four reflections were brought into the diffraction condition from the $0\,0\,4$ pole by rotating the sample normal to the azimuth bringing the 115 poles into the diffraction plane. Comparisons of the four reflections will be made with respect to feature size.

3.5.1   Optical Microscopy

Figure 3.61 shows a micrograph of the high fluence nanosecond laser spot irradiated with 100 pulses, peak fluence on the spot being 4.71 J/cm^2. The horizontal size of the spot or crater is 76 μm. The vertical size of the spot or crater is about 40 μm. A horizontal and vertical linescan across the center of the micrograph reveals the contrast in more detail. Figure 3.62 and 3.63 show horizontal and vertical linescans across the center of the irradiated spot on the micrograph. The linescan shows the feature size of the damage. The micrograph shows that the incident laser beam had an odd shape and was poorly approximated as radially symmetric.
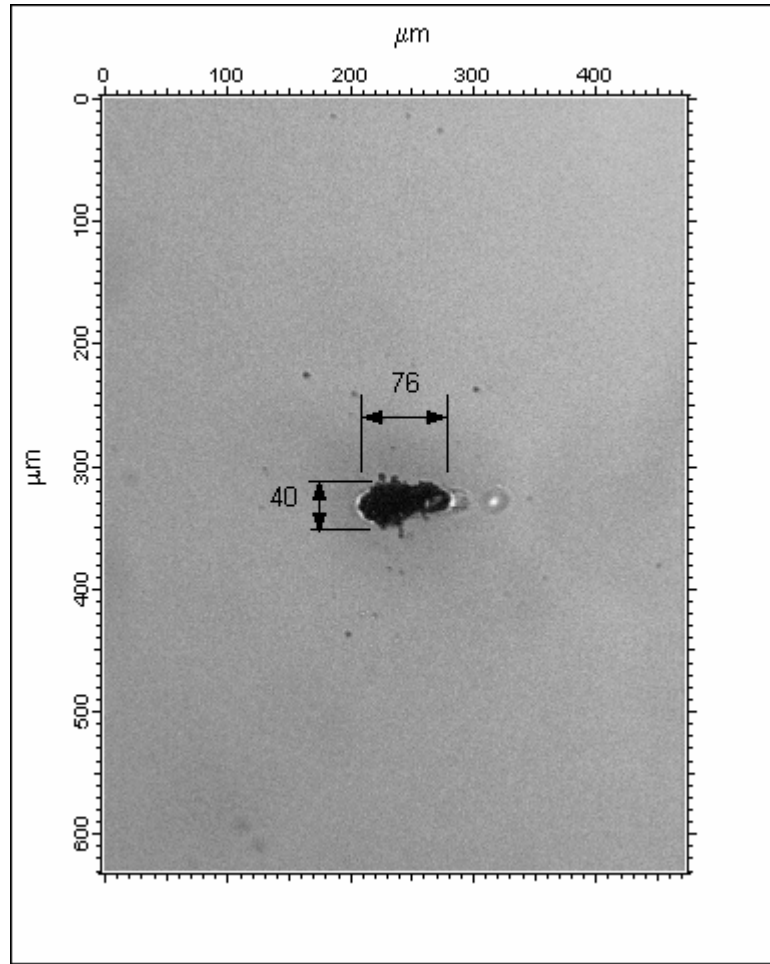
Figure 3.61. Optical micrograph showing feature size of high peak fluence (4.71 J/cm^2) nanosecond laser spot.
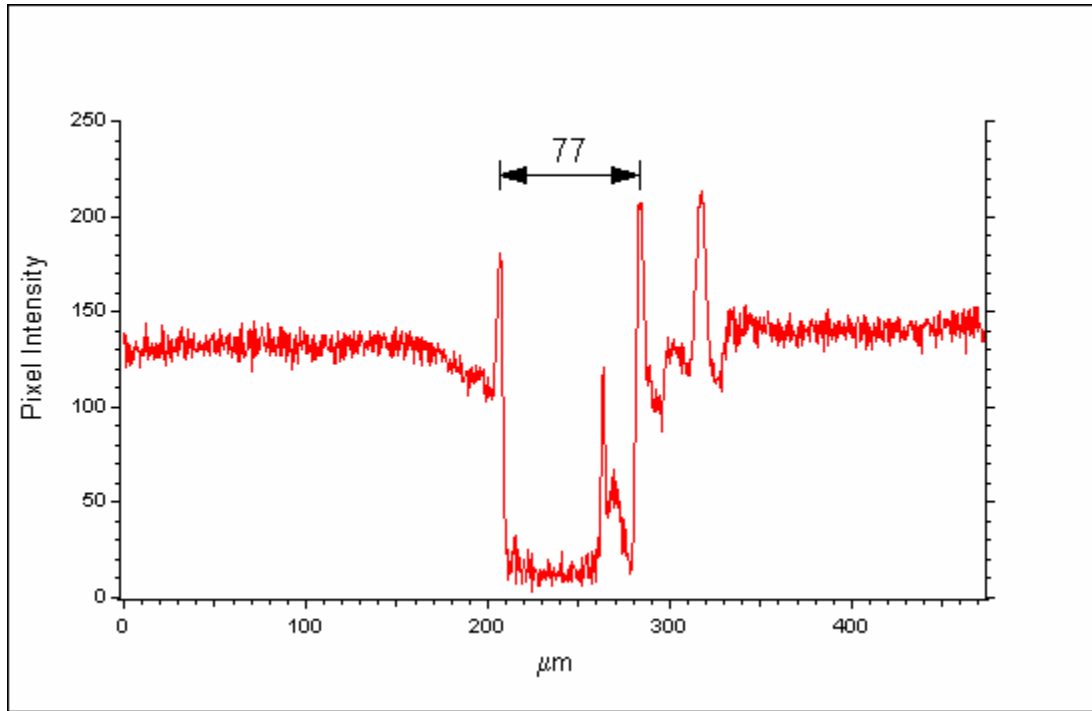
Figure 3.62. Horizontal linescan across micrograph of high peak fluence ns laser spot, showing feature size.
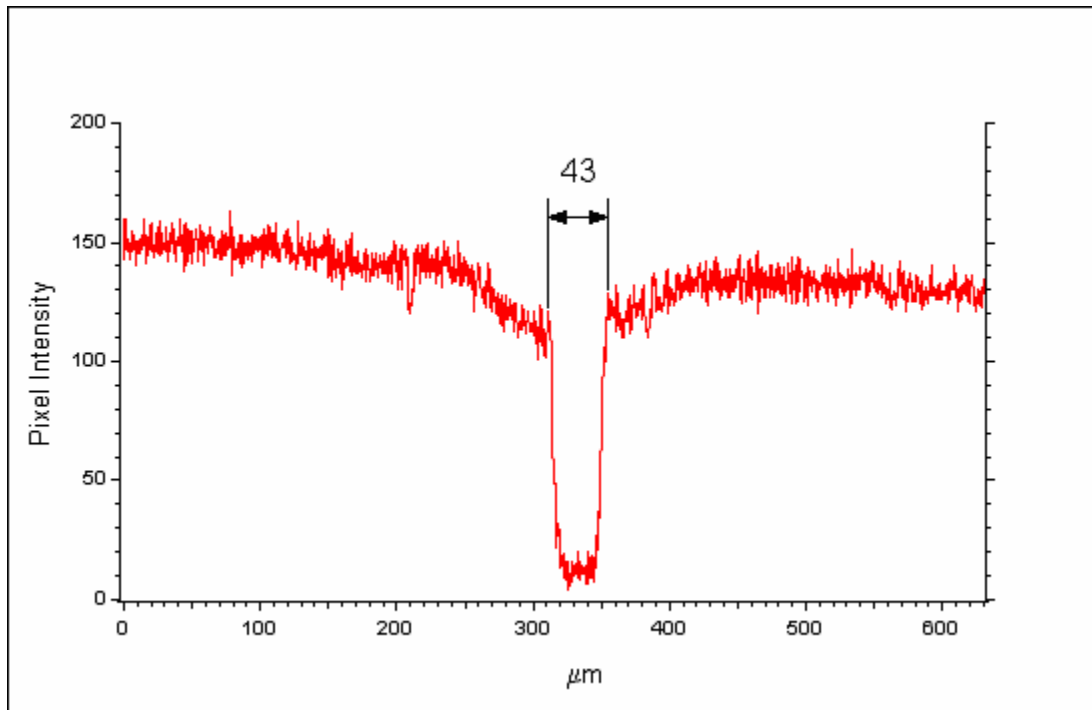
Figure 3.63. Vertical linescan across micrograph of high peak fluence ns laser spot, showing feature size.

3.5.2 Topography – Trial 1 - 115

The following section deals with the topographs of the nanosecond laser irradiated spot, with an h k l of 115. The topographs presented in this section were obtained during experimentation in November 2003 at the APS. The 115 pole was brought into diffraction condition by rotating the specimen by an azimuth of 45˚ with respect to the 0 0 4 reflection.

3.5.2.1 Slice Analysis

Figure 3.64 is an XY slice at the peak of the rocking curve. The XY slice is an image of the crystal diffracting at its Bragg peak, as seen by the CCD camera.
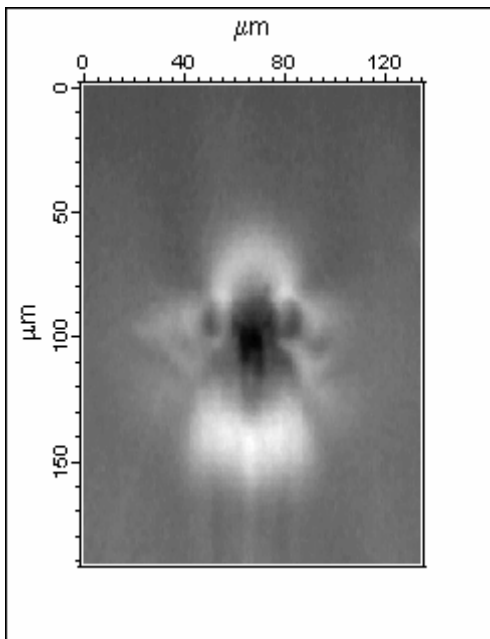
Figure 3.64. XY slice of high peak fluence ns laser spot 115 at the center of Bragg peak showing damage, as seen by the CCD camera.

Figure 3.65 is an image of the Xθ slice showing the diffracted intensity in the horizontal direction. The Xθ slice is extracted approximately across the center of the feature at a Y coordinate of 96 μm of the XY slice. The superimposed red line across the image is the image line profile that shows the change in intensity along the horizontal direction across the feature at a θ value of 13.74525˚. Figure 3.66 is an image of the Yθ slice with showing the extent of contrast in the vertical direction. The Yθ slice is extracted at X coordinate of 100 μm of the XY slice.

The characterization images, Figures 3.67 and 3.68, clearly show that the extent of the damage is well beyond the extent seen with a microscope. The arrows on the Maximum image show the location where the different rocking curves B, C, D and E were extracted to analyze the damage. A is the rocking curve of the undamaged crystal that is recorded far away from the extent of damage in the horizontal direction and its location is not shown in the images.

. Figures 3.69 and 3.70 show the comparisons of the five different rocking curves and Table 3.6 gives the data recorded from the five rocking curves. The discussion and comparison of the 115 data with the other reflections is done in section 3.5.6.
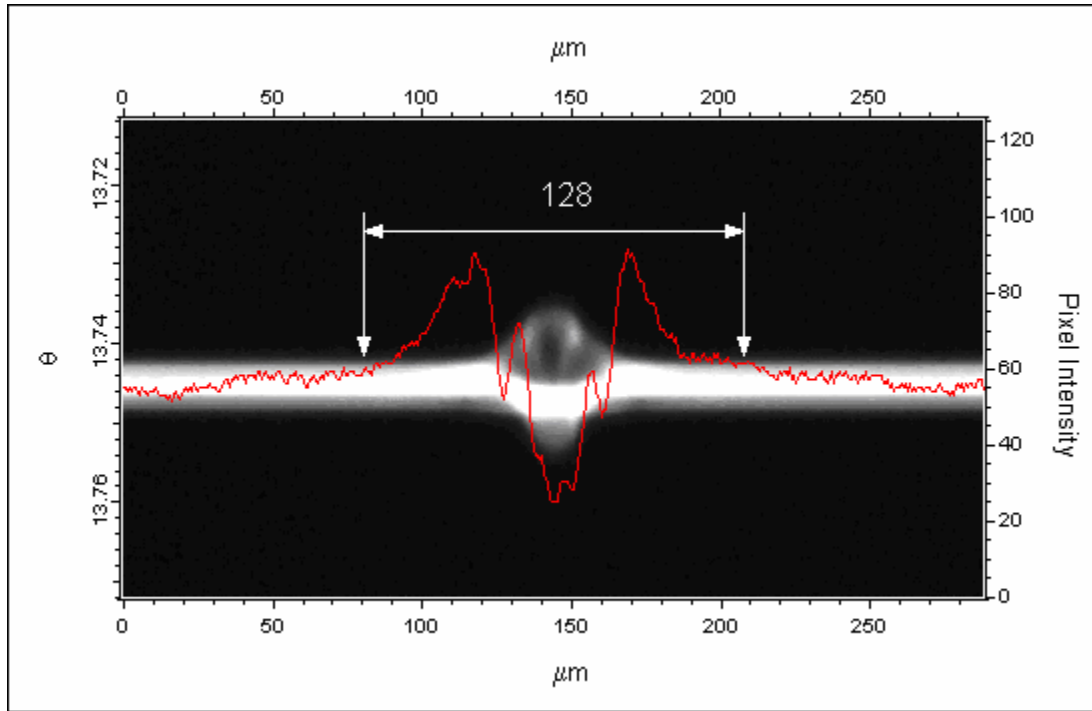
Figure 3.65. Xθ slice of high peak fluence ns laser spot 115 showing region of horizontal damage. The Xθ slice is taken at a Y value of 96 μm of the XY slice.
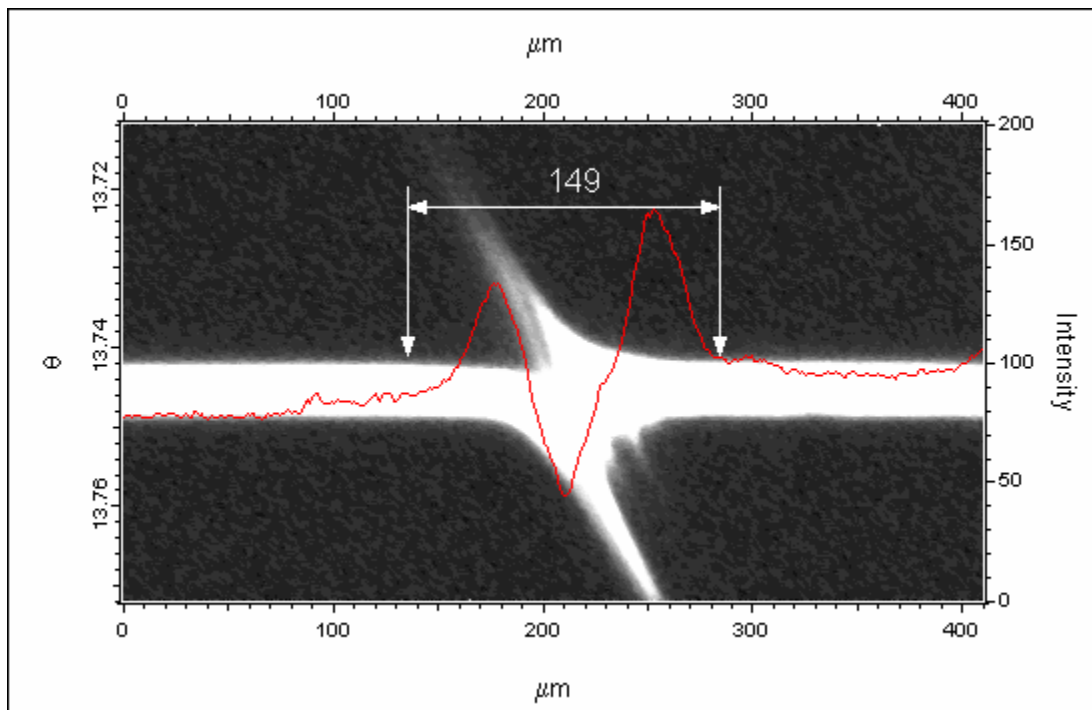
Figure 3.66. Yθ slice of high peak fluence ns laser spot 115 region of vertical damage. The Yθ slice is taken at an X value of 67 μm on the XY slice.

97

3.5.2.2 Image Analysis on Rocking Curve Characterizations

Figure 3.67 High peak fluence fs laser spot 115 images showing characterizations Maximum, Standard Deviation, FWHM, Maximum Location, Skew & Kurtosis. The maximum image shows the location of the rocking curves, at the arrow head.
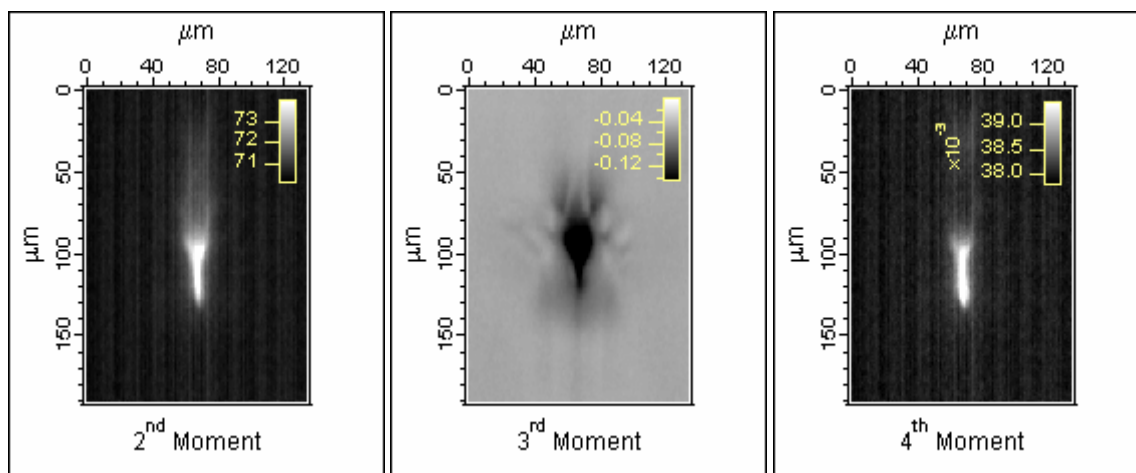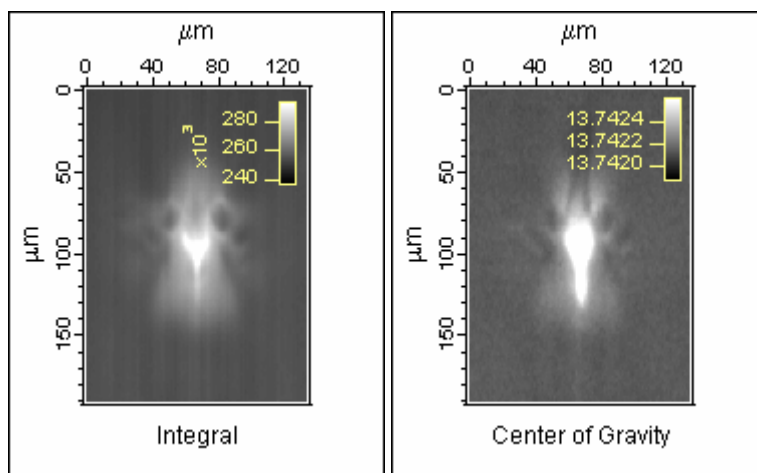
Figure 3.68. High peak fluence fs laser spot 115 images showing moments Integral and Center of Gravity, 2nd, 3rd & 4th Moment about the Center of Gravity.
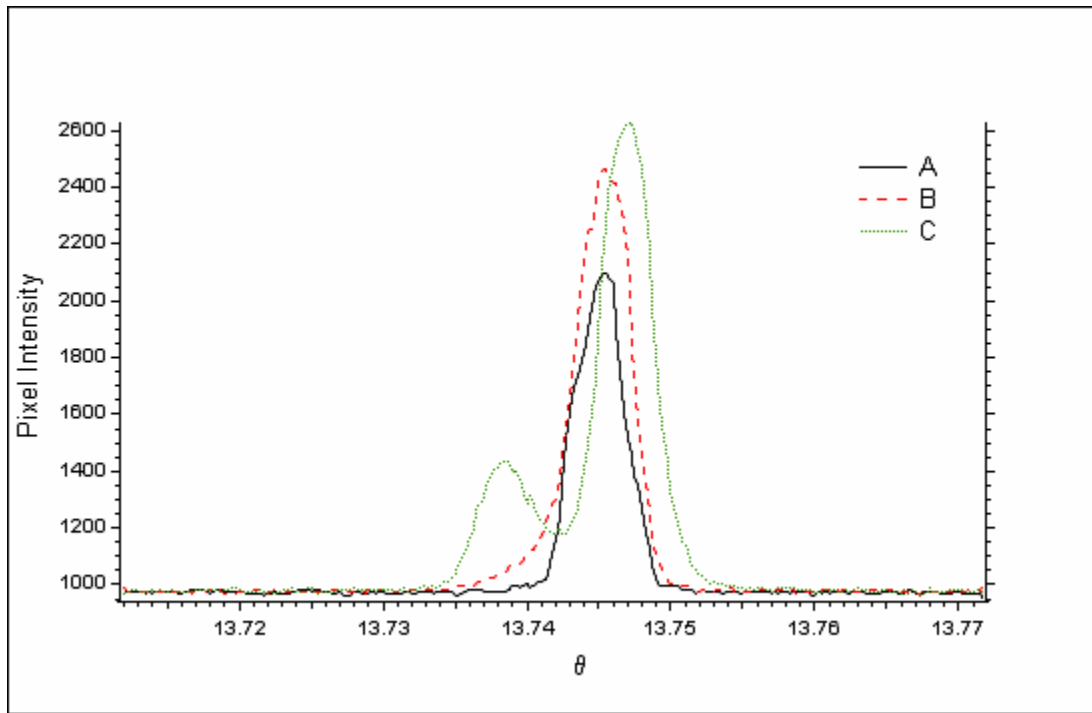
Figure 3.69. Comparison of rocking curves A, B & C of high peak fluence ns laser spot 115.
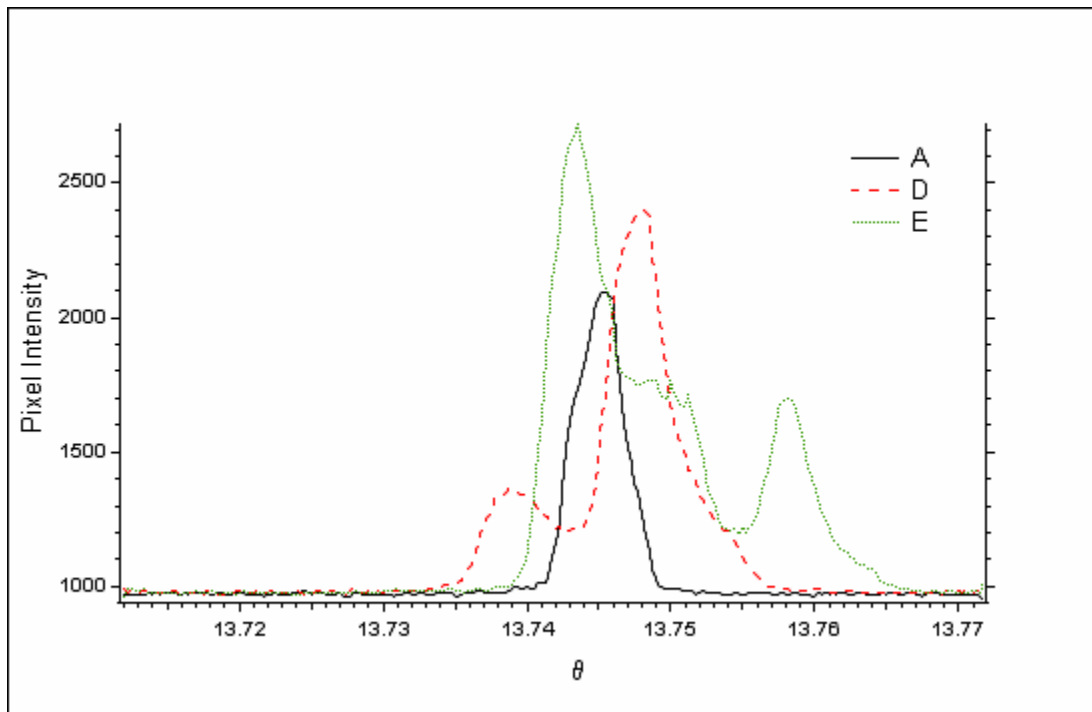
Figure 3.70. Comparison of rocking curves A, D & E of high peak fluence ns laser spot 115.

Table 3.6. Rocking curve details of high peak fluence ns laser spot 115.

Rocking Curve	Peak Intensity	Background Intensity	FWHM (arc sec)	FWHM (Curve) / FWHM (A)
A	2096	947	15.23	1.00
B	2464	964	16.05	1.05
C	2627	963	14.95	0.98
D	2403	969	16.76	1.10
E	2719	960	18.36	1.21

3.5.3 Topography – Trial 2 - $1\bar{1}5$

The following section deals with the topographs of the nanosecond laser irradiated spot, with an h k l of $1\bar{1}5$. The topographs presented in this section were obtained during experimentation in November 2003 at the APS. The $1\bar{1}5$ pole was brought into diffraction condition by rotating the specimen by an azimuth of 135˚ with respect to the $0\,0\,4$ reflection.

3.5.3.1 Slice Analysis

Figure 3.71 is an XY slice at the peak of the rocking curve. The XY slice is an image of the crystal diffracting at its Bragg peak, as seen by the CCD camera.
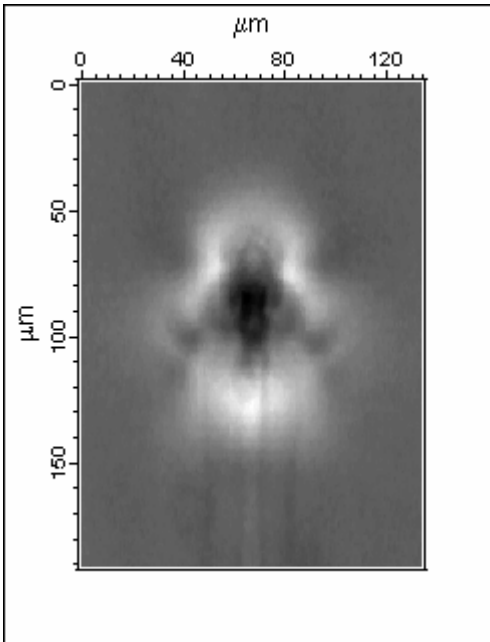
Figure 3.71. XY slice of high peak fluence ns laser spot $1\bar{1}5$ at the center of Bragg peak showing damage, as seen by the CCD camera.

Figure 3.72 is an image of the Xθ slice showing the diffracted intensity in the horizontal direction. The Xθ slice is extracted approximately across the center of the feature at a Y coordinate of 96 μm of the XY slice. The superimposed red line across the image is the image line profile that shows the change in intensity along the horizontal direction across the feature at a θ value of 13.8364˚. Figure 3.73 is an image of the Yθ slice with showing the extent of contrast in the vertical direction. The Yθ slice is extracted at X coordinate of 100 μm of the XY slice.

The characterization images, Figures 3.74 and 3.75, clearly show that the extent of the damage is well beyond the extent seen with a microscope. The Maximum image shows the location where the different rocking curves B, C, D and E were extracted to analyze the damage. A is the rocking curve of the undamaged crystal that is recorded far away from the extent of damage in the horizontal direction and its location is not shown in the images.

. Figures 3.76 and 3.77 show the comparisons of the five different rocking curves and Table 3.7 gives the data recorded from the five rocking curves. The discussion and comparison of the $1\bar{1}5$ data with the other reflections is done in section 3.5.6.
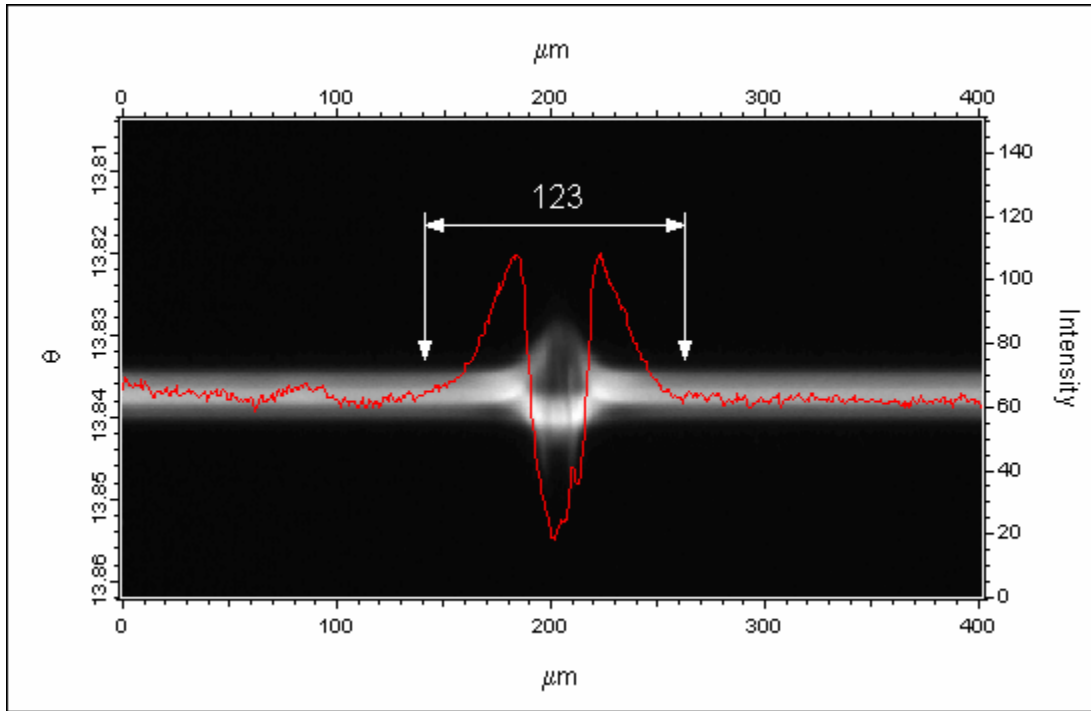
Figure 3.72. Xθ slice of high peak fluence ns laser spot $1\bar{1}5$ showing extent of horizontal damage. The Xθ slice is taken at a Y value of 96 μm of the XY slice.
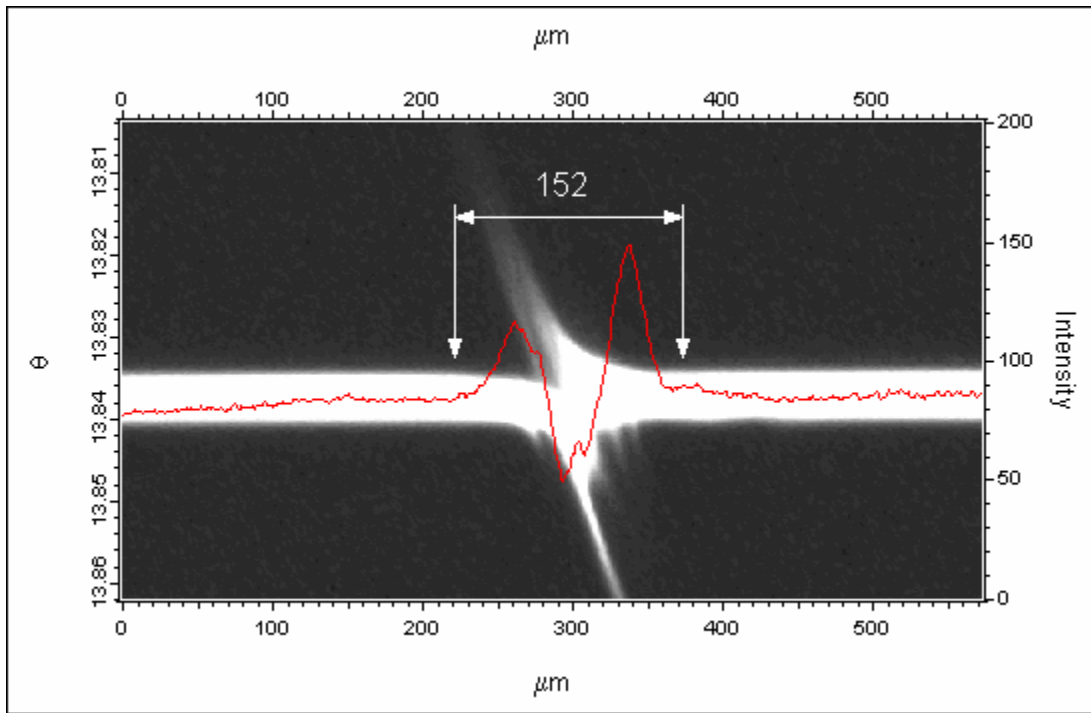
Figure 3.73. Yθ slice of high peak fluence ns laser spot $1\bar{1}5$ showing extent of vertical damage. The Yθ slice is taken at an X value of 67 μm on the XY slice.

3.5.3.2 Image Analysis on Rocking Curve Characterizations
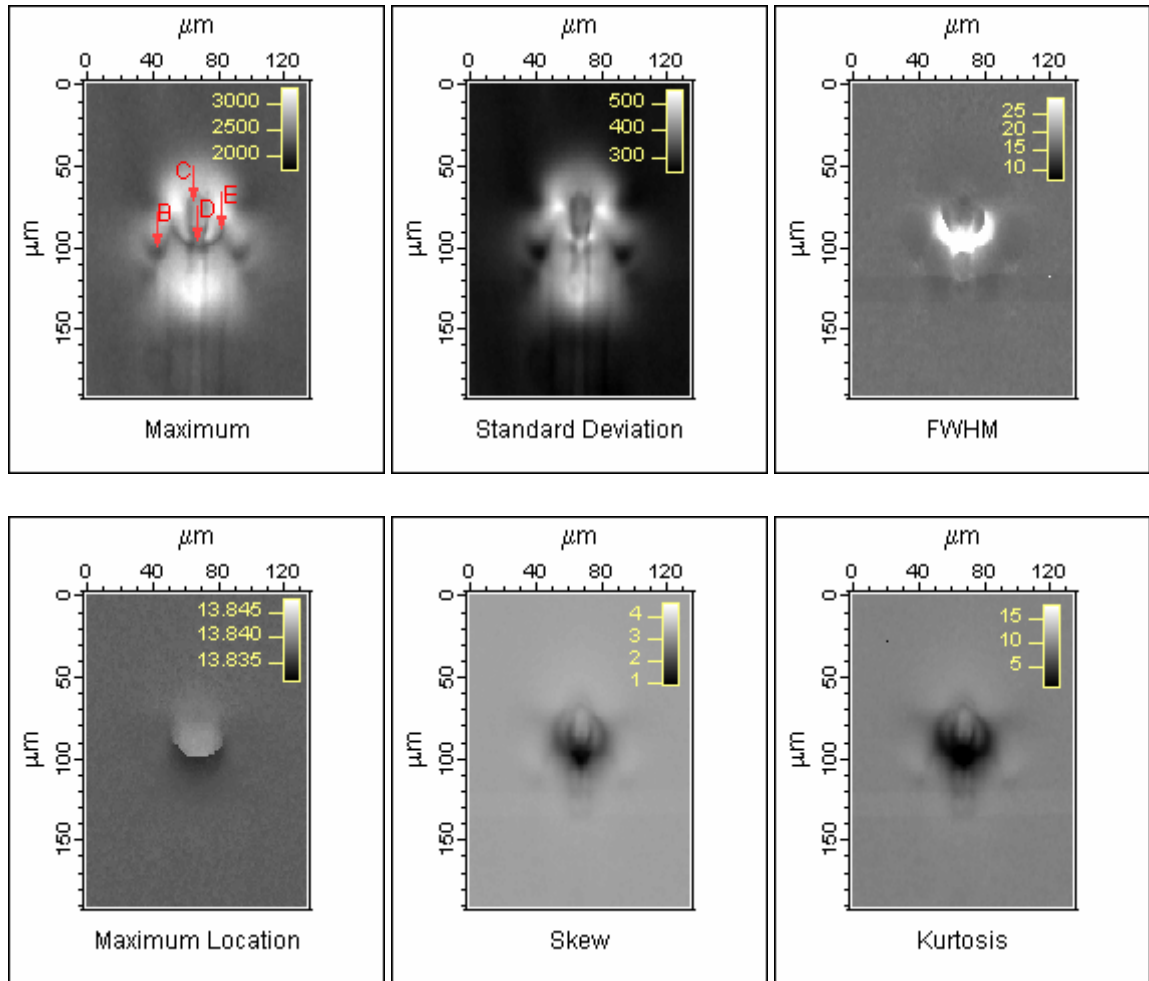
Figure 3.74. High peak fluence fs laser spot $1\bar{1}5$ images showing characterizations Maximum, Standard Deviation, FWHM, Maximum Location, Skew & Kurtosis. The maximum image shows the location of the rocking curves, at the arrow head.
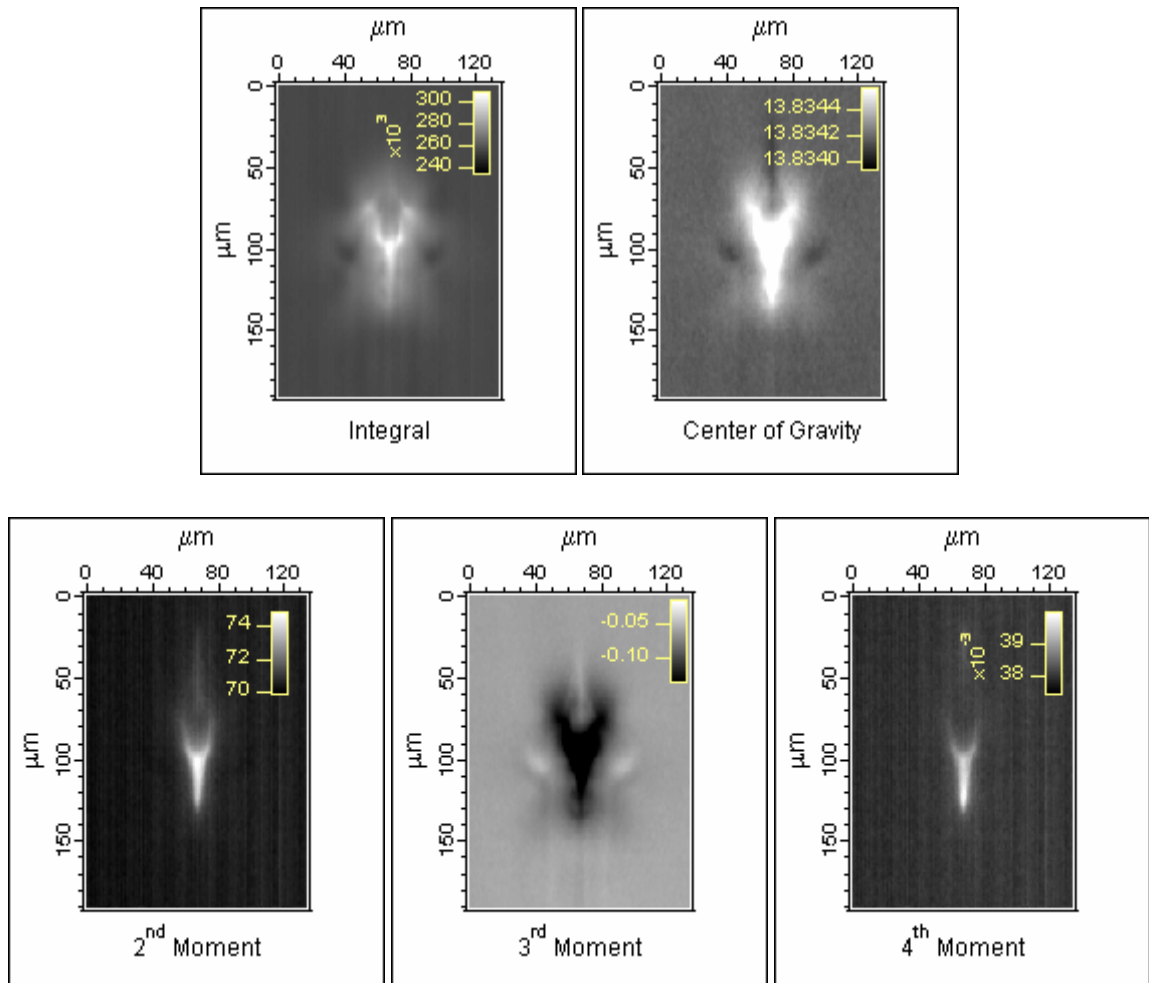
Figure 3.75. High peak fluence fs laser spot $1\bar{1}5$ images showing moments Integral and Center of Gravity, 2nd, 3rd & 4th Moment about the Center of Gravity.
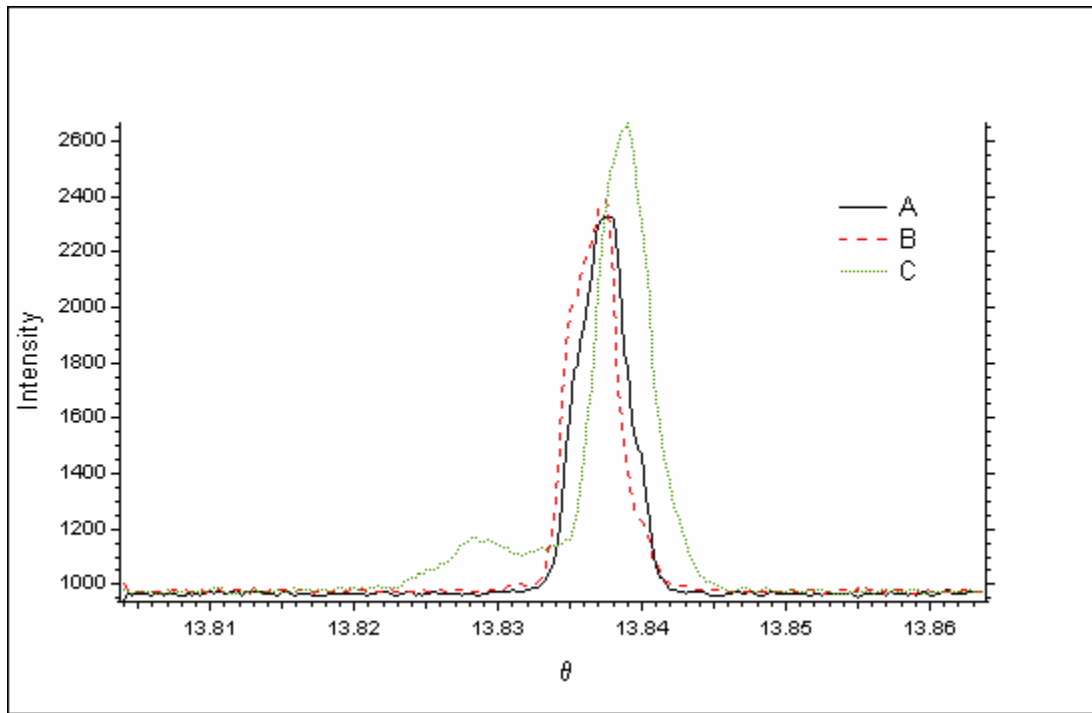
Figure 3.76. Comparison of rocking curves A, B & C of high peak fluence ns laser spot $1\bar{1}5$.
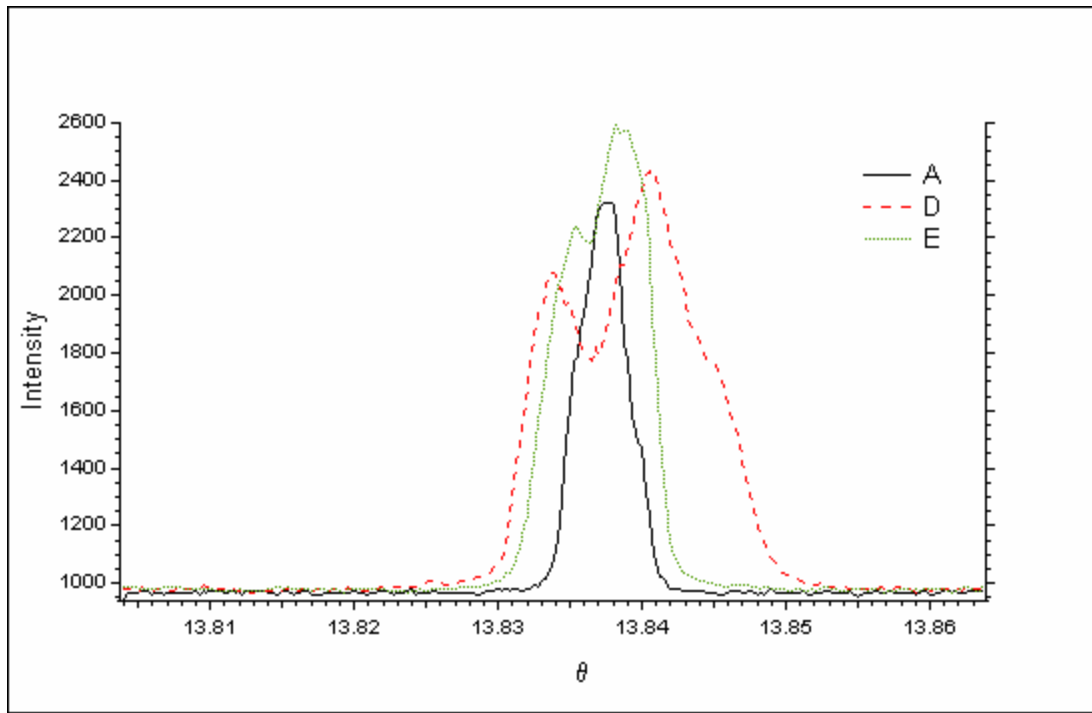
Figure 3.77. Comparison of rocking curves A, D & E of high peak fluence ns laser spot $1\bar{1}5$.

Table 3.7. Rocking curve details of high peak fluence ns laser spot $1\bar{1}5$.

Rocking Curve	Peak Intensity	Background Intensity	FWHM (arc sec)	FWHM (Curve) / FWHM (A)
A	2323	945	14.95	1.00
B	2393	965	14.14	0.95
C	2664	966	14.84	0.99
D	2438	966	48.84	3.27
E	2599	964	27.37	1.83

3.5.4   Topographs – Trial 3 - $\bar{1}\bar{1}5$

The following section deals with the topographs of the nanosecond laser irradiated spot, with an h k l of $\bar{1}\bar{1}5$. The topographs presented in this section were obtained during experimentation in November 2003 at the APS. The $\bar{1}\bar{1}5$ pole was brought into diffraction condition by rotating the specimen by an azimuth of 225° with respect to the $0\,0\,4$ reflection.

3.5.4.1 Slice Analysis

Figure 3.78 is an XY slice at the peak of the rocking curve. The XY slice is an image of the crystal diffracting at its Bragg peak, as seen by the CCD camera.
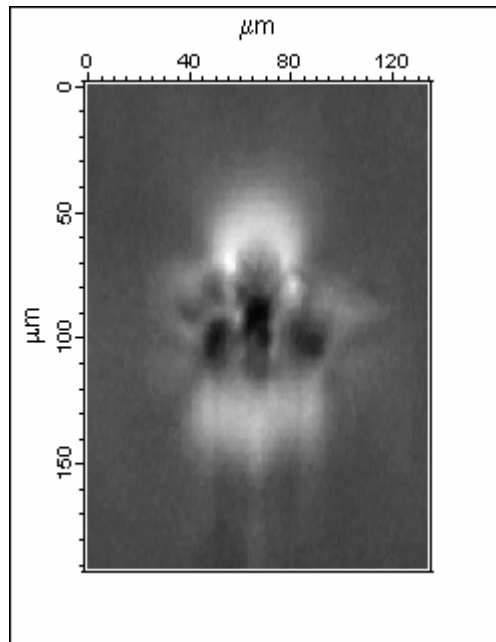
Figure 3.78. XY slice of high peak fluence ns laser spot $\bar{1}\bar{1}5$ at the center of Bragg peak showing damage, as seen by the CCD camera.

Figure 3.79 is an image of the Xθ slice showing the diffracted intensity in the horizontal direction. The Xθ slice is extracted approximately across the center of the feature at a Y coordinate of 96 μm of the XY slice. The superimposed red line across the image is the image line profile that shows the change in intensity along the horizontal direction across the feature at a θ value of 13.9123°. Figure 3.80 is an image of the Yθ slice with showing the extent of contrast in the vertical direction. The Yθ slice is extracted at X coordinate of 100 μm of the XY slice.

The characterization images, Figures 3.81 and 3.82, clearly show that the extent of the damage is well beyond the extent seen with a microscope. The Maximum image shows the location where the different rocking curves B, C, D and E were extracted to analyze the damage. A is the rocking curve of the undamaged crystal that is recorded far away from the extent of damage in the horizontal direction and its location is not shown in the images.

. Figures 3.83 and 3.84 show the comparisons of the five different rocking curves and Table 3.8 gives the data recorded from the five rocking curves. The discussion and comparison of the $1\bar{1}\bar{5}$ data with the other reflections is done in section 3.5.6.
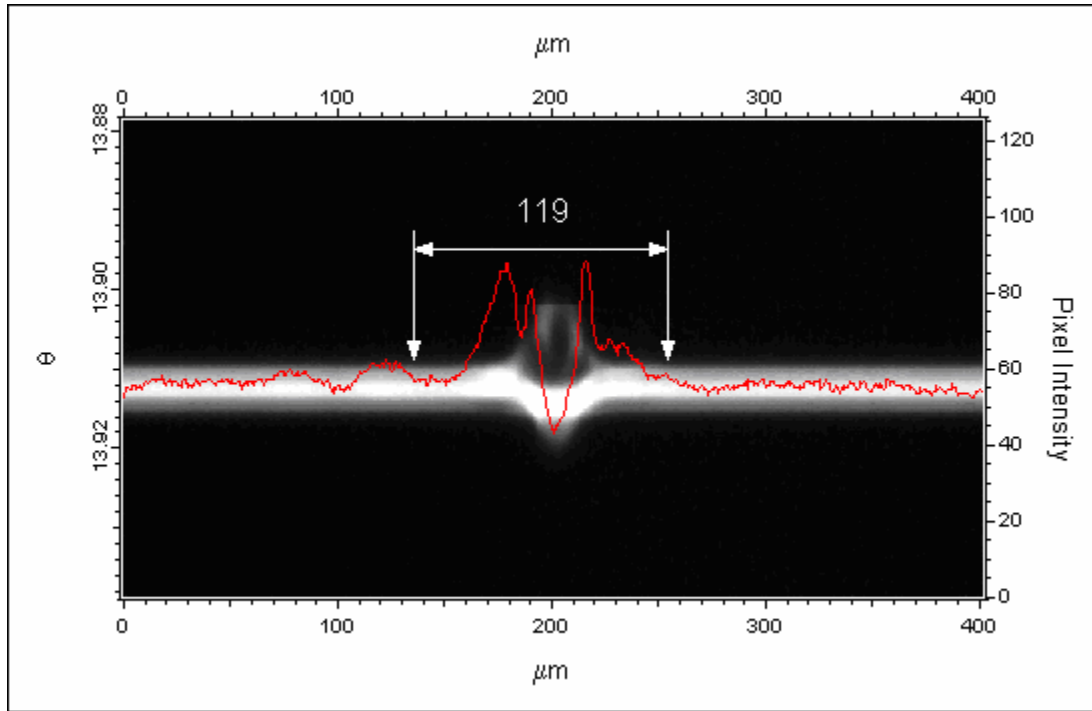
Figure 3.79. Xθ slice of high peak fluence ns laser spot $\overline{1}\overline{1}5$ showing extent of horizontal damage. The Xθ slice is taken at a Y value of 96 μm of the XY slice.
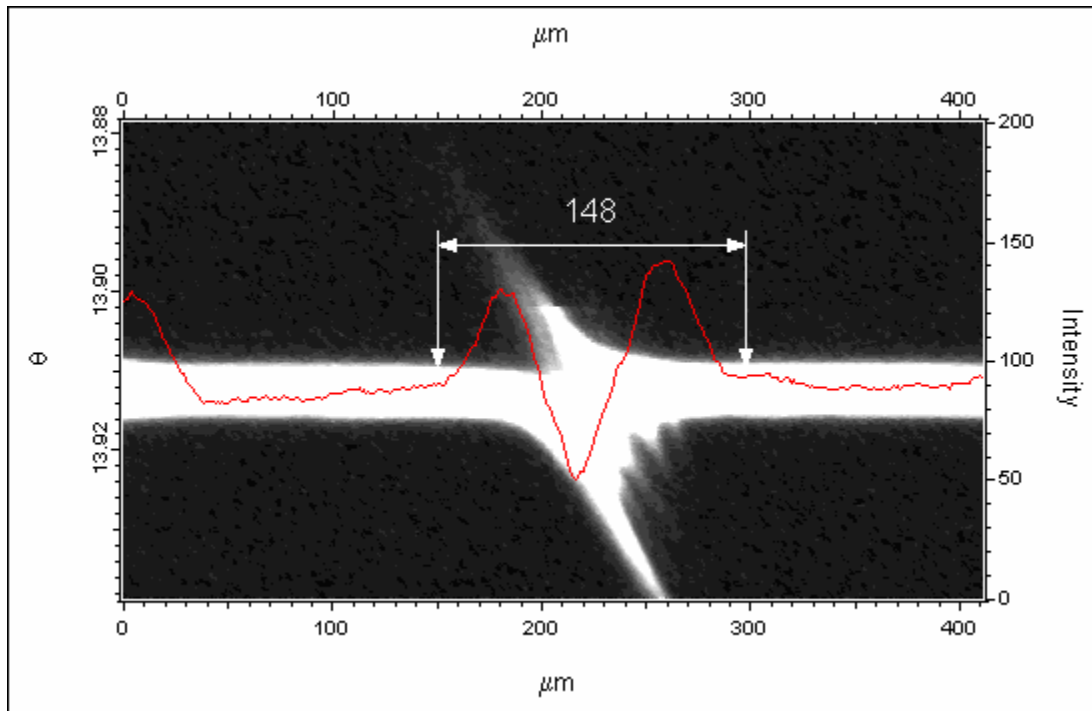
Figure 3.80. Yθ slice of high peak fluence ns laser spot $\overline{1}\overline{1}5$ showing vertical damage. The Yθ slice is taken at an X value of 67 μm on the XY slice.

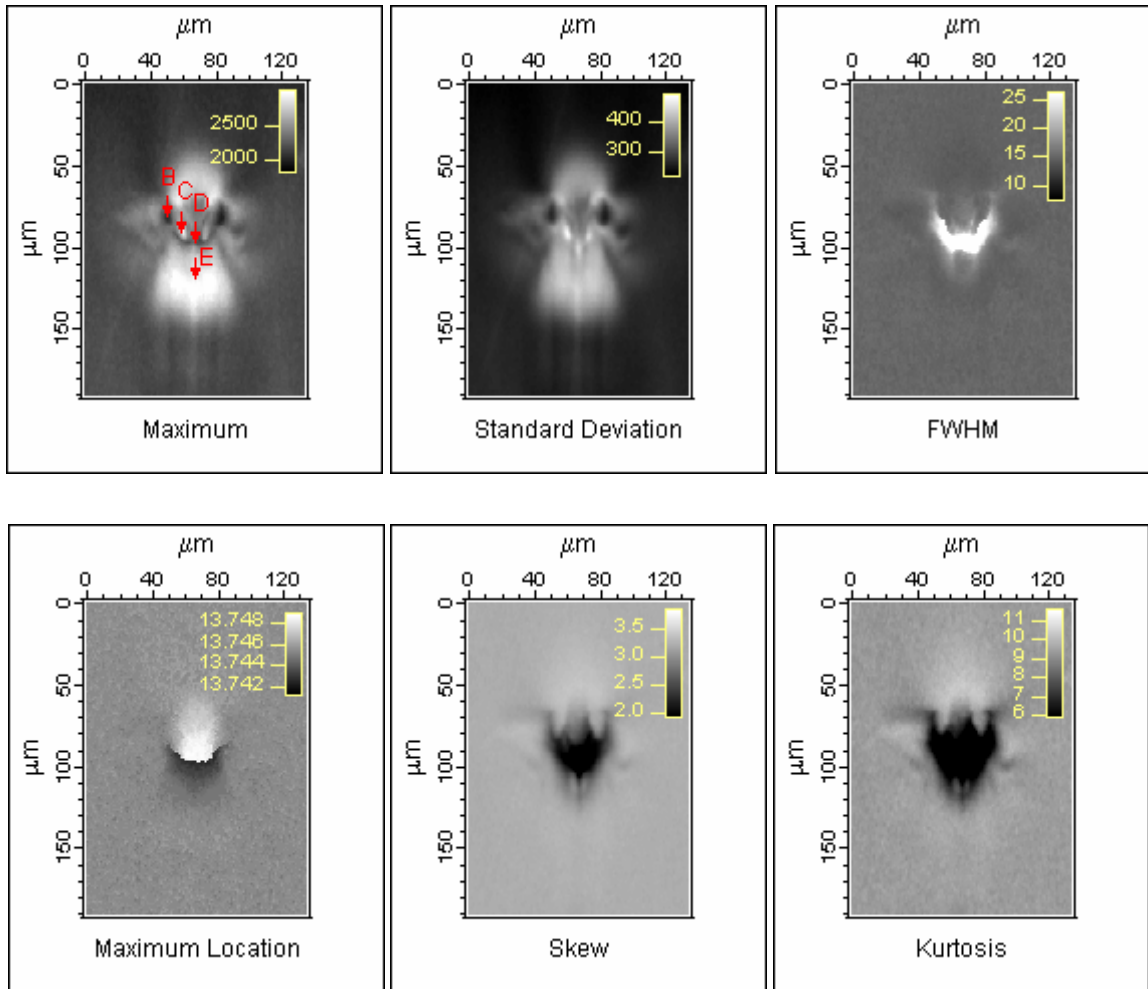## 3.5.4.2 Image Analysis on Rocking Curve Characterizations
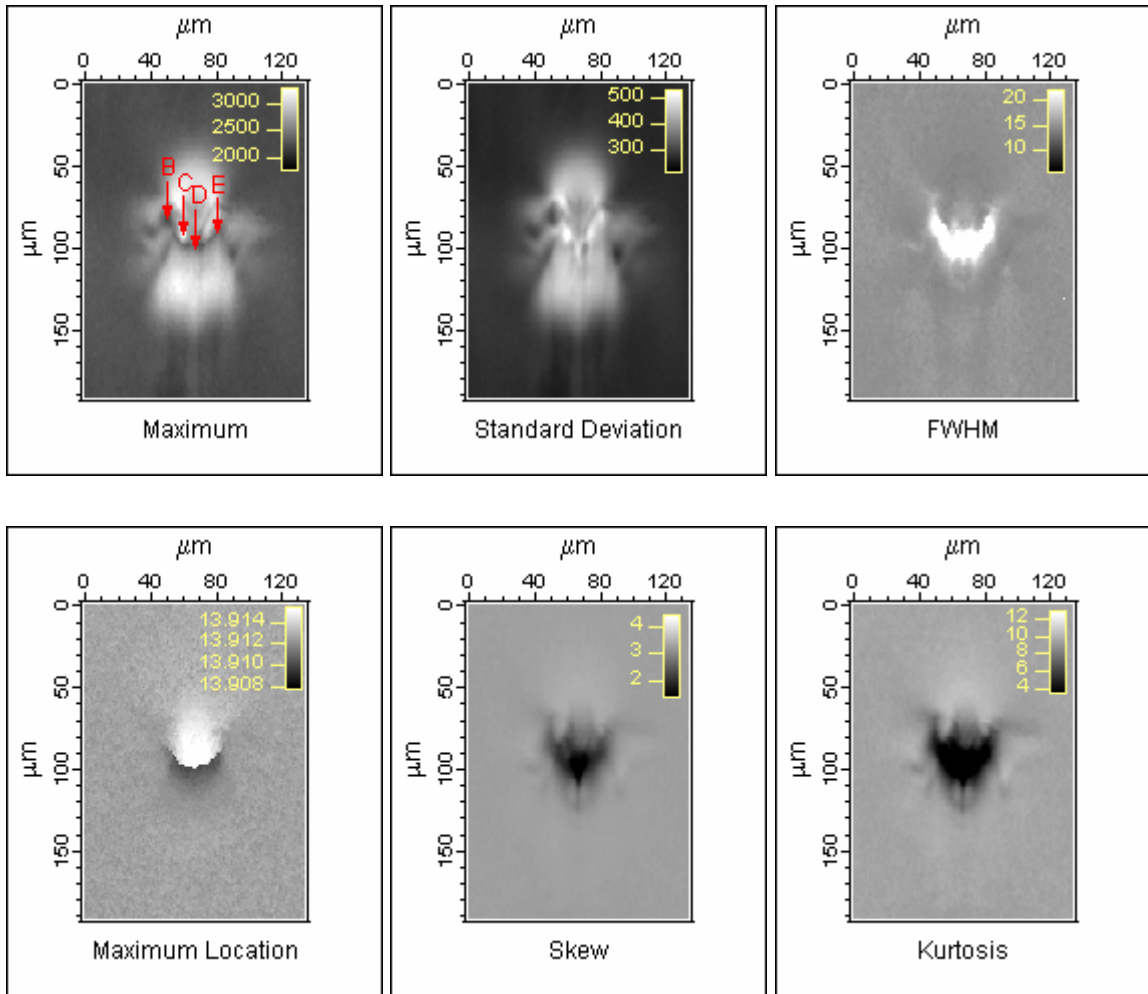
Figure 3.81. High peak fluence fs laser spot $\bar{1}\bar{1}5$ images showing characterizations Maximum, Standard Deviation, FWHM, Maximum Location, Skew & Kurtosis. The maximum image shows the location of the rocking curves, at the arrow head.
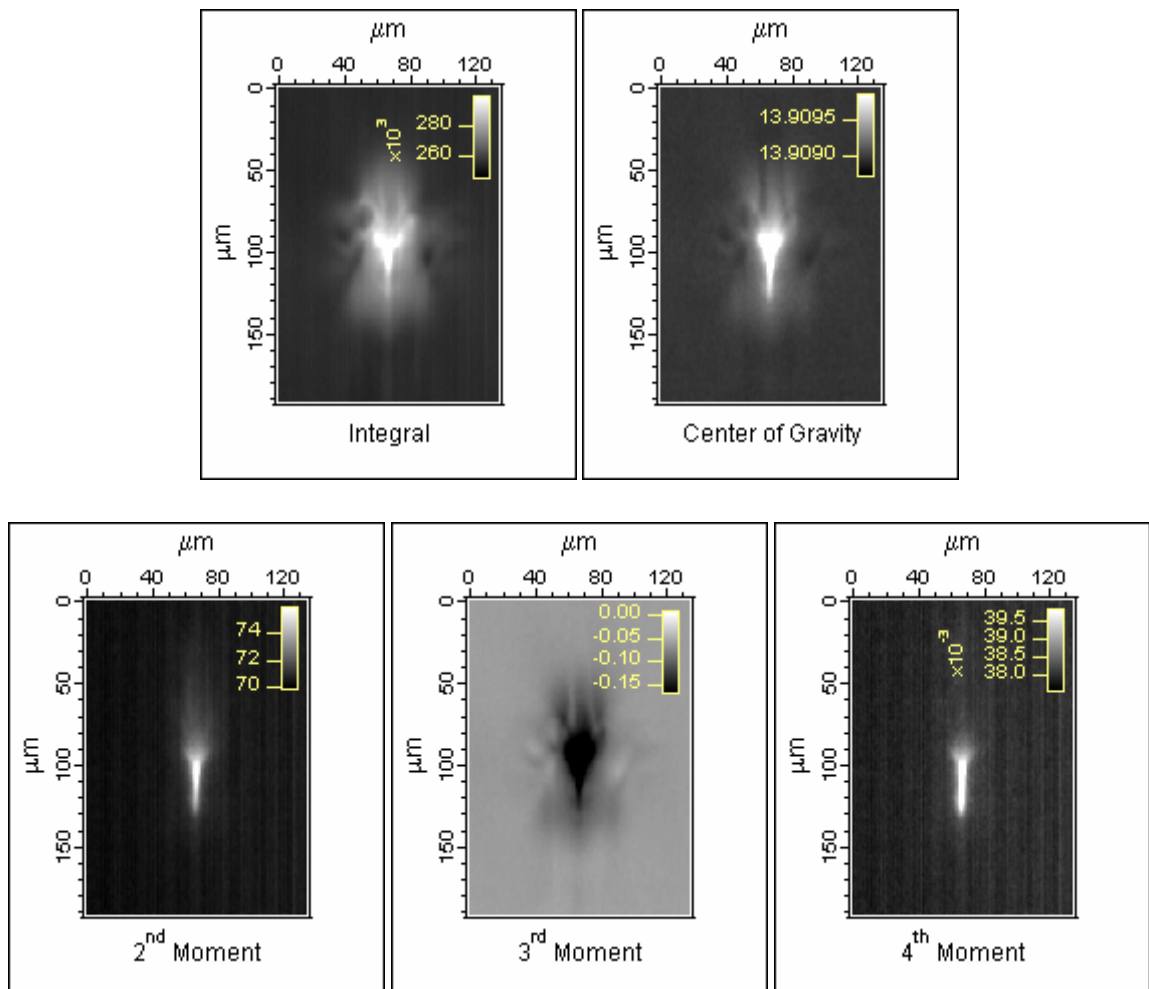
Figure 3.82. High peak fluence fs laser spot 115 images showing moments Integral and Center of Gravity, 2nd, 3rd & 4th Moment about the Center of Gravity.
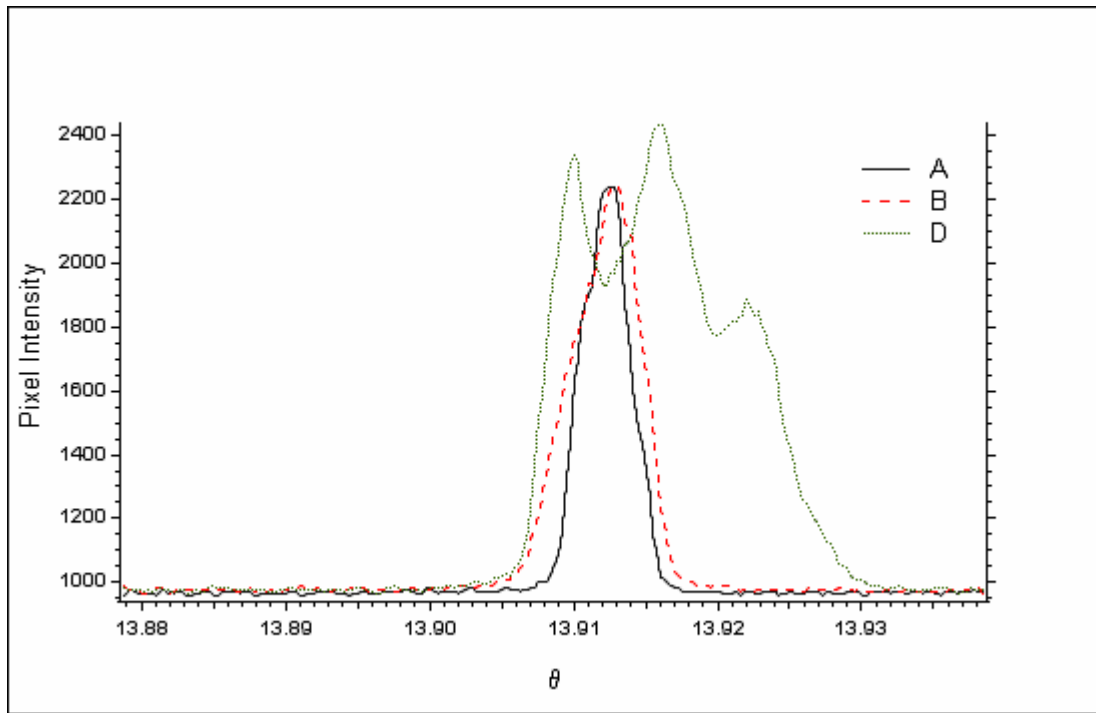
Figure 3.83. Comparison of rocking curves A, B & D of high peak fluence ns laser spot $\bar{1}\bar{1}5$.
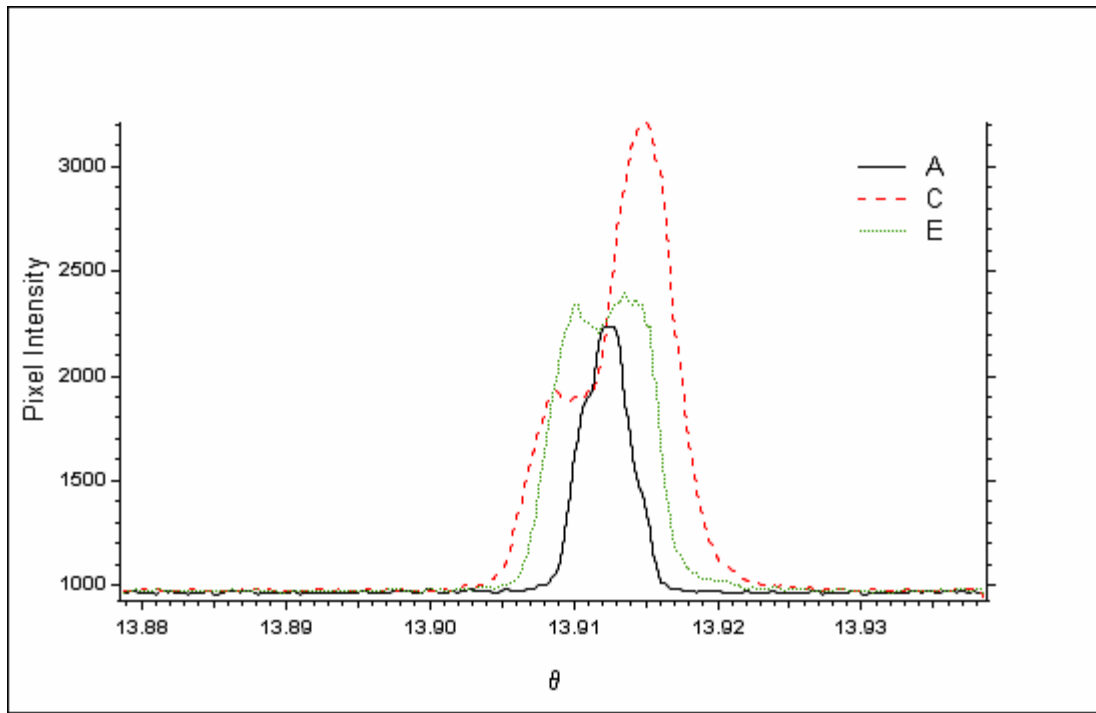
Figure 3.84. Comparison of rocking curves A, C & E of high peak fluence ns laser spot $\bar{1}\bar{1}5$.

Table 3.8. Rocking curve details of high peak fluence ns laser spot $\overline{1}\overline{1}5$.

Rocking Curve	Peak Intensity	Background Intensity	FWHM (arc sec)	FWHM (Curve) FWHM (A)
A	2236	957	15.00	1.00
B	2245	945	21.32	1.42
C	3208	936	19.53	1.30
D	2440	963	57.15	3.81
E	2392	953	28.93	1.93

One important point to notice here is that the extent of the damage seen in the high peak fluence nanosecond laser spot is a lot smaller than the damage shown by the high fluence femtosecond laser spot. The high power femtosecond laser damage measured on the same $\overline{1}\overline{1}5$ crystal plane shows a horizontal damage of 154 μm and a vertical damage of 288 μm which is more than the damage shown by the nanosecond laser damage measured on the same $\overline{1}\overline{1}5$ crystal plane. However, both the high power lasers show the existence of a slowly decaying intensity away from the central damaged region.

3.5.5   Topographs – Trial 4 - $\bar{1}15$

The following section deals with the topographs of the nanosecond laser irradiated spot, with an h k l of $\bar{1}15$. The topographs presented in this section were obtained during experimentation in November 2003 at the APS. The $\bar{1}15$ pole was brought into diffraction condition by rotating the specimen by an azimuth of -45˚ with respect to the 004 reflection.

3.5.5.1 Slice Analysis

Figure 3.85 is an XY slice at the peak of the rocking curve. The XY slice is an image of the crystal diffracting at its Bragg peak, as seen by the CCD camera.
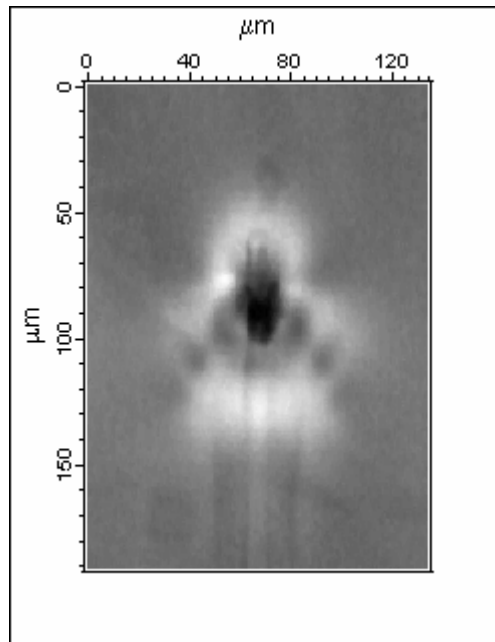
Figure 3.85. XY slice of high peak fluence ns laser spot $\bar{1}15$ at the center of Bragg peak showing damage, as seen by the CCD camera.

Figure 3.86 is an image of the Xθ slice showing the diffracted intensity in the horizontal direction. The Xθ slice is extracted approximately across the center of the feature at a Y coordinate of 96 μm of the XY slice. The superimposed red line across the image is the image line profile that shows the change in intensity along the horizontal direction across the feature at a θ value of 13.8165˚. Figure 3.87 is an image of the Yθ slice with showing the extent of contrast in the vertical direction. The Yθ slice is extracted at X coordinate of 100 μm of the XY slice.

The characterization images, Figures 3.88 and 3.89, clearly show that the extent of the damage is well beyond the extent seen with a microscope. The Maximum image shows the location where the different rocking curves B, C, D and E were extracted to analyze the damage. A is the rocking curve of the undamaged crystal that is recorded far away from the extent of damage in the horizontal direction and its location is not shown in the images.

. Figures 3.90 and 3.91 show the comparisons of the five different rocking curves and Table 3.9 gives the data recorded from the five rocking curves. The discussion and comparison of the $\bar{1}15$ data with the other reflections is done in section 3.5.6.

117
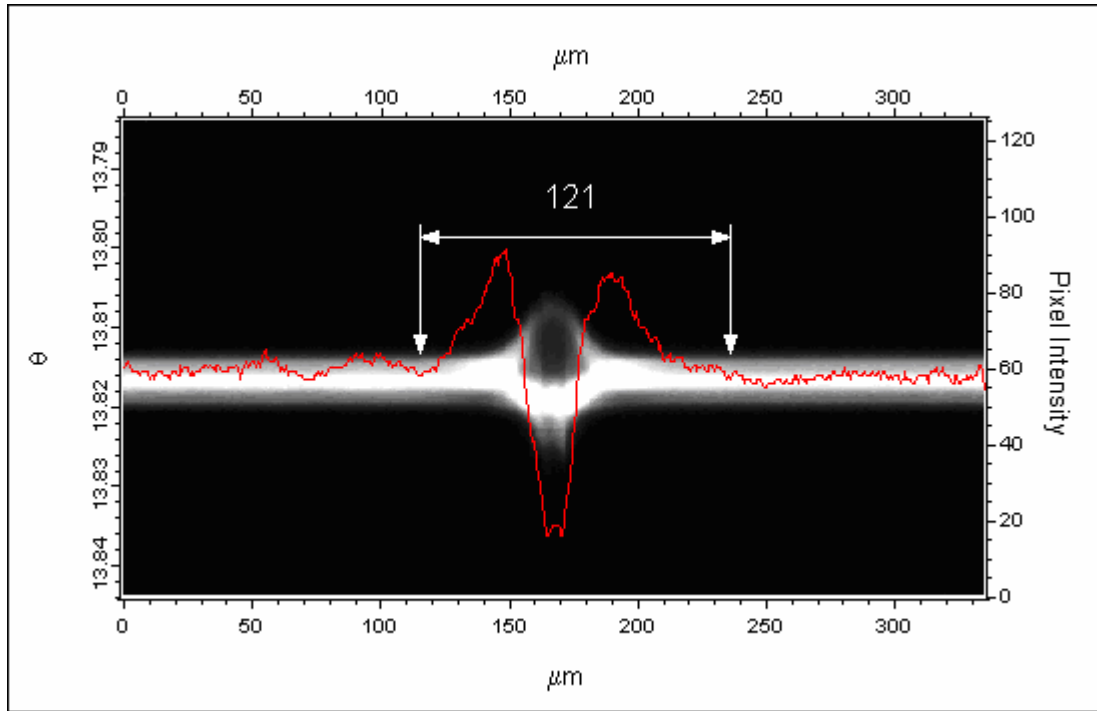
Figure 3.86. Xθ slice of high peak fluence ns laser spot $\overline{1}15$ showing extent of horizontal damage. The Xθ slice is taken at a Y value of 96 μm of the XY slice.
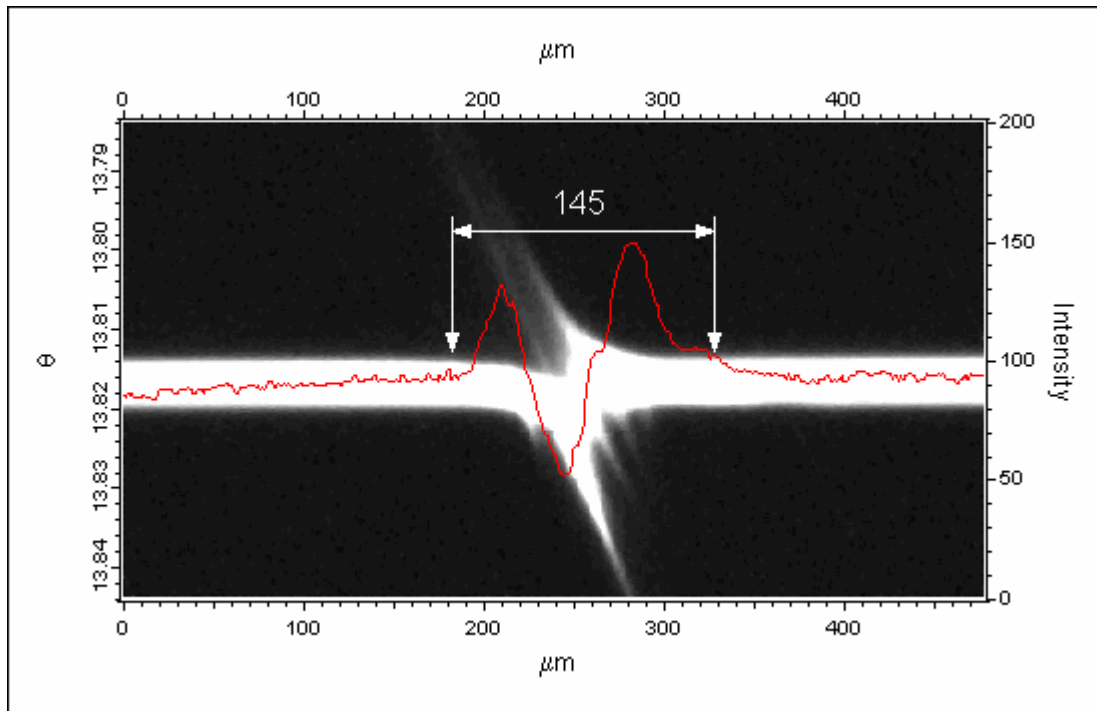
Figure 3.87. Yθ slice of high peak fluence ns laser spot $\overline{1}15$ showing extent of vertical damage. The Yθ slice is taken at an X value of 67 μm on the XY slice.

3.5.5.2 Image Analysis on Rocking Curve Characterizations
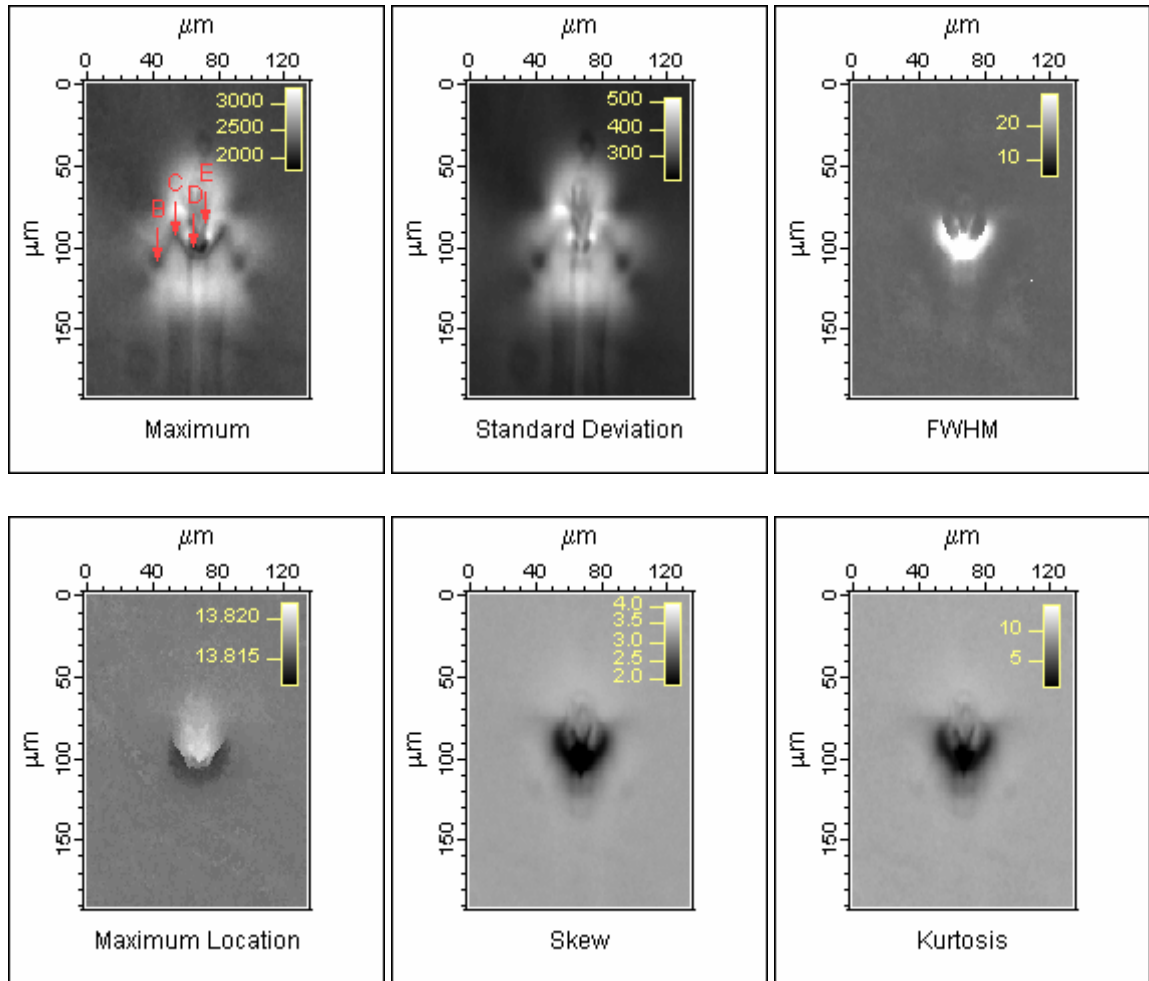
Figure 3.88. High peak fluence fs laser spot $\overline{1}15$ images showing characterizations Maximum, Standard Deviation, FWHM, Maximum Location, Skew & Kurtosis. The maximum image shows the location of the rocking curves, at the arrow head.
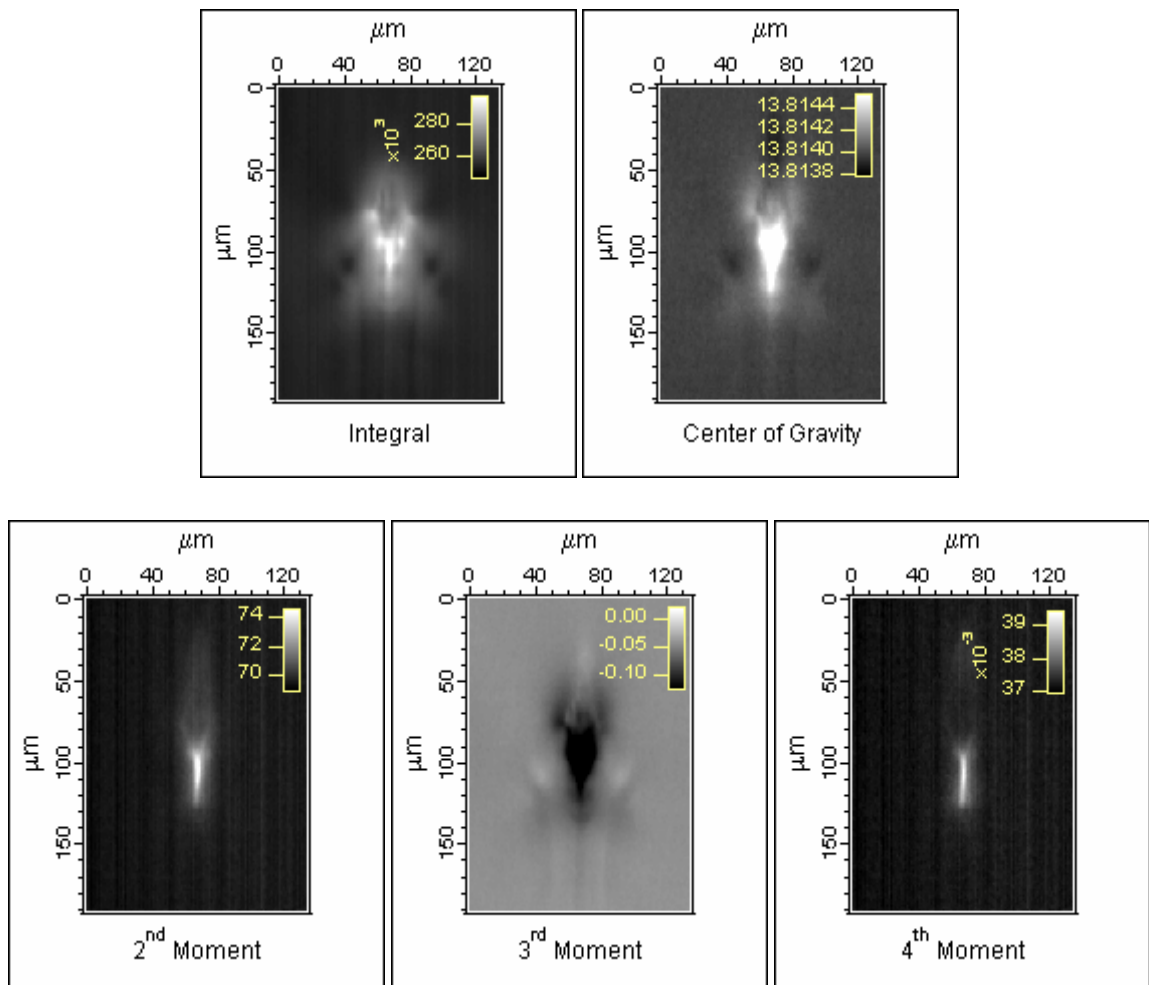
Figure 3.89. High peak fluence fs laser spot $\bar{1}15$ images showing moments Integral and Center of Gravity, 2nd, 3rd & 4th Moment about the Center of Gravity.
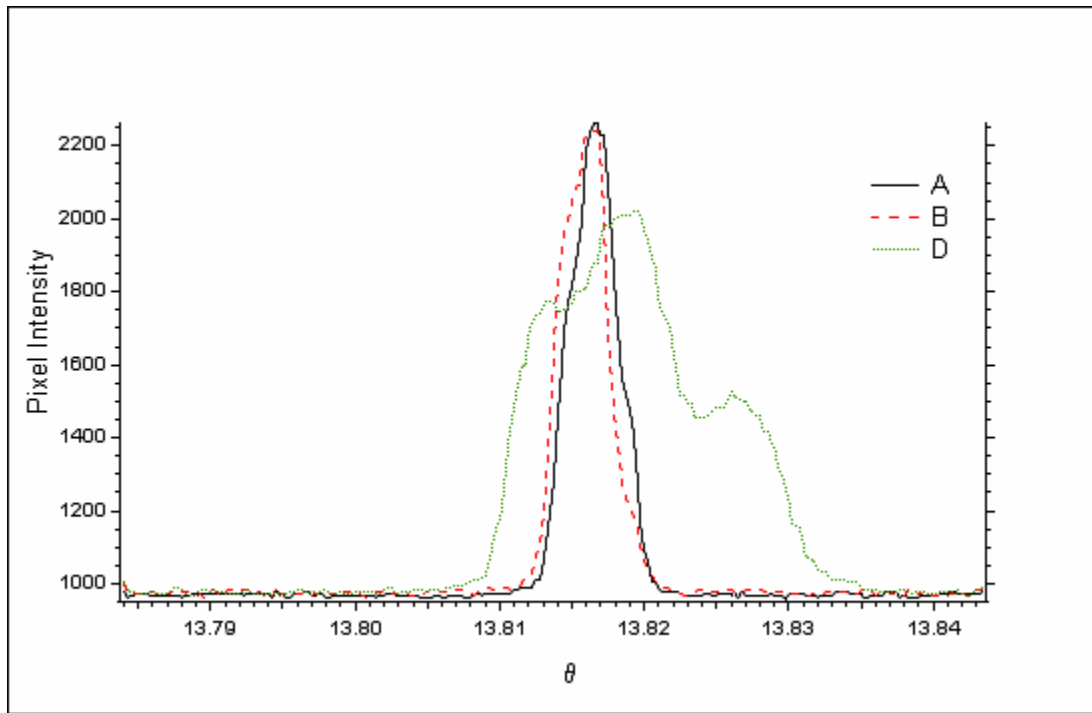
Figure 3.90. Comparison of rocking curves A, B & D of high peak fluence ns laser spot $\bar{1}15$.
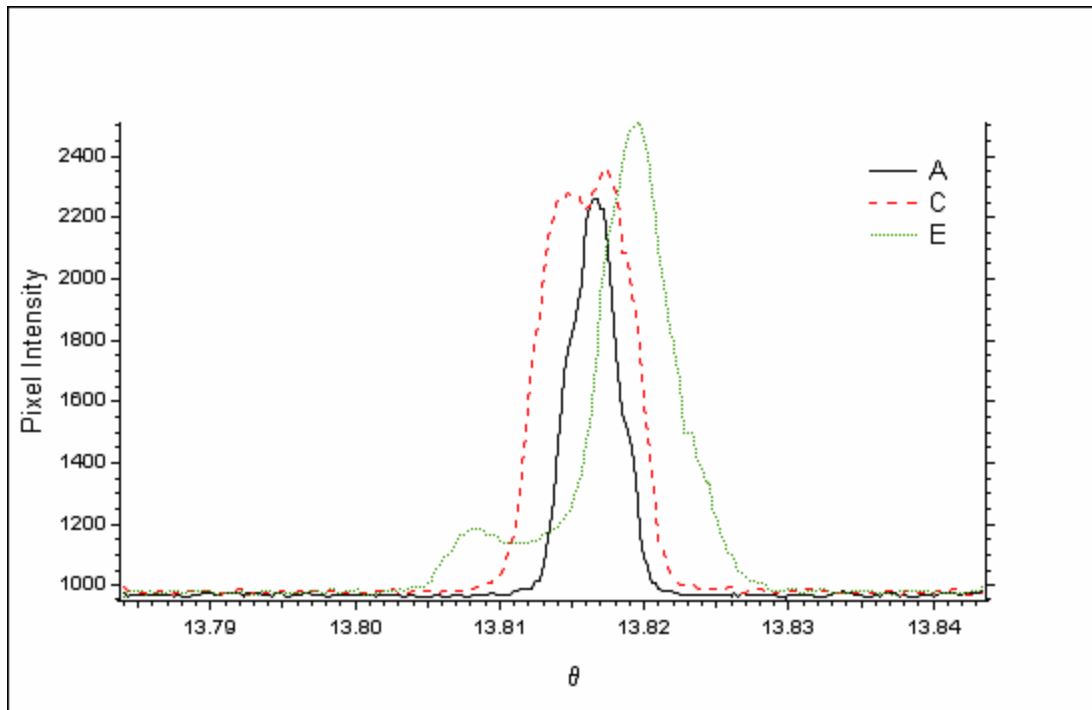
Figure 3.91. Comparison of rocking curves A, C & E of high peak fluence ns laser spot $\bar{1}15$.

Table 3.9. Rocking curve details of high peak fluence ns laser spot $\bar{1}15$.

Rocking Curve	Peak Intensity	Background Intensity	FWHM (arc sec)	FWHM (Curve) / FWHM (A)
A	2262	956	14.56	1.00
B	2241	960	14.23	0.98
C	2359	968	27.97	1.92
D	2022	967	42.93	2.95
E	2508	963	19.98	1.37

3.5.6 Discussions for Topography – Trials 1, 2, 3 & 4

Table 3.10 summarizes the extent of horizontal and vertical damage seen in the topographs from Trials 1, 2, 3 and 4.

Table 3.10. Summary of horizontal and vertical damage in the topographs fromTrials 1, 2, 3 and 4.

Trial	h k l	Horizontal Feature Size (µm)	Vertical Feature Size (µm)
1	1 1 5	128	149
2	1 $\bar{1}$ 5	122	152
3	$\bar{1}$ $\bar{1}$ 5	119	148
4	$\bar{1}$ 1 5	121	145

Figure 3.65, 3.72, 3.79 and 3.86 show the Xθ slice showing the extent of damage in the horizontal direction. The Xθ slice is extracted at Y coordinate of 96 µm of the XY slice for each Trial. As seen in Table 3.10, the damage extends horizontally for 128 µm, 122 µm, 119 µm and 121 µm for Trials 1, 2, 3 and 4, respectively. It can be seen that the horizontal damage is consistent for different h k l planes that observed at different azimuths even thought the irradiated spot is not radially symmetrical.

Figures 3.66, 3.73, 3.80 and 3.87 show the Yθ slice showing the extent of damage in the vertical direction. The Yθ slice is extracted at X coordinate of 67 µm of the XY slice for each Trial. The damage in the vertical direction across the feature measures 149, 152, 148 and 145 µm for Trials 1, 2, 3 and 4, respectively. It can be seen that the feature sizes are very consistent even in the vertical direction

The arrows B, C, D & E in the Maximum characterization image represent the rocking curves of a single pixel and the maximum image in Figures 3.67, 3.74, 3.81 and 3.88 show the positions of these rocking curves. A is the rocking curve of the undamaged

crystal that is recorded far away from the extent of the strain field in the horizontal direction and its location is not shown in the images.

Tables 3.6, 3.7, 3.8 and 3.9 give the parameters recorded from the five rocking curves in each of the trials and Figures 3.69, 3.70, 3.76, 3.77, 3.83, 3.84, 3.90 and 3.91 show the comparisons of these different rocking curves. The shapes of the rocking curves and the FWHM values from the tables give an idea of the variation in rocking curves at different regions of the feature.

The characterization images from Figures 3.67, 3.68, 3.74, 3.75, 3.81, 3.82, 3.88 and 3.89 show the same consistent nature and extent of damage for each of the different crystal planes (h k l). Because the topographs and rocking curve characterization images are similar for the four 115- type reflections, we may infer that the damage in the crystal is largely at least 4-fold symmetric. The topographs form two sets mutually perpendicular to each other in azimuth. The topographs illustrate the difference in behavior in the diffraction plane (vertical direction) and perpendicular to the diffraction plane (horizontal direction).

3.6   Low Peak Fluence Nanosecond Laser Spot, 0.40 J/cm^2

The following section will deal with micrographs and topographs of a nanosecond laser spot irradiated with a peak fluence of 0.40 J/cm^2. Experiments were conducted on this spot in November 2003.

3.6.1   Optical Microscopy

Figure 3.92 shows a micrograph of the low fluence nanosecond laser spot irradiated with 100 pulses, peak fluence on the spot being 0.40 J/cm^2. The horizontal size of the spot or crater is 37 μm. The vertical size of the spot or crater is about 18 μm. Horizontal and vertical linescan across the center of the micrograph reveals the contrast in more detail. Figures 3.93 and 3.94 show horizontal and vertical linescans across the center of the irradiated spot on the micrograph. The spot has the same general shape as the high fluence nanosecond laser spot, and is not really radially symmetric. It is smaller due to the lower fluence.
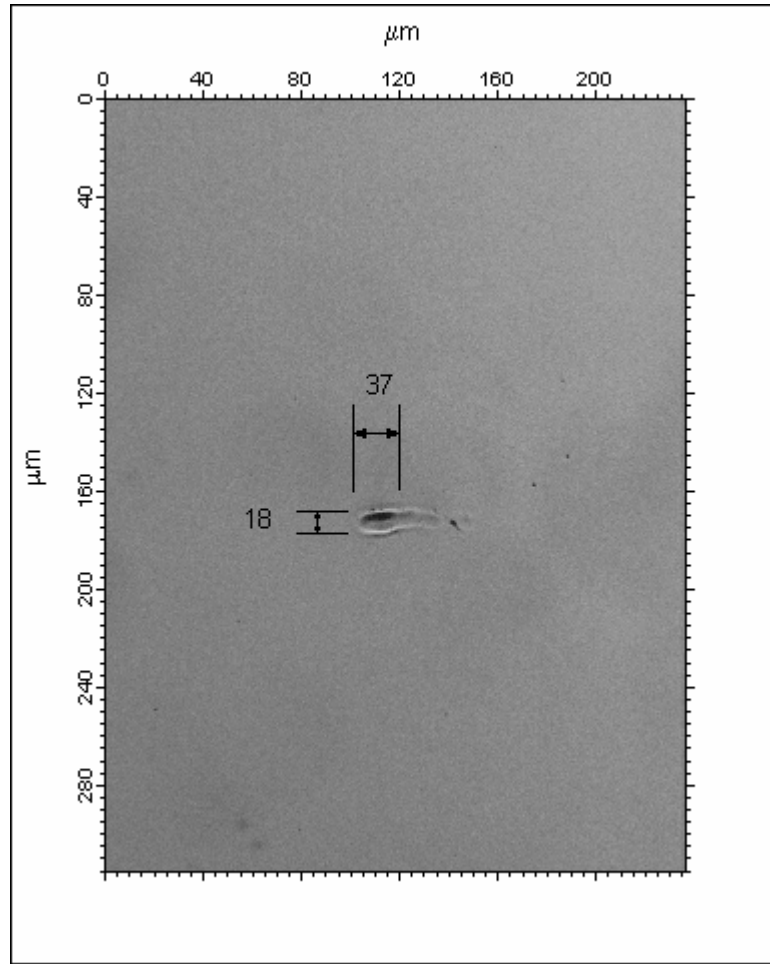
Figure 3.92. Micrograph showing feature size of low peak fluence (0.40 J/cm2) laser spot.
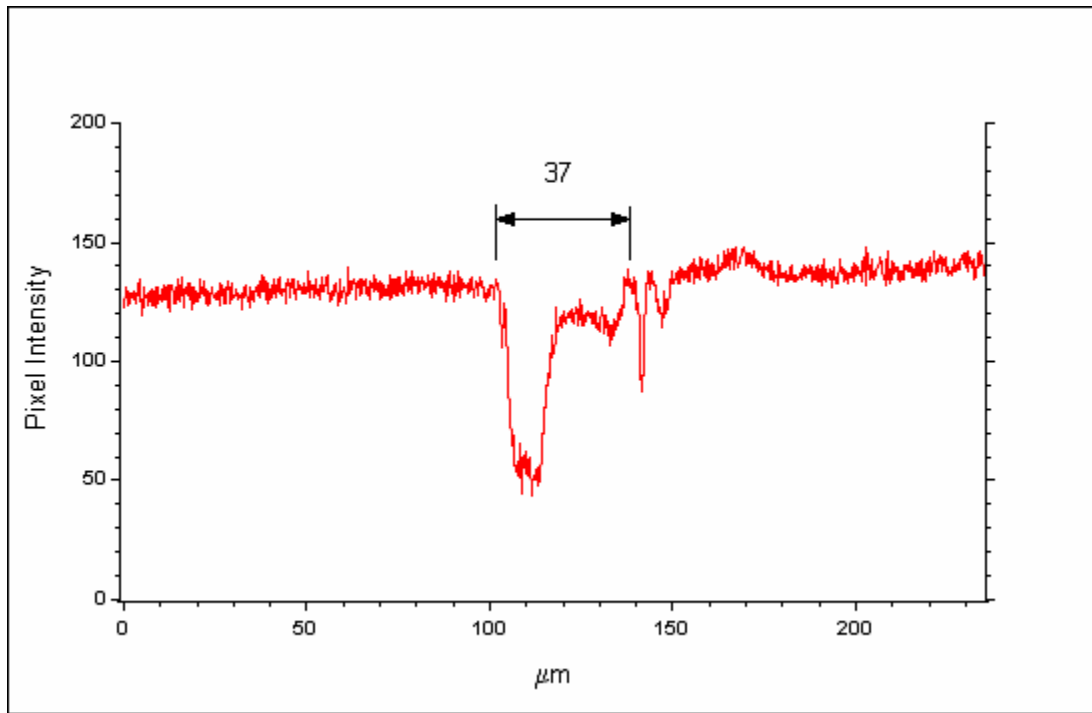
Figure 3.93. Horizontal linescan across micrograph of low peak fluence ns laser spot, showing feature size.
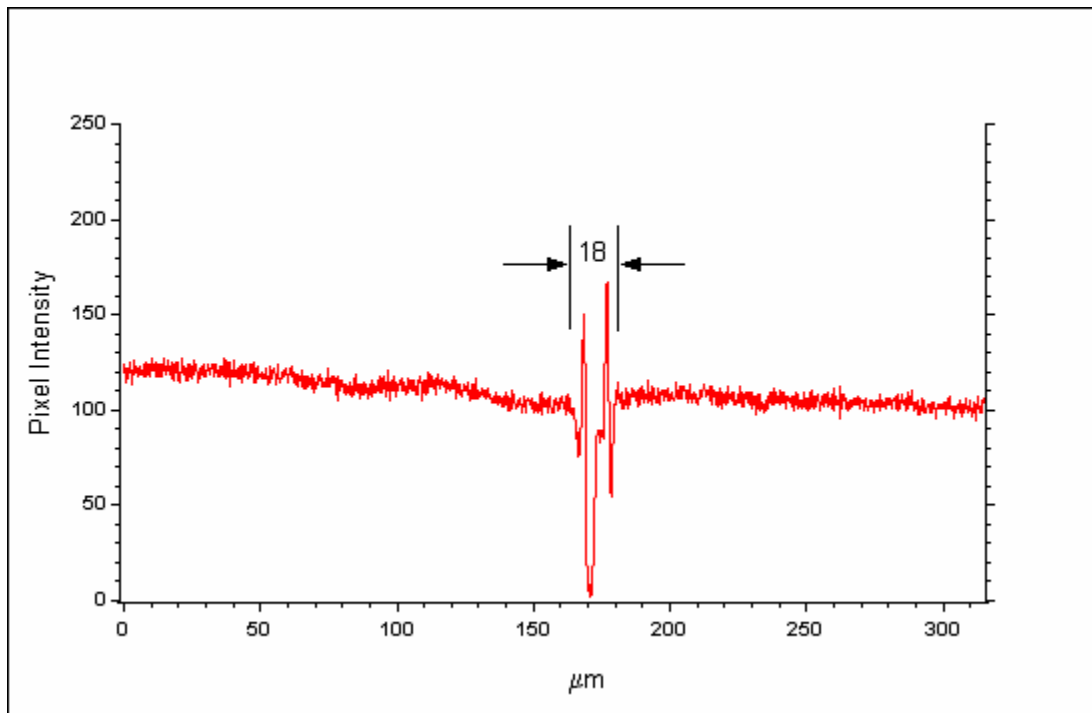
Figure 3.94. Vertical linescan across micrograph of low peak fluence ns laser spot, showing feature size.

3.6.2 Topography

The following section deals with the topographs of the low power nanosecond laser irradiated spot, with an h k l of 115. The topographs presented in this section were obtained during experimentation in November 2003 at the APS. The topographs in this section can be used effectively to draw damage comparisons with the high power nanosecond topographs taken in November 2003.

3.6.2.1 Slice Analysis

Figure 3.95 is an XY slice at the peak of the rocking curve. The XY slice is an image of the crystal diffracting at its Bragg peak, as seen by the CCD camera.
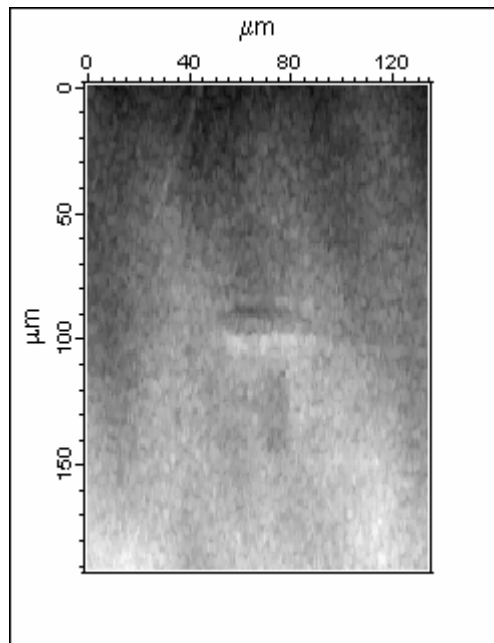
Figure 3.95. XY slice of low peak fluence ns laser spot 115 at the center of Bragg peak showing damage, as seen by the CCD camera.

Figure 3.96 shows the Xθ slice with adjusted intensity range showing the intensity variation in the horizontal direction. The Xθ slice is extracted approximately across the center of the feature at a Y coordinate of 96 μm of the XY slice. The superimposed red line across the image is the image line profile that shows the change in intensity along the horizontal direction across the feature at a θ value of 13.9295˚.

Figure 3.97 shows the Yθ slice with adjusted intensity range showing the intensity variation in the vertical direction. The Yθ slice is extracted at X coordinate of 67 μm of the XY slice.

From the linescans across the topographs in Figures 3.96 and 3.97 it can be seen that it is difficult to see the effects of the laser spot, which is barely visible in the topograph. All that is visible is low level noise across the topograph. This shows that the low power nanosecond laser damage is very small in the crystal as compared to the high power nanosecond laser damage.
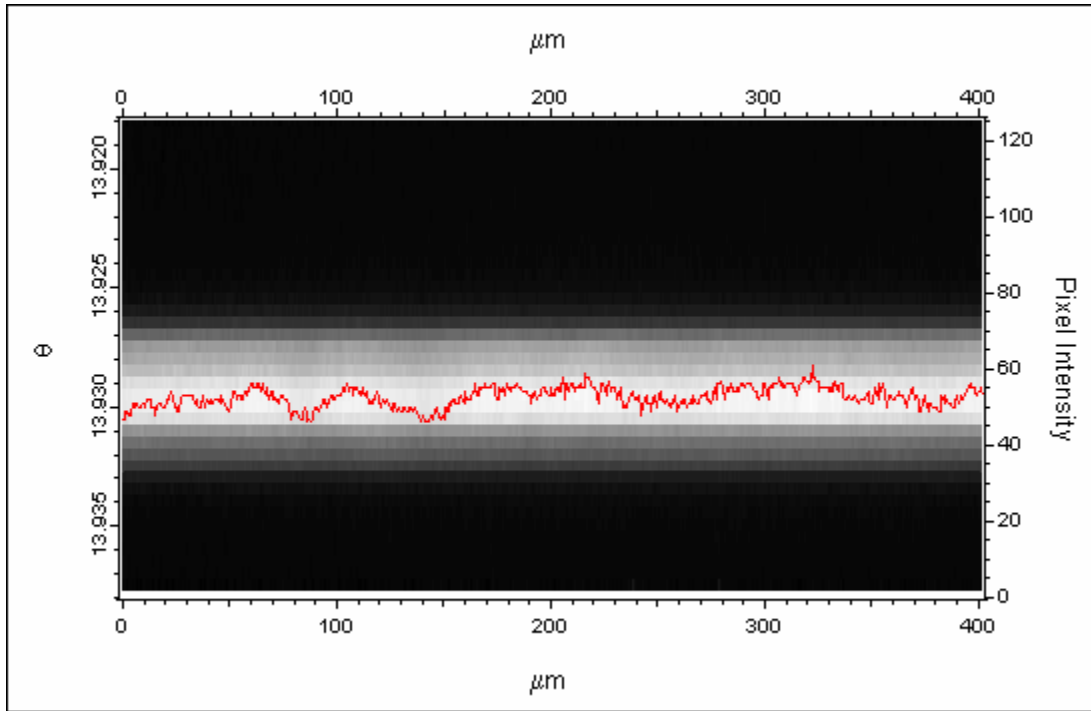
Figure 3.96. Xθ slice of low peak fluence ns laser spot 115 showing region of horizontal damage. The Xθ slice is taken at a Y value of 96 μm of the XY slice.
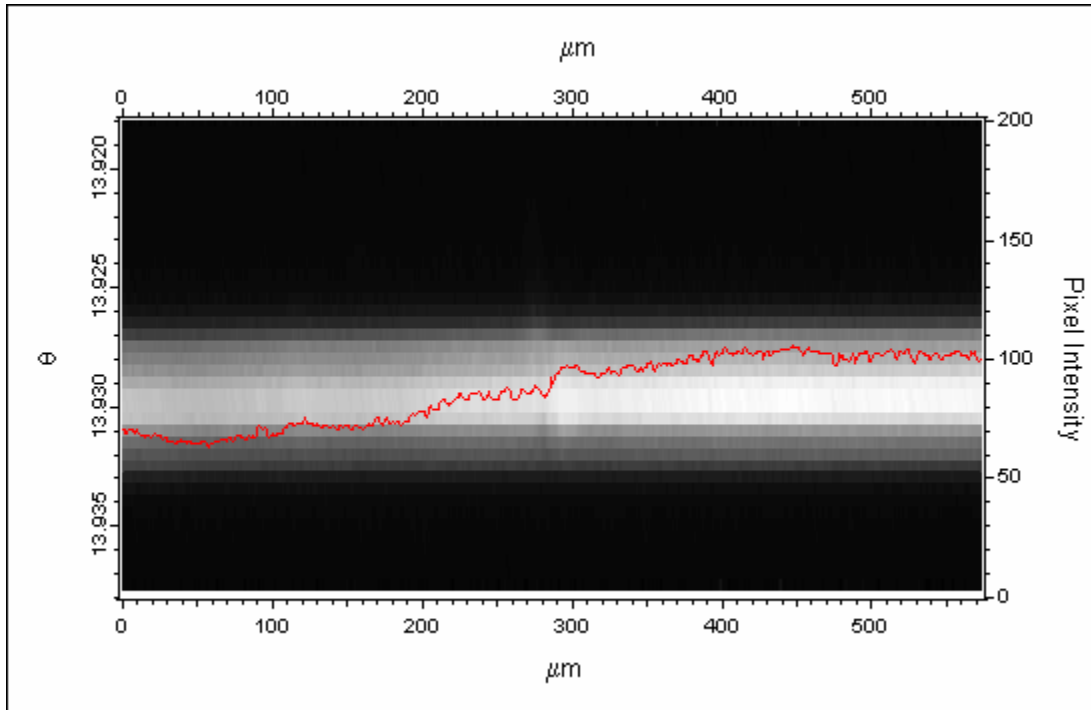
Figure 3.97. Yθ slice of low peak fluence ns laser spot 115 showing region of vertical damage. The Yθ slice is taken at an X value of 67 μm on the XY slice.

Figure 3.98 shows an Xθ slice extracted approximately across the center of the feature at a Y coordinate of 96 μm of the XY slice. The lines A, B, C & D are rocking curves of a single pixel in the vertical direction of the Xθ slice. A is the rocking curve of the undamaged crystal that is recorded at 10 μm on slice Xθ, far away from the damaged region in the horizontal direction. Figure 3.99 shows comparisons of the four different rocking curves and Table 3.11 gives the data recorded from the four rocking curves.
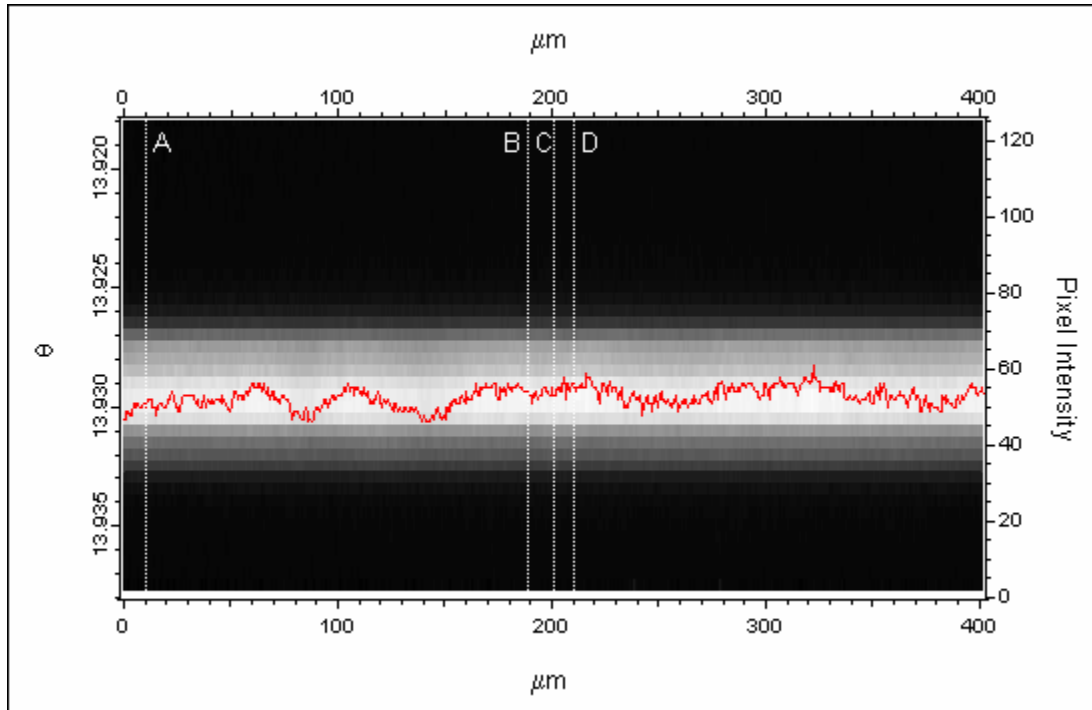
Figure 3.98. Xθ slice of low peak fluence ns laser spot 115 showing positions of rocking curves A, B, C & D. The Xθ slice is taken at a Y value of 96 μm of the XY slice.
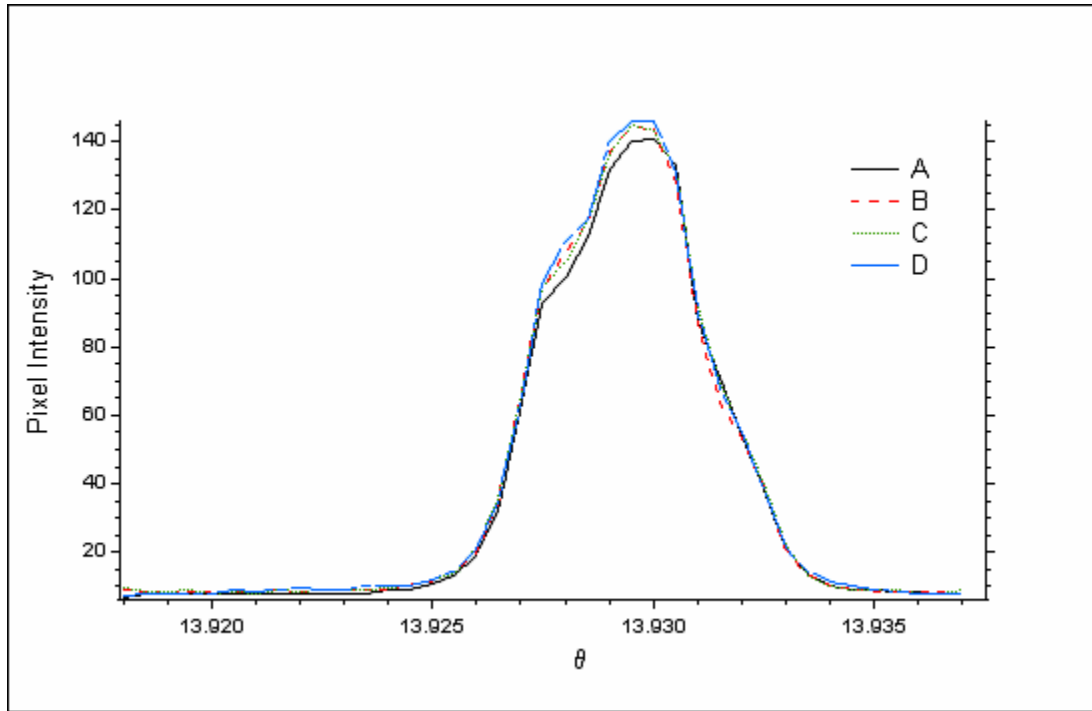
Figure 3.99. Comparison of rocking curves A, B, C & D of low peak fluence ns laser spot 115 .

Table 3.11. Rocking curve details of low peak fluence ns laser spot 115 .

Rocking Curve	Rocking Curve Position (μm)	Peak Intensity	Background Intensity	FWHM (arc sec)	FWHM (Curve) / FWHM (A)
A	10	140.9	6.65	15.19	1.00
B	189	144.4	8.00	14.59	0.96
C	201	144.8	8.00	14.97	0.99
D	210	146.0	7.50	14.77	0.97

It can be seen in Table 3.11 and in Figure 3.99 the FWHM of all the rocking curves B, C & D are almost the same as that of the rocking curve, A, of the undamaged crystal. Hence, the rocking curves support the conclusion that the low fluence nanosecond laser introduces very little damage to the crystal.

The characterization images in Figures 3.100 and 3.101 also show very little damage as compared to the high power femtosecond laser spot. The laser spot can,

however be identified in all of them except the Maximum Location and 4th Moment images. The human eye is sensitive and can pick out these small differences and identify the laser spot region.

3.6.2.2 Image Analysis on Rocking Curve Characterizations
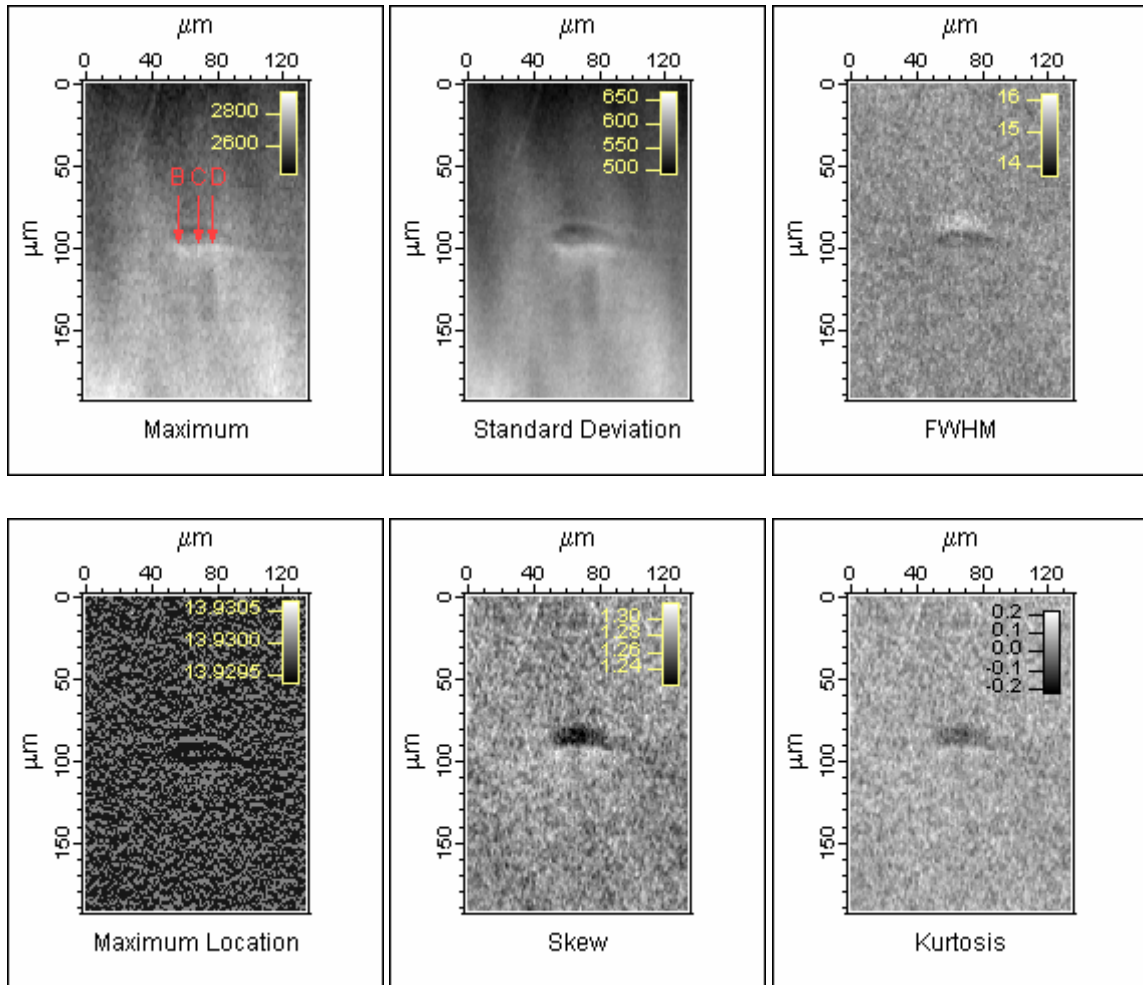
Figure 3.100. Low peak fluence ns laser spot 115 images showing characterizations Maximum, Standard Deviation, FWHM, Maximum Location, Skew & Kurtosis. The maximum image shows the location of the rocking curves, at the arrow head.
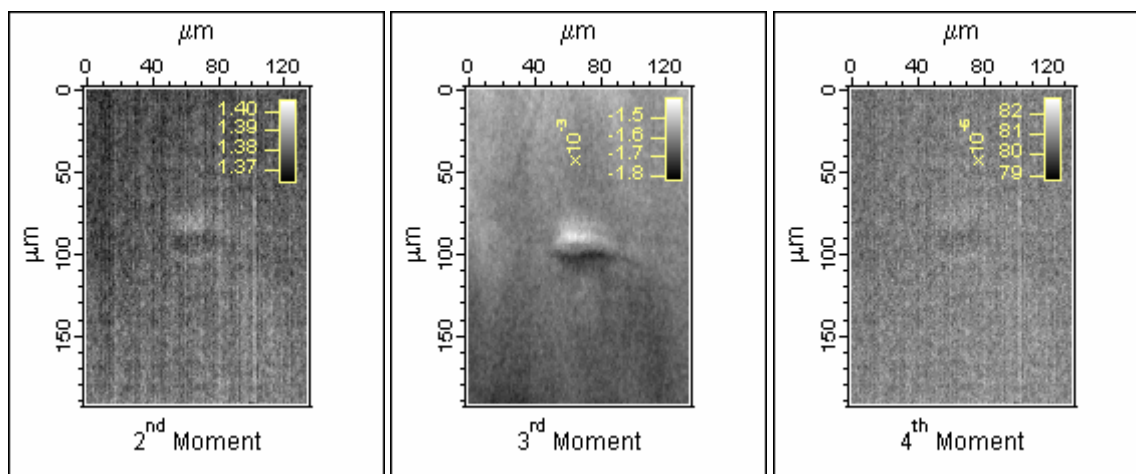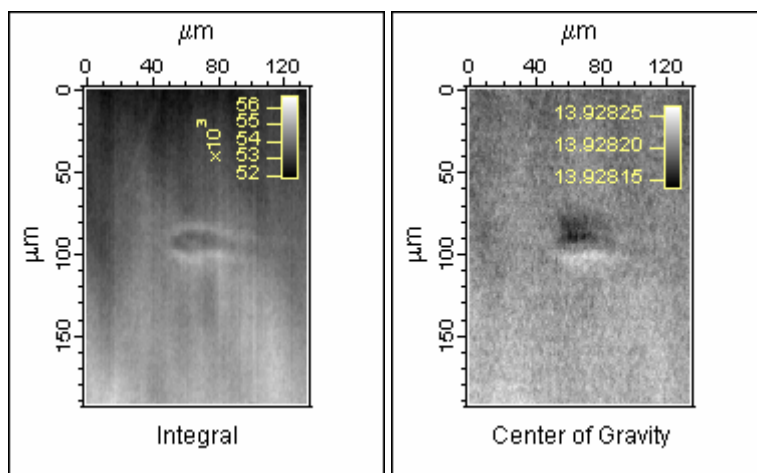
Figure 3.101. Low peak fluence ns laser spot 115 images showing moments Integral and Center of Gravity, 2nd, 3rd & 4th Moment about the Center of Gravity.

3.7   PHASE DESTROYER

To eliminate any speculations that the contrast in images on the topographs were due to phase contrast, an experiment was conducted. Two sets of data were obtained, one with a phase destroyer and one without. The phase destroyer was custom made at the APS during the experimental time. It's a circular disc made with four circular sheets of paper. This disc can be rotated about its center with a stepping motor. The purpose of the phase destroyer is to eliminate the partial coherency in the synchrotron beam. This coherency has been found to be useful in providing enhanced contrast in radiographs taken at the APS. The incident x-ray beam passes through the spinning paper whose fibrous nature gives different optical path lengths for different portions of the beam to pass through. Spinning will eliminate images of the paper fibers from forming in the integration time of data collection. Figure 3.102 shows an image of the phase destroyer.
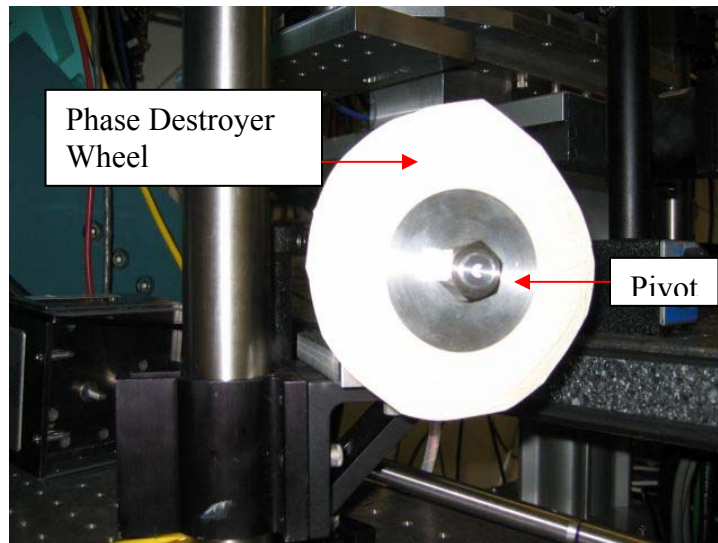
Figure 3.102. Phase destroyer wheel

A test was conducted to see the functionality of the phase destroyer. Packing foam was used as a specimen to test the phase destroyer. Radiographic images were taken in transmission with and without the phase destroyer and were analyzed for phase contrast. Figure 3.103 shows radiographs of the packing foam with and without the phase destroyer. It can be seen that the radiograph without the phase destroyer shows distinct boundaries on the features due to the presence of phase contrast. The topograph with the phase destroyer in place does not show the bright contrast on the boundaries of the features and hence confirms that the phase destroyer does indeed eliminate the partial coherency in the beam.
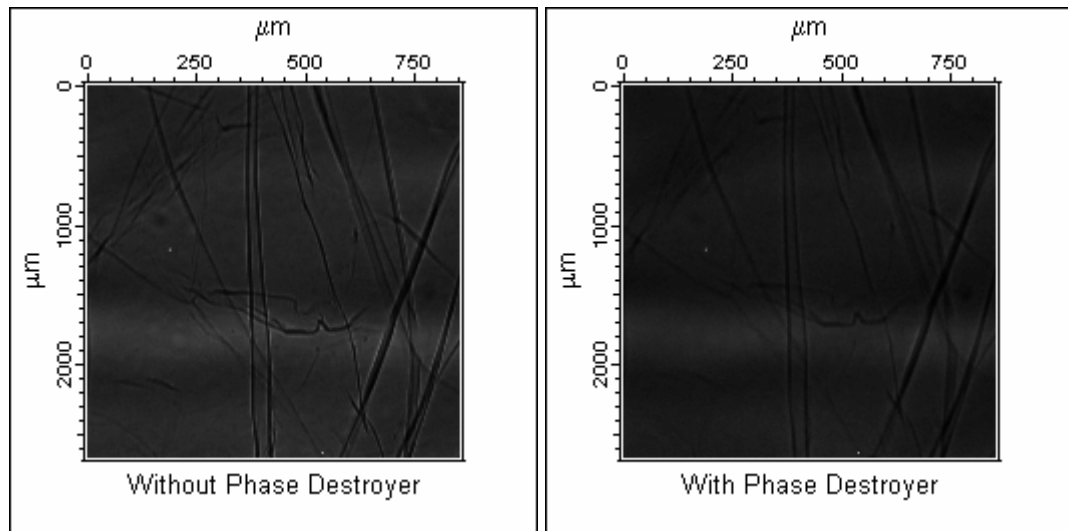
Figure 3.103. CCD camera images of packing foam with and without the phase destroyer.

A second test was conducted on the low peak fluence femtosecond laser spot. For one set of data, this phase destroyer was placed in the path of the x-ray beam before the beam was incident on the specimen. The specimen was rocked using this beam and data was recorded. In the other set of data, the phase destroyer was removed. Figures 3.104

shows the images at Bragg peak of the low peak fluence femtosecond spot, with and without the phase destroyer.
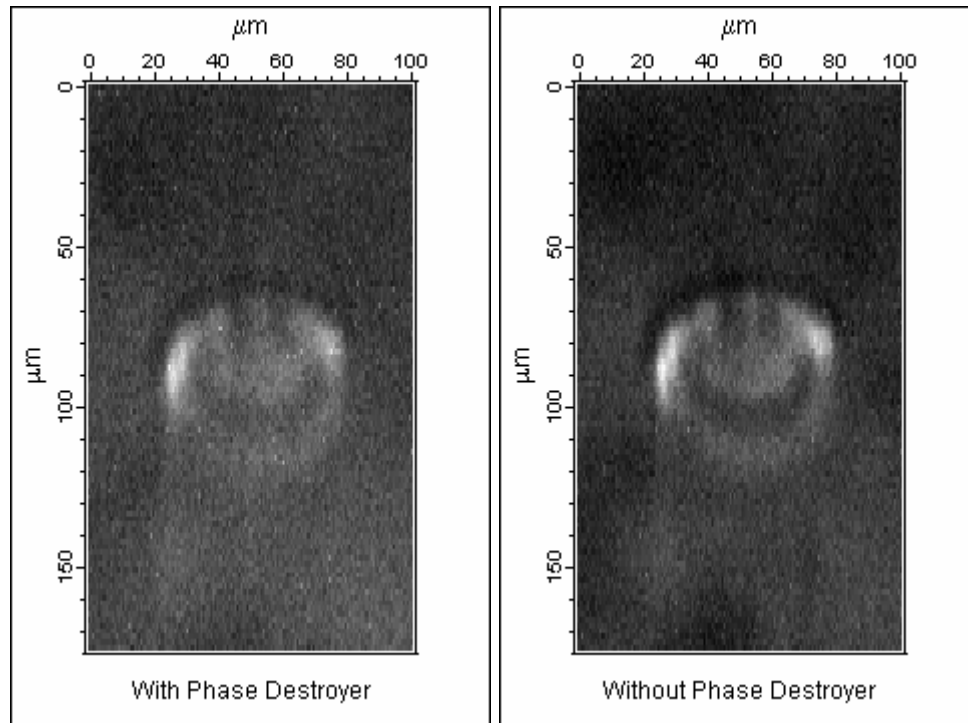
Figure 3.104. Low peak fluence fs spot images with and without phase destroyer as see by the CCD camera.

It can be seen that both the topographs of the low fluence femtosecond laser spot show the same features formation with the same intensity, hence confirming the fact that the contrast in the topographs is not due to phase contrast.

CHAPTER 4

SUMMARY OF RESULTS & CONCLUSIONS

From the results chapter it can be clearly seen that x-ray diffraction and x-ray topography is a very useful method to analyze and characterize laser irradiated damage to a silicon crystal. It can be helpful in determining the extent and nature of the damage produced in the crystal. Table 4.1 summarizes the observed feature sizes in this study.

Table 4.1. Summary of Results

Laser Spot	Peak Fluence (J/cm^2)	h k l	Micrograph Feature Size (μm)		Topograph Linescan Feature Size (μm)	
			Horizontal	Vertical	Horizontal	Vertical
April ' 04						
Femtosecond High Peak Fluence	4.83	0 0 4	68	62	189	416
Femtosecond Low Peak Fluence	0.63	0 0 4	70	72	59	58
Nov ' 03						
Femtosecond High Peak Fluence	4.83	$\bar{1}\bar{1}5$	68	62	154	288
Femtosecond Low Peak Fluence	0.63	0 0 4	70	72	61	55
Nov '03						
Nanosecond High Peak Fluence	4.71	115	76	40	128	149
		$1\bar{1}5$			123	152
		$\bar{1}\bar{1}5$			119	148
		$\bar{1}15$			121	145
Nanosecond Low Peak Fluence	0.40	115	37	18	-	-

The conclusions from this study are as follows.

- X-ray topography proved to be a useful method for observing damage introduced by laser irradiation. The dimensional extent of the damaged on the surface can be quantified and may provide valuable experimental observations for comparisons to computational models of the laser irradiation process. Further work on modeling the dynamical diffraction process and tying topographs to structural models of the material are needed, but the method should provide good insight into the nature of the damage caused to crystals by laser irradiation.

- High peak fluence femtosecond (4.83 J/cm^2) and high peak fluence nanosecond (4.71 J/cm^2) laser irradiation of a silicon crystal introduces damage to the crystal lattice well beyond the area ablated and thus visible. Thermo-elastic calculations of ultrashort laser pulses by Chen and Tzou [Chen et al., 2002 a, b.] have shown that a stress wave is generated which propagates through the material. One speculation would be that this stress wave could propagate damage into the material out beyond the region irradiated by, for example, nucleating dislocations.

- Low peak fluence femtosecond (0.63 J/cm^2) and low peak fluence nanosecond (0.40 J/cm^2) laser irradiation on a silicon crystal introduces little to no damage to the crystal lattice, certainly none outside the area where material was ablated. Comparing the high and low fluence results imply that there is a threshold level of fluence for propagation of damage outside the ablated region. Since the high and low fluence irradiations in this study differed by an order of magnitude, the threshold value cannot be determined precisely.

- The dimensional extent of damage measured with different reflections was the same for different 115 type reflections but differed between the 115 and 004 reflections. For the high fluence femtosecond laser spot, the extent of damage seen in the diffraction plane (vertically) was approximately 416 μm for the 004 reflection compared to 288 μm for the 115 reflection. The extent of damage seen horizontally was approximately 189 μm for the 004 reflection compared to 154 μm for the 115 reflection. Such observations may be useful in determining the exact nature of the damage introduced (for example, determining the Burgers vectors of dislocations).

- High fluence (4.83 J/ cm^2) femtosecond laser irradiation on a silicon crystal introduces damage to a greater dimensional extent than a nanosecond laser with nearly the same peak fluence (4.71 J/ cm^2). In the laser spots studies here, nearly the same energy density was delivered to the crystal over 500,000 times faster with the femtosecond laser pulses which should result in quite different damage mechanisms.

- With the electronic x-ray camera an enormous number of rocking curves can be collected from a specimen each originating from a different location on the specimen. These rocking curves can be characterized in various ways. Again, further work on structural models of the damage in the material and the dynamical diffraction process is needed. Care must be taken in interpreting the rocking curves. The diffracted rays do not have to be parallel and they may move to different pixels in different locations. The true resolution of the measurement system will not be given by the size of the pixels but will be somewhat larger than this. Errors of this type may be minimized by keeping the x-ray camera close or by inserting an analyzer crystal on the diffracted beam side.

APPENDIX A

IMAGE SHIFT CALCULATIONS

A1.1   Derivation for Image Shift

The following presents a derivation of the shifting of images on the detector as rocking curves are taken. It is assumed that all the incident and diffracted rays are parallel in the image. This does not have to be true as regions of interest with lattice rotations will cause a shift in the diffraction angle. This derivation is useful; however, in understanding the magnitude of the corrections is the starting place for further corrections. Figure A1.1 shows a schematic of the image shifting process in a scan.

In the following derivation, the following result on the point of intersection of two lines will prove useful.

Point of Intersection of Two Lines:

$$y - y_1 = m_1(x - x_1). \tag{A1.1}$$

Line A in point-slope form

$$y - y_2 = m_2(x - x_2). \tag{A1.2}$$

Line B in point-slope form

Point of intersection is given by (x,y). Setting y from the two equations equal gives

$$m_1(x - x_1) + y_1 = m_2(x - x_2) + y_2. \tag{A1.3}$$

or

$$x = \frac{m_1 x_1 - m_2 x_2 - y_1 + y_2}{m_1 - m_2}. \tag{A1.4}$$

Once x is determined from this equation y can be determined from

$$y = y_1 + m_1(x - x_1).$$

(A1.5)
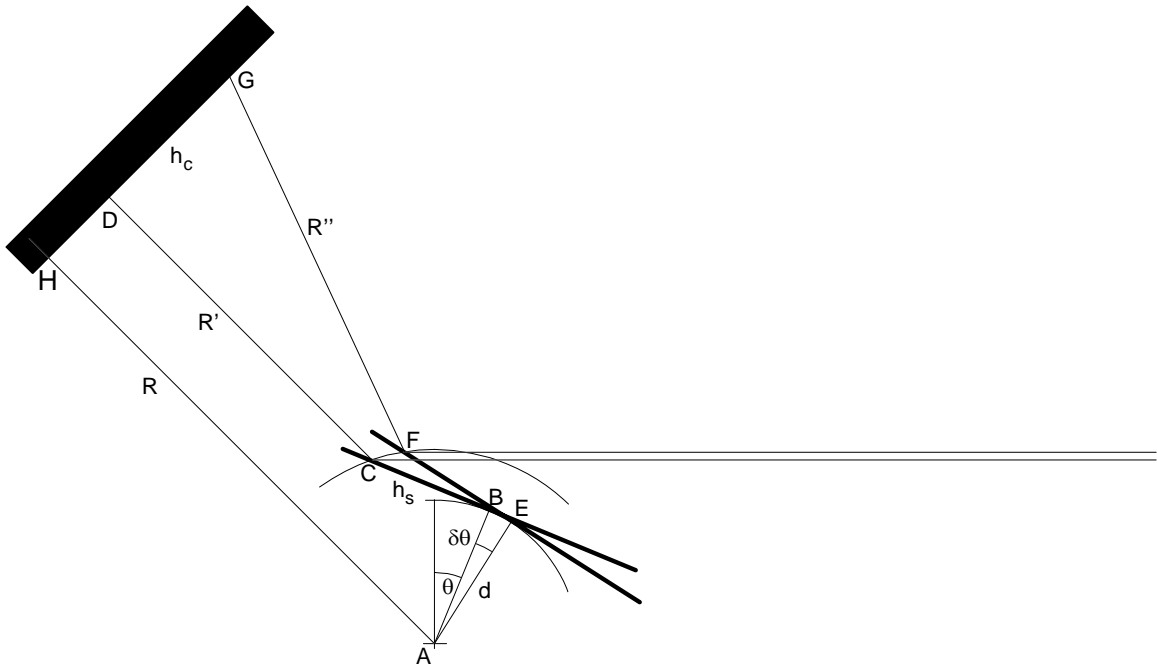
Figure A1.1. Image shifting process in a scan

Point A is the center of rotation of the θ axis. The sample rotates about this axis in a θ scan. An x-ray camera, HG, is located a distance R from the center of rotation. Point C is an identifiable point on the surface of the specimen. In a topograph, point C is imaged on the x-ray camera at point D. Point B is the point on the sample surface directly above (below) the center of rotation along the normal to the surface. Through a θ scan, the sample rotates. As the sample rotates from θ to θ+δθ, the point B moves to point E and point C moves to point F. On the x-ray camera, the image point D moves to point G.

The depth below the surface of the specimen that the center of rotation is located

is d. If the center of rotation is above the surface then d is negative. The distance

coordinate in the surface of the specimen is h_s. The origin of h_s is directly above (below)

the center of rotation. The distance from the specimen to the x-ray camera is R. The

shift of a feature at point D on the topograph due to a rotation of $\delta\theta$ is h_c.

$\overline{AB} = \overline{AE} = d$ Distance to the center of rotation from the specimen surface

$\overline{BC} = \overline{EF} = h_s$ Height coordinate on the specimen

$\overline{CD} = \overline{FG} = R$ Camera radius

$\overline{DG} = h_c$ Height coordinate on the camera

With the coordinate system origin at the center of rotation (Point A), Point B is at

$$(x_B, y_B) = (d\sin\theta, d\cos\theta).$$ (A1.6)

Point C is at

$$(x_C, y_C) = (d\sin\theta - h_s\cos\theta, d\cos\theta + h_s\sin\theta).$$ (A1.7)

Point E is at

$$(x_E, y_E) = (d\sin(\theta + \delta\theta), d\cos(\theta + \delta\theta)).$$ (A1.8)

Point F is at

$$(x_F, y_F) = (d\sin(\theta + \delta\theta) - h_s\cos(\theta + \delta\theta), d\cos(\theta + \delta\theta) + h_s\sin(\theta + \delta\theta)).$$ (A1.9)

Point H is at

$$(x_H, y_H) = (-R\cos 2\theta, R\sin 2\theta).$$ (A1.10)

The line containing $\overline{AH}$ is given by

$$y = \frac{-\sin 2\theta}{\cos 2\theta} x.$$
(A1.11)

Which has a slope

$$m_{AH} = \frac{-\sin 2\theta}{\cos 2\theta}.$$
(A1.12)

The line containing $\overline{HG}$ has a slope given by the negative inverse of the slope of this line because it is perpendicular to it and it is in the plane of the x-ray camera. The equation of the line, in point-slope form, containing $\overline{HG}$ is

$$(y - R \sin 2\theta) = \frac{\cos 2\theta}{\sin 2\theta}(x + R \cos 2\theta).$$
(A1.13)

The equation of the line containing $\overline{CD}$ is

$$(y - d\cos\theta - h_s \sin\theta) = \frac{-\sin 2\theta}{\cos 2\theta}(x - d\sin\theta + h_s \cos\theta).$$
(A1.14)

The equation of the line containing $\overline{FG}$ is

$$(y - d\cos(\theta + \delta\theta) - h_s \sin(\theta + \delta\theta)) = \frac{-\sin(2\theta + 2\delta\theta)}{\cos(2\theta + 2\delta\theta)}(x - d\sin(\theta + \delta\theta) + h_s \cos(\theta + \delta\theta))$$

(A1.15)

Point D is at the intersection of the lines containing $\overline{CD}$ and $\overline{HG}$. Its x-coordinate is

$$x_D = \frac{m_{HG}x_H - m_{CD}x_C - y_H + y_C}{m_{HG} - m_{CD}}$$
(A1.16)

where the slopes of the lines are given by

$$m_{HG} = \frac{\cos 2\theta}{\sin 2\theta}.$$
(A1.17)

$$m_{CD} = \frac{-\sin 2\theta}{\cos 2\theta}.$$
(A1.18)

The y-coordinate for point D is

$$y_D = y_H + m_{HG}(x_D - x_H).$$
(A1.19)

Point G is the intersection of the lines containing $\overline{FG}$ and $\overline{HG}$ and has coordinates

$$x_G = \frac{m_{HG}x_H - m_{FG}x_F - y_H + y_F}{m_{HG} - m_{FG}}.$$
(A1.20)

$$y_G = y_H + m_{HG}(x_G - x_H).$$
(A1.21)

where the slope of the line containing $\overline{FG}$ is

$$m_{FG} = \frac{-\sin(2\theta + 2\delta\theta)}{\cos(2\theta + 2\delta\theta)}.$$
(A1.22)

A1.2 Image Shift Calculation Data Tables and Figures.

For values of d = 10 μm (an estimate), R = 47 mm, and a rocking angle range of 0.06˚, Table A1.1 shows the calculated shift in DG for values of h_s = -100 μm, 0 μm and 100 μm and the approximation calculation for shift $R\delta 2\theta$.

Table A1.1. Calculated valued for image shift on the detector.

$\delta\theta$ (degrees)	Calculated DG at h_s= 0 μm (μm)	Calculated DG at h_s = -100 μm (μm)	Calculated DG at h_s = 100 μm (μm)	Calculated$R\delta 2\theta$ (for comparison) (μm)
-0.0300	-46.07470	-46.12307	-46.02634	-46.07669
-0.0275	-42.23514	-42.27948	-42.19080	-42.23697
-0.0250	-38.39558	-38.43589	-38.35527	-38.39724
-0.0225	-34.55602	-34.59230	-34.51974	-34.55752
-0.0200	-30.71646	-30.74871	-30.68421	-30.71779
-0.0175	-26.87691	-26.90512	-26.84869	-26.87807
-0.0150	-23.03735	-23.06153	-23.01316	-23.03835
-0.0125	-19.19779	-19.21795	-19.17763	-19.19862
-0.0100	-15.35823	-15.37436	-15.34210	-15.35890
-0.0075	-11.51867	-11.53077	-11.50658	-11.51917
-0.0050	-7.67912	-7.68718	-7.67105	-7.67945
-0.0025	-3.83956	-3.84359	-3.83553	-3.83972
0.0000	0.00000	0.00000	0.00000	0.00000
0.0025	3.83956	3.84359	3.83553	3.83972
0.0050	7.67912	7.68718	7.67105	7.67945
0.0075	11.51867	11.53077	11.50658	11.51917
0.0100	15.35823	15.37436	15.34210	15.35890
0.0125	19.19779	19.21795	19.17763	19.19862
0.0150	23.03735	23.06154	23.01315	23.03835
0.0175	26.87691	26.90514	26.84868	26.87807
0.0200	30.71647	30.74873	30.68420	30.71779
0.0225	34.55603	34.59232	34.51973	34.55752
0.0250	38.39559	38.43592	38.35526	38.39724
0.0275	42.23515	42.27951	42.19078	42.23697
0.0300	46.07471	46.12311	46.02631	46.07669

For values of d = 10 μm (an estimate), R = 47 mm, and a rocking angle range of 0.06˚, Table A1.2 and Figure A1.2 shows how good an approximation Rδ2θ is for the image shift on the detector in comparison with calculated shift of DG for values of h_s = -100 μm, 0 μm and 100 μm.

Table A1.2. Difference in calculated values of image shift and approximated Rδ2θ values.

δθ (degrees)	Calculated DG(h_s=-100)-2Rδθ (μm)	Calculated DG(h_s=0)-R2δθ (μm)	Calculated DG(h_s= +100)-R2δθ (μm)
-0.0300	-0.046379991	0.001988320	0.050356631
-0.0275	-0.042514014	0.001824802	0.046163618
-0.0250	-0.038648409	0.001660694	0.041969797
-0.0225	-0.034783119	0.001496054	0.037775226
-0.0200	-0.030918085	0.001330940	0.033579965
-0.0175	-0.027053248	0.001165411	0.029384070
-0.0150	-0.023188551	0.000999526	0.025187602
-0.0125	-0.019323933	0.000833342	0.020990617
-0.0100	-0.015459337	0.000666919	0.016793175
-0.0075	-0.011594705	0.000500315	0.012595334
-0.0050	-0.007729977	0.000333588	0.008397152
-0.0025	-0.003865095	0.000166797	0.004198688
0.0000	0.000000000	0.000000000	0.000000000
0.0025	0.003865366	-0.000166744	-0.004198854
0.0050	0.007731061	-0.000333377	-0.008397814
0.0075	0.011597144	-0.000499840	-0.012596824
0.0100	0.015463675	-0.000666074	-0.016795824
0.0125	0.019330710	-0.000832023	-0.020994756
0.0150	0.023198310	-0.000997626	-0.025193561
0.0175	0.027066532	-0.001162825	-0.029392181
0.0200	0.030935435	-0.001327562	-0.033590559
0.0225	0.034805078	-0.001491778	-0.037788635
0.0250	0.038675519	-0.001655416	-0.041986350
0.0275	0.042546816	-0.001818416	-0.046183647
0.0300	0.046419029	-0.001980720	-0.050380468
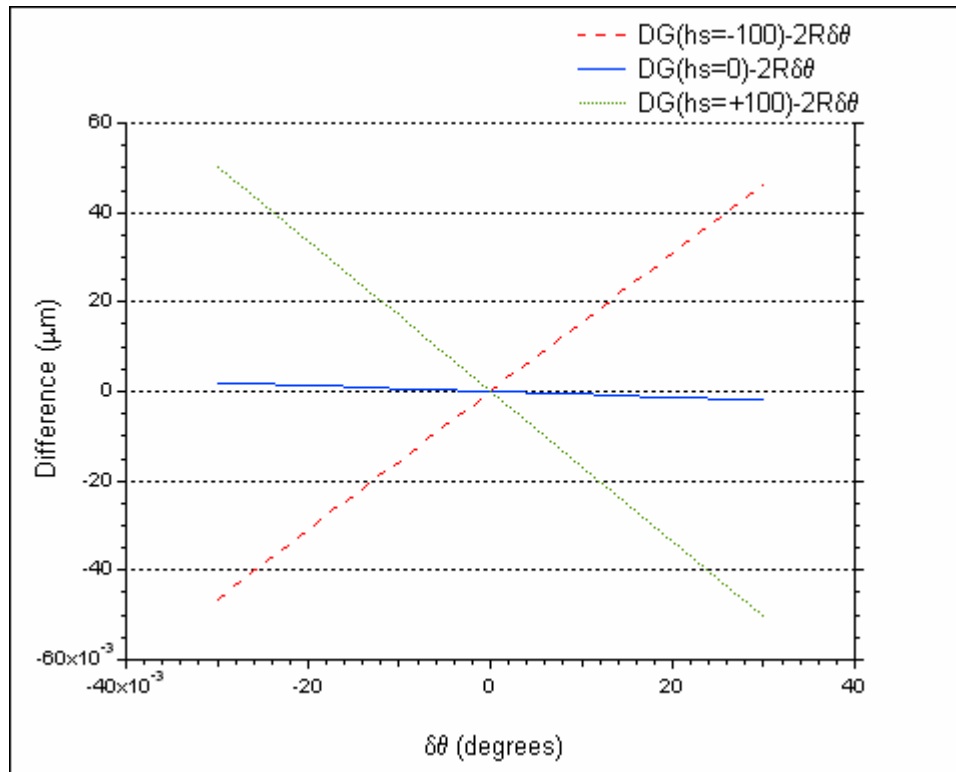
Figure A1.2. Difference between Rδ2θ and a more exact calculation showing how good an approximation Rδ2θ is for the image shift on the detector.

A1.3 Change in Beam Footprint

Table A1.2 shows the change in feature size over a rocking angle range of $0.06°$. The parameter that is kept constant is the camera radius of 47 mm. The values of h_s are kept the same for different trials with varying values of d.

Table A1.3. Change in feature footprint values for different values of d.

d (μm)	θ (°)	h_S Top/Bottom of Feature (μm)	x_D (μm)	y_D (μm)	Distance Moved by Top of Feature (μm)	Distance Moved by Bottom of Feature (μm)	δ Feature Size (μm)
0	22.412	25	31214.84191	31010.21986	92.12917	92.17757	0.04839
		-25	31201.40366	31023.74092			
	22.472	25	31149.84293	31075.51088			
		-25	31136.34221	31089.03802			
5	22.412	25	31211.58348	31013.49836	92.12717	92.17557	0.04840
		-25	31198.14523	31027.01942			
	22.472	25	31146.57906	31078.78114			
		-25	31133.07834	31092.30828			
10	22.412	25	31208.32506	31016.77687	92.12517	92.17358	0.04840
		-25	31194.88681	31030.29793			
	22.472	25	31143.31519	31082.05140			
		-25	31129.81446	31095.57854			

Table A1.4 shows the change in feature size over a rocking angle range of $0.06°$. The parameters that are kept constant are the camera radius of 47 mm. The values of d are kept constant with varying values of h_s.

Table A1.4. Change in feature footprint values for different values of h_s.

d (μm)	θ (°)	h_S Top/ Bottom of Feature (μm)	x_D (μm)	y_D (μm)	Distance Moved by Top of Feature (μm)	Distance Moved by Bottom of Feature (μm)	δ Feature Size (μm)
10	22.412	50	31215.04418	31010.01634	92.10098	92.14937	0.04839
		0	31201.60593	31023.53740			
	22.472	50	31150.06555	31075.28783			
		0	31136.56483	31088.81497			
10	22.412	0	31201.60593	31023.53740	92.14937	92.19778	0.04841
		-50	31188.16768	31037.05846			
	22.472	0	31136.56483	31088.81497			
		-50	-31123.0641	31102.34211			
10	22.412	75	-31221.7633	31003.25581	92.07679	92.12517	0.04839
		25	31208.32506	31016.77687			
	22.472	75	31156.81591	31068.52426			
		25	31143.31519	31082.05140			

It can be seen from Tables A1.2 and A1.3 that the change in feature footprint size is approximately 0.049 μm, over a rocking angle range of $0.06°$. This change in feature footprint size is very small (less than 1/10 of a pixel) and has not been corrected for.

APPENDIX B

IGOR OPERATIONS

This section deals with the use of Igor and some of the data processing steps used in this study. The following were the sequence of steps followed to analyze the raw 16-bit TIFF data that was recorded during experimentation at the APS in November 2003 and April 2004.

- All the raw 16-bit TIFF images from a scan are stored in unique folders. The first step is to assemble all these individual images as a stack or 3 dimensional data structure. A user procedure (program) was written to do this operation. A user procedure is a program written by the user to do specific tasks. All the user procedures are stored in the path C:\ Program Files\ WaveMetrics\ Igor Pro Folder \User Procedures.

- The user procedure "loadimagefile5.8.1b" is loaded from the menu File/ OpenFile/ Procedure. A window pops up and the "loadimagefile5.8.1b" is loaded. The "loadimagefile5.8.1b" file has a number of macros (sub program tools) which load upon compilation. The important macros in "loadimagefile5.8.1b" are "Build_StackMakerPanel" and "BuildChunk2Plane_Graph".

- The "Build_StackMakerPanel" is used to make 3 dimensional stacks from the raw images. It can be loaded from the menu Macros/ Build_StackMakerPanel. A pop-up window opens and the raw 16-bit tiff images can be loaded using the button "Find Image Folders". Select the folder containing all the raw data folders. In the panel window, highlight the data folders (folders containing a sequence of images). The output folder for the stacks can be chosen using the button "Select Output Folder".

The stacks are made by pressing the button "Make Stacks". The stacks are saved as igor binary wave (.ibw) files.

- The stacks are then loaded in the experiment using the menu Data/ Load Waves/ Load Igor Binary… and then chosing the path where the stack is located. All loaded files and variables in an experiment can be accessed using the "Data Browser" in the Data menu.

- The loaded stacks can be viewed using the macro "BuildChunk2Plane_Graph" and choosing the desired stack from the drop down menu. All the frames in a stack can be browsed through using the frame button at the top of this macro. Any desired frame can also be extracted as an individual image using the button "Extract".

- To make generate a rocking curve from a region of interest open the macro "BuildChunk2Plane_Graph" and select the desired stack from the drop down menu. Go to the first frame in the stack and then click on the "ROI" button. A ROI window pops up. Click on "Start ROI Draw" and then draw a region of interest with the mouse. When done click on "Finish ROI". Click on the "Rocking Curve" button and then press the "Start" button. The program processes the request and then creates the rocking curve variable in the data browser.

- For the image shift correction operation, the "TThShiftStack" user procedure was loaded. Once this procedure is compiled, it is executed from the command window by the command

$$TThShiftStack(InStack,Radius,ThetaStep,PixSize)$$

where 'InStack' is the name of the stack to be corrected, 'Radius' is the camera radius for that set of collected data (47 mm for all our data), 'ThetaStep' is the unit step

increase in rocking angle or the angle between successive images (mostly 0.00025˚ for most of our data) and 'PixSize' is the resolution of each pixel (0.67 μm for all our data). The Radius and PixSize must have the same units.

- The 3 dimensional stacks were then cropped to focus mainly on the feature. The coordinates of the region to be focused on are noted, the coordinates being x1, y1, x2 and y2. Where x1 is where the region of focus starts on the x-axis and x2 is where the region of focus ends on the x-axis and similarly with the y-axis. The coordinates noted must be pixel values. The stack is ten cropped using the following command.

Duplicate/R = [x1,x2][y1,y2] "Source Stack Name" "Destination Stack Name"

- The 3 dimensional data structures were then filtered using a 3 dimensional, 3 x 3 x 3 median filter to remove shot noise from the images. This was done using the following command.

ImageFilter/ N /O median3d "Stack name"

- To make the characterization images from a stack the user procedures "FindMoments", "MomentsImages" and "MakeStatsImages" are loaded and compiled. To make the characterization images Kurtosis, Skew, Standard Deviation, FWHM, Maximum Location, Average and Maximum the following command was used:

MakeStatsImages(a)

where 'a' is the stack for which the characterization images are being generated.

- To make the moments images Integral, Center of Gravity, 1st, 2nd and 3rd moment about the center of gravity, the following command was used:

MomentsImages(a,start,step)

where 'a' is the stack for which the characterization images are being generated, 'start' is the start rocking angle for that particular scan and 'step' is the step size of rocking angle for the scan.

- To extract a rocking curve of a pixel, note down the x and y coordinate of the pixel. A rocking curve of the pixel can be extracted using the command

$$rock[]=a[x][y][p]$$

A rocking for that pixel is extracted in the variable rock in the data browser.

- Some analysis required conversion of the 16-bit stacks to 8-bit stacks. The 8-bit conversion was a requirement of the software such that they could be analyzed using the Graphical Slicer. The stack had to be normalized to 256 colors first and then redimensioned from 16-bit to 8-bit. To do this the Image menu had to be loaded first from Analysis/ Packages/ Image Processing. From the Image menu, Image Normalization is selected which pops up a Normalization Panel window. From the drop down menu, the stack to be converted is selected, the 0->255 option is selected and the Do It button is pressed. The stack is then redimensioned by going to Data/ Redimension Waves. A Redimension Waves window pops up from which the normalized stack is selected and the precision is changed from Unsigned word 16-bit to Unsigned byte 8-bit.

- To analyze slices from the stack, the 8-bit stacks are loaded into the Graphical Slicer. The Graphical Slicer is loaded from the menu Misc/ Graphical Slicer. The 8-bit stack to be analyzed is selected as the source wave and XY, YZ and XZ slices can be viewed and extracted. The export command is used to extract a slice to the data browser.

REFERENCES

2BM, Advanced Photon Source. "2BM Instrumentation". http://2bm.xor.aps.anl.gov/ Instrumentation /Equipment.html (accessed March 24, 2005, APS intranet).

Advanced Photon Source, Argonne National Laboratory, "Graphics gallery" http://www.aps.anl.gov/ald/grafgal2/digital/accelsysts.htm (accessed February 9, 2005).

Allenspacher. P., B. Huttner, W. Riede. 2003. *Ultrashort Pulse Damage of Si and Ge Semiconductors*. Proceedings of SPIE Vol. 4932: p. 358-365.

Amelinckx. S., R. Gevers and J. Van Landuyt. 1978. *Diffraction and Imaging Techniques in Material Science*. 2nd revised edition. Amsterdam; New York: North-Holland Pub. Co. Vol II.

Azzouz, Iftitan. M. 2004. *Investigation of Photoionization Processes in Ultrashort Laser Induced Damage in Optical Materials*. J. Phys, B: At. Mol. Opt. Phys. Vol 37: p. 3259-3264.

Boggon. T. J., J. R. Helliwell, R. A. Judge, A. Olczak, D. P. Siddons, E. H. Snellb and V. Stojanoff. 2000. *Synchrotron X-ray Reciprocal-Space Mapping, Topography and Diffraction Resolution Studies of Macromolecular Crystal Quality*. Acta Cryst. Vol D56: p. 868-880

Bowen, Keith. D and Brian Tanner. 1998. *High Resolution X-ray Diffractometry and Topography*. London; Bristol, PA: Taylor & Francis.

Certified Scientific Software, "SPEC" http://www.certif.com/spec.html (accessed June 7, 2005).

Chen. J. K., D. Y. Tzou, J. E. Beraun. 2004. *Numerical Investigation of Ultrashort Laser Damage in Semiconductors*. International Journal of Heat and Mass Transfer. Vol 48: p. 501-509.

Chen. J. K., D. Y. Tzou, J. E. Beraun. 2002 a. *Thermomechanical Response of Metals Heated by Ultrashort-pulsed Lasers*. Journal of Thermal Stresses. Vol 25: p. 539-558.

Chen. J. K., D. Y. Tzou, J. E. Beraun. 2002 b. *Ultrafast Deformation in Femtosecond Laser Heating*. Journal of Heat Transfer . Vol 128: p. 284-292.

Cullity B. D. 1978. *Elements of X-Ray Diffraction*. 2nd edition. Reading, Mass: Addison-Wesley.

Georgia State University. "HyperPhysics" http://hyperphysics.phy-astr.gsu.edu/hbase/ quantum/imgqua/bragglaw.gif (accessed April 15, 2005).

Hart, Michael. 1975. *Synchrotron Radiation - Its Application to High-Speed, High-Resolution X-ray Diffraction topography*. J. Appl. Cryst. Vol 8: p. 436

Hect, Jeff. 1994. *Understanding Lasers*. 2nd edition. New York: IEEE Press.

Herrmann. R. F. W., J. Gerlach and E. E. B. Campbell. 1998. *Ultra Short Pulse Laser Ablation of Silicon: a MD-Simulation Study*. Appl. Phys. A. Vol 66: p. 35-42

Hoszowska1. J., A K Freund, E Boller, J P F Sellschop, G Level, J Härtwig, R C Burns, M Rebak and J Baruchel. 2001. *Characterization of Synthetic Diamond Crystals by Spatially Resolved Rocking Curve Measurements*. J. Phys. D: Appl. Phys. Vol 34: p. A47-A51.

Hu. Z. W., B. Lai, Y. S. Chu, Z. Cai, D. C. Mancini, B. R. Thomas, A. A. Chernov. 2001. *Phase Sensitive X-ray Diffraction Imaging of Defects in Biological Macromolecular Crystals*. Phys. Rev. Lett. Vol 87: p. 148101.

Kawado. S, T. Taishi, S. Iida, Y. Suzuki, Y. Chikaura and K. Kajiwara. 2005. *Determination of the Three-Dimensional Structure of Dislocations in Silicon by Synchrotron White X-ray Topography Combined with a Topo-Tomographic Technique*. J. Phys. D: Appl. Phys. Vol 38: p. A17–A22.

Kishimura. H., A. Yazaki, Y. Hironaka, K. G. Nakamura, K. Kondo. 2003. *Lattice Deformation in Laser-Irradiated Silicon Crystal Studied by picosecond X-ray Diffraction*. Appl. Surface Sciences. Vol. 207: p. 314-317.

Korytar .D and C. Ferrari. 2001. *X-ray Topography in the Study of Semiconductors*. Acta Physica Slovaca. Vol. 51, No. 1: p. 9 – 15

Krawitz, Aaron D. 2001. *Introduction to Diffraction in Materials Science and Engineering*. New York: John Wiley.

Lang. A. R. 1959. *Studies of Individual Dislocations in Crystals by X-ray Diffraction Microradiography*. J. Appl. Phys. Vol 30. Issue 11: p. 1748-1755.

Linde, D. von der and K. Sokolowski-Tinten. 2000. *The Physical Mechanisms of Short-pulse Laser Ablation*. Appl Surface Science. Vol. 154-155: p. 1-10.

Liu. X., D. Du, and G. Mourou. 1997. *Laser Ablation and Micromachining with Ultrashort Laser Pulses*. IEEE J. Quantum Electron. Vol 33: p. 1706-1716.

Murray. C. E., I. C. Noyan, P. M. Mooney, B. Lai, Z. Cai. 2004. *Probing Strain Fields About Thin Film Structures Using X-ray Microdiffraction*. Mat. Res. Soc. Symp. Proc. Vol 795: p. 289-294

Silfvast, William. T. 2004. *Laser Fundamentals*. 2nd edition. Cambridge, UK; New York: Cambridge University Press.

Stojanoff. V., D. P. Siddons, L. A. Monaco, P. Vekilov, F. Rosenberger. 1997. *X-ray Topography of Tetragonal Lysozyme Grown by the Temperature-Controlled Technique*. Acta Cryst. Vol D53: p. 588-595.

Wavemetrics, Inc. "Igor Pro". http://www.wavemetrics.com/products/igorpro/igorpro .htm (accessed June 1, 2005).

Winholtz. R. A.. 2003. *An Investigation of X-ray Topography to Examine Laser-Induced Damage in Materials*. Air Force Summer Faculty Fellowship Program Final Report.